NTNU

Norwegian University of
Science and Technology

Turbulence Modelling of the Flow Around a Prolate Spheorid

Henrik Stumberg Larssen

Marine Technology
Submission date: June 2018
Supervisor: Bjørnar Pettersen, IMT

Norwegian University of Science and Technology
Department of Marine Technology

NTNU
Norwegian University of Science and Technology
Department of Marine Technology

MASTER THESIS IN MARINE HYDRODYNAMICS

SPRING 2018

FOR

Stud.techn. Henrik Stumberg Larssen

TURBULENCE MODELLING OF THE FLOW AROUND A PROLATE SPHEROID.

The candidate shall investigate the turbulence modelling of the flow around a 45degree inclined 6:1 prolate spheroid at Re=16000. This is to be conducted by use of the verification and validation standard ASME V&V 20, and the results shall be validated against available DNS results from MGLET. The work shall be performed with the CFD code OpenFOAM.
The candidate shall identify critical physical aspects of the flow, which needs to be captured in order to obtain qualitative similarity with the DNS results. Recommendations for appropriate turbulence modelling for the studied flow configuration, along with similar flows, are to be provided.
Focus of the study shall be on the near wake flow details. The results obtained shall be discussed and proper visualization of results are important for comparison
Computational parameters shall be investigated and documented. The proper parameters and detailed settings of the numerical simulations (including pre- and post-processing) shall be documented for later use.

In the thesis the candidate shall present his personal contribution to the resolution of the problem within the scope of the thesis work. Theories and conclusions should be based on mathematical derivation and logic reasoning identifying the various steps in the deduction. The original contribution of the candidate and material taken from other sources shall be clearly defined. Work from other sources shall be properly referenced. The candidate should utilize the existing possibilities for obtaining relevant literature.
The thesis should be organized in a rational manner to give a clear exposition of results, assessments and conclusions. The text should be brief and to the point, with a clear language.

The thesis shall contain the following elements: A text defining the scope, preface, list of contents, summary, main body of thesis, conclusions with recommendations for further work, list of symbols and acronyms, references and appendices. All figures, tables and equations shall be numerated.
It is supposed that Department of Marine Technology, NTNU, can use the results freely in its research work by referring to the student's thesis.
The thesis shall be submitted June 11th , 2018, in two copies.

Bjørnar Pettersen
Professor/supervisor

Co-supervisor: PhD Håkon Strandenes

Abstract

In numerous engineering disciplines, including naval and offshore engineering, the accurate prediction of turbulent flows is essential for cost-efficient and safe designs. For industrial applications, the turbulence must be modelled, and the development and understanding of appropriate turbulence modelling for a given type of problem follows an extensive set of case studies. The present thesis aims to be a contribution to that endeavor with respect to separating bluff body flows.

This thesis evaluates the ability of a set of RANS, hybrid and LES turbulence models to predict the flow around the 6:1 prolate spheroid at 45° incidence at $Re = 16000$ based on the minor axis. The flow configuration under investigation is the topic of an ongoing series of DNS studies at NTNU Trondheim, where preliminary results at $Re = 16000$ were used for model validation. This bluff body flow is a challenging turbulence modelling test case, which contains complex features as laminar-turbulent transition, flow separation, unsteadiness and an asymmetric wake. Thus, the test case is well suited to investigate shortcomings of different models and to drive model development. All simulations were performed with the CFD software OpenFOAM, and the models were verified and validated (V&V) with the standardized procedures in ASME (2009) and Hills (2005).

Because of issues with numerical stability, the V&V procedures could only be followed for RANS and hybrid models, whereas a less formal evaluation was performed for the LES models. The RANS models and hybrid models, which required numerical damping, exhibited a steady and symmetric flow about the meridional plane. The Smagorinsky LES model was able to predict the wake asymmetry, but it was less severe than that seen in the DNS study. Based on the stabilized and the undamped results prior to instability, unsteadiness and turbulence anisotropy at the near-body are assessed as critical aspects of the flow. These features of the flow are seen as essential in developing wake oscillations of sufficient magnitude to establish the wake asymmetry. Accordingly, hybrid models with an anisotropic RANS mode and LES models are recommended for modelling of this configuration and similar ones. Due to the shortcomings of this study and the continuous need for further V&V studies of bluff body flows, possible methodological improvements for a future V&V study of this flow configuration are discussed.

Sammendrag

I en rekke tekniske disipliner, inkludert marine- og offshore-engineering, er nøyaktig simulering av turbulente strømninger avgjørende for kostnadseffektive og trygge design. For industrielle applikasjoner må ofte turbulensen modelleres, og utvikling og forståelse av passende turbulensmodellering for et gitt type problem følger et omfattende sett av casestudier. Denne oppgaven har til hensikt å være et bidrag til den innsatsen med hensyn til separerende butte legeme strømninger.

Denne oppgaven evaluerer evnen til et sett med RANS, hybrid og LES turbulensmodeller for å forutsi strømningen rundt en $6:1$ prolate sfæroide ved $45°$ vinkling ved $Re = 16000$ basert på den mindre aksen. Strømningskonfigurasjonen som undersøkes er temaet for en pågående serie DNS-studier ved NTNU Trondheim, der foreløpige resultater ved $Re = 16000$ ble benyttet til modellvalidering. Denne strømningen er en utfordrende testcase, som inneholder blant annet laminær-turbulent transisjon, separasjon, en rekke ulike ustabiliteter og en asymmetrisk bakevje. Testcasen er derfor velegnet til å undersøke mangler i ulike modeller, og for å drive modellutvikling. Alle simuleringer ble utført med CFD-programmet OpenFOAM, og modellene ble verifisert og validert (V&V) med standardiserte prosedyrer fra ASME (2009) og Hills (2005).

På grunn av problemer med numerisk stabilitet kunne V&V-prosedyrene kun følges for RANS- og hybrid-modellene, mens en mindre formell evaluering ble utført for LES-modellene. RANS- og hybridmodellene, som krevde numerisk demping, viste en jevn og symmetrisk strømning rundt meridionalplanet. Smagorinsky LES-modellen var i stand til å forutsi asymmetrien, men den var svakere enn det som ble predikert i DNS-studien. Basert på de stabiliserte og de udempede resultatene før numerisk ustabilitet, er ustabiliteter i bakevja og turbulensanisotropi nære sfæroiden vurdert som kritiske aspekter ved strømningen. Disse egenskapene er blitt ansett som avgjørende for å utvikle bakevje-asymmetrien. Derfor anbefales hybridmodeller med en anistropisk RANS-modus og LES-modeller for modellering av denne og lignende strømninger. På grunn av manglene i denne studien og det kontinuerlige behovet for videre V&V-studier av separerende butte legeme strømninger, presenteres mulige metodologiske forbedringer i en fremtidig V&V-studie av denne strømningskonfigurasjonen.

Preface

This report comprises the Master's thesis in Marine Technology at NTNU Trondheim. The work has been conducted in the Spring semester of 2018 and is within the field of Marine Hydrodynamics. A V&V study on turbulence modelling of the 6:1 prolate spheroid at 45° incidence at $Re = 16000$ has been conducted.

The main motivation of the work has been to investigate the suitability of different types of turbulence models for bluff body flows. Highly interconnected to this endeavor is the identification of important physical characteristics of the flow. Additionally, conducting this project with the formal procedures in ASME (2009), allowed the specification of simulation uncertainties. The proposed background for the reader is an adequate competence in fluid mechanics, turbulence modelling and CFD.

The thesis topic was developed after discussions with my supervisors, Professor Bjørnar Pettersen and Ph.D. candidate Håkon Strandnes. It followed from the project thesis in Fall 2017, where I performed more elementary CFD simulations, and a literature survey on turbulence modeling of bluff body flows.

During the Fall and Spring of 2017/2018, I have improved my understanding of basic fluid mechanics, turbulence and CFD substantially. Through the thesis work, I have obtained a broad experience with different aspects of CFD and turbulence modelling, but I have also observed that I still have a substantial way to go in terms of research methodology and experience to properly contribute to the field.

Acknowledgement

I would like to thank Professor Bjørnar Pettersen for all help, encouragements and interesting discussions throughout the year. In making this assignment possible, I am really grateful. Additionally, I would like to thank co-supervisor Håkon Strandnes for all his help with the more practical aspects of the project. I.e., hardware, running jobs on the Vilje supercomputer and discussions on meshing and numerical settings.

To my colleges at Marine Technology, family, friends and Elisa, my sincerest thanks to you all for the support you have given me throughout my years in Trondheim and Berkeley.

Henrik Stumberg Larssen

Trondheim, June 2018

Contents

Nomenclature

Einstein notation is applied extensively in this thesis. A review is given in Kundu et al. (2012). In addition to the below nomenclature, note the filtering definition in section 2.2. Below, only the symbol of the unresolved component of the filtered variables are presented if not otherwise specified.

Latin Letters

$\boldsymbol{f}$	Body force vector
$\boldsymbol{n}$	Outward facing unit normal vector
$\boldsymbol{u}$	Velocity vector
$\eta,\ \xi,\ z$	Position components in body-fixed coordinate system
CF_i	Force coefficient components
D	Spheroid minor axis diameter
E	Validation comparison error
f_i	Body force components
k	Turbulent kinetic energy
L	Turbulence length scale
p	Static pressure
r	Multivariate validation metric; refinement factor
Re	Reynolds number, $\frac{U_0 D}{\nu}$
S	Resolved strain-rate magnitude, $\sqrt{2S_{ij}S_{ij}}$
S_{ij}	Resolved strain-rate tensor, $\frac{1}{2}(\frac{\partial U_i}{\partial x_j} + \frac{\partial U_j}{\partial x_i})$
St	Strouhals number, $\frac{fD}{U_0}$
u, v, w	Instantaneous velocity components in $x,\ y,\ z$ - directions
U_0	Uniform inflow magnitude
u_i	Velocity components
$x,\ y,\ z$	Position components in global coordinate system
x_i^+	Dimensionless, sublayer-scaled, distance
x_i	Position components in global coordinate system

Greek Letters

$\boldsymbol{\omega}$	Vorticity vector
Δ	LES filter width
δ_{ij}	Kronecker delta
γ	Intermittency
μ	Dynamic viscosity
μ_t	Eddy viscosity
ν	Kinematic viscosity
ν_t	Kinematic eddy viscosity
ν_{SGS}	Kinematic SGS viscosity
ω	Vorticity vector magnitude; specific dissipation rate
ω_i	Vorticity components
Ω_{ij}	Resolved rotation-rate tensor
ρ	Mass density
τ_w	Surface shear stress
τ_{ij}	Unresolved component stress tensor
θ	Momentum thickness
Re_θ	Momentum thickness Reynolds number, $\theta U_0/\nu$

Abbreviations

CFD	Computational fluid mechanics
CFL	Courant-Friedrichs-Lewy number, $\Delta t \frac{u_i^{'}}{\Delta x_i}$
DES	Detached-eddy simulation
DNS	Direct numerical simulation
EARSM	Explicit algebraic Reynolds stress models
FVM	Finite volume method
GCI	Grid convergence index
LDA	Laser doppler anemometry
LES	Large-eddy simulation
PDE	Partial differential equation
RANS	Reynolds-Averaged Navier-Stokes
SAS	Scale-adaptive simulation
SGS	Subgrid-scale
V&V	Verification and validation

Chapter 1

Introduction

1.1 Background and Motivation

What are the drag on a submarine or the forces acting on an offshore riser? The solutions to these complex problems depends on an accurate prediction of the surrounding flows. In addition to these two examples, offshore and naval engineers face numerous problems where prediction of turbulent flows is essential in establishing cost-efficient and safe designs.

Apart from recent history, the only tractable approaches to these problems were theoretical and experimental fluid mechanics (EFD). Starting from the fundamental conservation laws from Newtonian mechanics, Navier and Stokes, amongst others, derived the governing equations for viscous fluid flow in the mid-19th century, the Navier-Stokes equations (White, 2007). However, due to their complexity, the assumption of a frictionless (ideal) fluid was for long the only practical approach to solving these equations. This provided limited practical use for fluid engineers, especially in the case of internal flows, who resorted to experiments. This gap between theory and empiri did not start to narrow before the advent of Prandlt's boundary layer theory in 1904 (Prandtl, 1904). In this theory, the flow is divided into two regions, one close to bodies where viscous action is important, and an outer region where it can be neglected. In the case of the two aforementioned flows, the outer regions may be predicted with potential flow theory, while the inner layer is governed by the full Navier-Stokes equations. Alongside Prandtl's discovery, Reynolds' systematic experiments of different flow regimes and his use of non-dimensional numbers were crucial in the understanding of fluid flows (White, 2007). Another important work in the understanding of turbulent flows, were given by Kolmogorov, who established a lower limit for turbulent scales (Tikhomirov, 1991). The combination of theoretical developments and the advent of new instrumentation techniques, made EFD the powerful and important discipline it is today (White, 2007). However, there are some important limitations to EFD: Investigation of numerous configurations, as desirable in design, is costly. Further, results face issues with blockage and scale effects (Vaz et al., 2016).

Many of the limitations of EFD can be circumvented with computational fluid dynamics (CFD). In CFD, a mathematical model, resembling the physics, is solved numerically to simulate the flow. For our applications, this consist of the incompressible Navier-Stokes equations coupled with some turbulence model. Major breakthroughs in CFD followed the increase in computing power in the 1950s-1980s; finite difference methods were developed extensively (Thomée, 2001), and finite volume methods with pressure-velocity coupling algorithms were devised (Patankar and Spalding, 1972). Even though these methods may have advantages over EFD, they introduce numerous error sources (cf. section 2.5). Presently, the main error source in this endeavor is the turbulence modelling error (Wilcox, 2006). The need for turbulence modelling follows from Kolmogorov (1941); Kolmogorov argued that the smallest turbulent length scales scale such that the required number of grid cells in a 3D computation is given as $N \sim Re^{9/4}$ (Müller, 2017). Thus, for a typical marine flow of $Re = 10^9$, a computational solution is presently infeasible. The rationale of turbulence modelling is to limit the grid requirements by modelling the effect the smaller scales have on the larger ones. That raises the fundamental questions of turbulence modelling: which scales are to be modelled, and in what manner?

These questions have been investigated since the days of Reynolds and Boussinesq in the late 19th century (Wilcox, 2006). A vast range of models have been developed; these models differ in what scales are modelled (filtering) and the modelling ranges from simple algebraic relations to transport equations(PDEs). In the assessment of each model, note Wilcox's description of the ideal model:"An ideal model shall introduce the minimum amount of complexity while capturing the essence of the relevant physics" (Wilcox, 2006, p. 2). I.e., in a world with limited computing power, there is no such thing as a perfect model covering all flows, as there is trade-off between accuracy and cost. The model selection depends on the flow; in a simple free shear flow an algebraic model may suffice, while a complex separating flow may only be accurately resolved with demanding hybrid or LES simulations. Followingly, how are the flows usually seen in offshore engineering to be modelled accurately? These flows are typically high Reynolds number flows around bluff bodies. In Larssen (2017), major characteristics of such flows were identified: turbulence anisotropy, unsteadiness and three-dimensionality. To investigate model suitability for bluff body flows, a range of different type of models were recommended for Verification and Validation (V&V) studies: $k-\omega\ SST$, $BSL-EARSM$, $k-\omega\ SST\ SAS$ and $k-\omega\ SST\ DES$. These models were identified as accurate within their respective type (e.g., $k-\omega\ SST$ is a popular isotropic RANS model), distinctly different and representing computational costs that is presently acceptable in industry.

To accurately and objectively assess the appropriate turbulence modelling for highly separating bluff body flows, numerous verification and validation(V&V) studies are needed. I.e., by performing a number of test cases with different flow characteristics, the accuracy of each model may be identified (Vaz et al., 2016). This may be used to develop model improvements or best-practice guidelines. If this is to be done in a systematic and collective manner, standardized procedures for verification and validation should be utilized to ensure comparable results. In this context verification denotes the process where the numerical uncertainty of a simulation is identified (Roache, 1998). If this is combined with a comparison to experimental results(validation), the modelling uncertainty may be quantified. One of the early developments in this field is Roache (1998). Later, his work has been extended in works by Hills (2005) and Eça and Hoekstra (2014). An established framework for V&V are given in the standard ASME (2009). The aim of this procedure may be to establish the uncertainty in a simulated quantity (e.g. a 95 % confidence interval in a force coefficient). Alternatively, following Hills (2005), the multivariate procedure is used to assess the model's overall suitability for a given problem. Note, in addition to these objective measures on model suitability, a thorough understanding of the flow physics is needed to assess the results. I.e., why do the V&V study show that model X is not suitable and why is model Y deemed suitable? Given the results and such an understanding, model improvements and/or best-practice guidelines may be pursued.

This thesis aims to be a contribution to the above effort. I.e., it aims to be a formal V&V study, contributing to improved understanding and modelling of the turbulence present in separating bluff body flows. Towards that aim, the procedures in ASME V&V 20 and Hills (2005) have been used to assess model predictions of the flow around the 6:1 prolate spheroid at 45° incidence at $Re = 16\ 000$ based on the minor axis. This flow case has been investigated by my supervisor with DNS simulations and may be characterized as a separating bluff body flow. More specifically, the boundary layer flow is characterized by laminar-turbulent transition and the wake is asymmetric and moderately unsteady. To address these characteristics, additional turbulence models were included, and most notably two LES models. In addition to conducting a V&V study, an aim of this thesis is to complement the DNS studies in describing this problem's governing flow physics. I.e., some features of the flow might not been captured by some model while another one might. Then, given a proper understanding of the different models, the triggering mechanism of a feature of the flow may be identified. Some important applications of this flow configuration is related to submarine maneuverability and particle modelling. A more detailed account of applications is given in Jiang et al. (2015).

1.2 Scope and Limitations of the Present Thesis

This study aims to increase the understanding of turbulence modelling for separating bluff body flows. These types of flows have relevance in numerous engineering disciplines, where their accurate prediction is of essence for cost-efficient, safe designs. To provide a proper assessment of a set of selected model's suitability for this type of flow, the procedures in ASME (2009) is adopted. I.e., a formal V&V study is to be conducted, and the test case is the 6:1 prolate spheroid at 45° incidence at $Re = 16000$ based on the minor axis. The simulations are to be validated against preliminary results of a DNS study by my supervisors and colleagues. The thesis objectives may be summarized in the following.

1. Perform a V&V study in accordance with ASME (2009) for the 6:1 prolate spheroid at 45° incidence at $Re = 16000$ for the turbulence models: $k-\omega\ SST$, $k-\omega\ SSTLM$, $k-\omega\ SST\ SAS$, $k-\omega\ SST\ DES$, Smagorinsky and WALE.

2. Based on the V&V study and post-processing of the simulations, identify critical physical aspects of the flow that needs to be captured to ensure qualitative similarity to the DNS results. I.e., an asymmetric wake. Provide recommendations for appropriate turbulence modelling of the studied flow configuration and similar flows.

There are some limitations to this study. The generalizability of the result is assumed to be restricted to curved, separating flows at moderate Reynolds number. With higher Reynolds numbers, it is assumed that the appropriate turbulence modelling might change. Hence, more V&V studies are needed to cover the full Re parameter space.

Due to time limitations, there are some methodological limitations to the study. In the field of V&V, there are more accurate procedures to estimate and monitor errors than those applied in this study. However, these methods are work-intensive in terms of computing time and pre-processing, and was thus not pursued. Further, there are some quantities of interest that were not readily available in OpenFOAM, the applied CFD software. With more resources, utilities could have been developed to increase control of the meshes used for LES models (x^+, z^+), and to investigate the different modelling regions for hybrid models.

The above limitations, along with proposed solutions, are discussed in section 4.5.

1.3 Outline of the Present Thesis

The present thesis is subdivided into 5 chapters and an appendix. Each chapter is further subdivided into sections. Their contents are briefly outlined below.

Chapter 1 presents the background and the motivation for this study. This is traced from the need of accurate flow predictions to that of accurate turbulence modelling. Further, accuracy follows from substantial model development and testing, and this is formalized in terms of Verification and Validation studies, whereof this thesis aims to contribute. Followingly, the motivation is concretized in a set of objectives. Additionally, limitations of this study in terms of generalizability and methodology are given.

Chapter 2 is to provide the necessary background theory and references for pursuing chapters. The initial section are devoted to a presentation of the governing equations and their physical characteristics of relevance to bluff body flows in general and for the prolate spheroid specifically. This includes a description of the preliminary DNS results of the flow configuration under investigation. Thereafter, the applied turbulence models are presented with an emphasis on their modelling ability of bluff body flows. Lastly, the main concepts of FVM are given along with its error sources, and the V&V procedures of ASME (2009) and Hills (2005) are presented.

Chapter 3 outlines specifics of the methodology applied in the study. I.e., aspects of the numerical solution such as applied software, the computational domain and boundary conditions. Next follows a description and discussion of the meshing methodology and the utilized numerical settings. Lastly, post-processing tools and the V&V procedure of this study are described in detail.

Chapter 4 presents and discusses the results. At first, all simulations are presented and discussed separately for each model type (LES, hybrid or RANS). Here, the emphasis is on qualitative validation with reference to the DNS results. Next, the results of the V&V study are presented, along with an interpretation. Lastly, the trends and indications of the previous sections are discussed. I.e., the important physical characteristics of the flow, and how the physics is to be translated into appropriate turbulence modelling. Additionally, methodological features of this V&V study are discussed.

Chapter 5 concludes the findings of the thesis and outline recommendations for further work. The conclusions highlight characteristic flow features and the appropriate type of turbulence modelling for this flow. Regarding further work, an emphasis is on a future V&V study that would build on the findings of this study and address its methodological shortcomings. However, to improve the understanding of turbulence modelling for the studied configuration and similar flows, other efforts are also identified. Particularly, more turbulence modelling development for anistropic hybrid models and formal V&V procedures for the use of DNS in validation are recommended.

Appendix includes various supplementary material not included in the main report. In Appendix A, all force coefficient time histories, except the ones who are qualitatively similar, are displayed. E.g., for a model that yields the same qualitative results for all three meshes, only one time history are presented. Further, the force coefficient statistics, along with V&V results are given in Appendix B. Appendix C is an extract of the literature survey on turbulence modelling for separating bluff body flows in Larssen (2017). Appendix D contains OpenFOAM scripts, displaying the numerical schemes for the different model types and the solution settings. Additionally, the project thesis and a poster are accompanying the thesis in a separate zip folder (Attached.zip).

Chapter 2

Background Theory

2.1 Governing equations

This section first presents the governing equations for incompressible Newtonian flow, followed by the corresponding filtered equations. Thereafter, the filtering operations in Reynolds-averaged Navier-Stokes(RANS) and Large Eddy Simulation(LES) are briefly discussed. A proper understanding of this section, the filtering in particular, is essential when investigating the suitability of different turbulence models (cf. section 2.3).

The Incompressible Navier-Stokes Equations

The fluid in this study is considered incompressible and Newtonian. Following the fundamental law of mass conservation, the continuity equation for incompressible flow may be derived (Kundu et al., 2012)

$$\frac{\partial u_i^{'}}{\partial x_i} = 0 \ . \tag{2.1}$$

Linear and angular momentum balance results in Cauchy's equation

$$\frac{\partial u_i^{'}}{\partial t} + u_j^{'} \frac{\partial u_i^{'}}{\partial x_j} = \frac{1}{\rho} \frac{\partial \sigma_{ij}^{'}}{\partial x_j} + f_i^{'} \ . \tag{2.2}$$

which reduces to the incompressible Navier-Stokes equations with the aforementioned constitutive assumptions

$$\frac{\partial u_i^{'}}{\partial t} + u_j^{'} \frac{\partial u_i^{'}}{\partial x_j} = -\frac{1}{\rho} \frac{\partial p^{'}}{\partial x_i} + \nu \frac{\partial^2 u_i^{'}}{\partial x_j \partial x_j} + f_i^{'} \ , \tag{2.3}$$

where the stress tensor is given as $\sigma_{ij}^{'} = -p^{'}\delta_{ij} + 2\mu s_{ij}^{'}$. Eqs. (2.1) and (2.3) constitute an elliptic-parabolic system of PDEs, which govern 3D Newtonian incompressible fluid flow (Müller, 2017).

Filtered equations

As described in Tikhomirov (1991), a turbulent flow contains a continuum of different length and time scales. For high Reynolds number flows ($Re \sim 10^9$), resolving the entire range of scales is not computationally viable. Hence, a filter is introduced to decompose a quantity $\psi^{'}$ into a resolved component Ψ and an unresolved component ψ. I.e., $\psi' = \Psi + \psi$ (Vaz et al., 2017). This filter is constant preserving and commuting with spatial and temporal differentiation. Then, if this filter is applied to Eqs. (2.1) and (2.3), it leads to

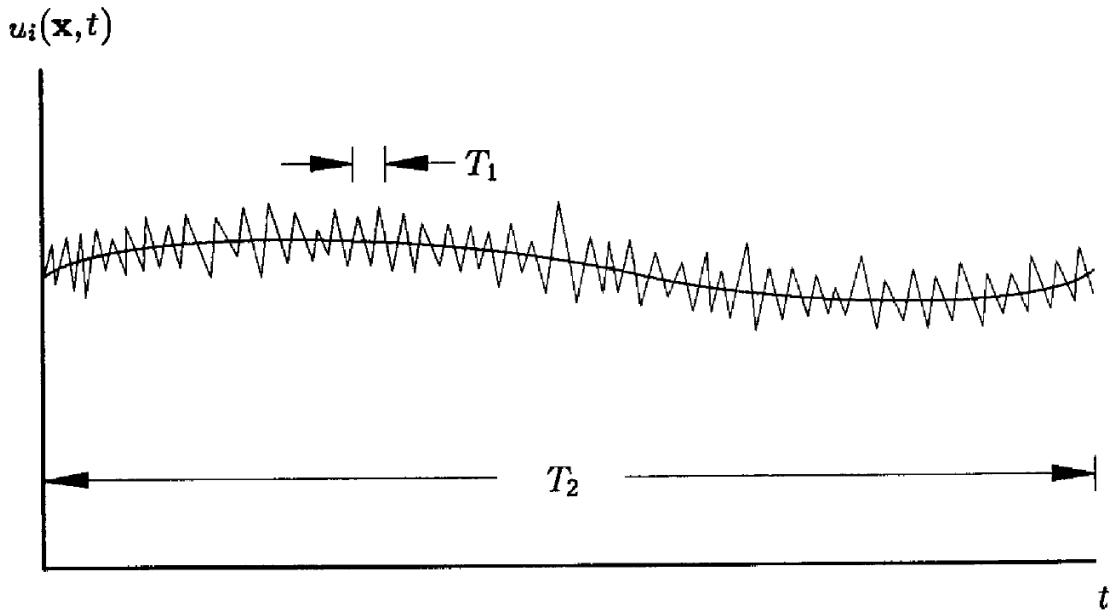

Figure 2.1: Time averaging of nonstationary turbulence (Wilcox, 1998).

$$\frac{\partial U_i}{\partial x_i} = 0 \ , \tag{2.4}$$

$$\frac{\partial U_i}{\partial t} + U_j \frac{\partial U_i}{\partial x_j} = -\frac{1}{\rho}\frac{\partial P}{\partial x_i} + \nu \frac{\partial^2 U_i}{\partial x_j \partial x_j} + f_i + \frac{1}{\rho}\frac{\partial}{\partial x_j}(\tau_{ij}(u_i, u_j)) \ . \tag{2.5}$$

Note, the filtering operation introduces a new diffusion-like term including the tensor τ_{ij}, which models the effect of the unresolved components. Eqs. (2.4) and (2.5) are governing for all the turbulence models in this study. Further, a possible hypothesis regarding τ_{ij} is the Boussinesq hypothesis (Wilcox, 1998)

$$\frac{\tau_{ij}(u_i, u_j)}{\rho} = 2\nu_t S_{ij} - \frac{2}{3}k\delta_{ij} \ . \tag{2.6}$$

This hypothesis implies that the eddy viscosity is a scalar and thus invariant for all τ_{ij} at a given point in space and time. All models in this study apply this hypothesis, but notice that the assumption is highly dependent on the filtering operation.

RANS filtering

In RANS, the filtering operation decomposes the pressure and velocity field to a slowly varying mean part with time scale T_2 and a rapidly fluctuating turbulent with time scale T_1 (Wilcox, 2006). This is well depicted in Figure 2.1. If the flow variables are time averaged with time scale T, the following must hold

$$U_i(\mathbf{x}, t) = \frac{1}{T}\int_t^{t+T} u_i'(\mathbf{x}, t)\ dt \ , \qquad T1 << T << T2 \ . \tag{2.7}$$

Further, τ_{ij} are denoted the Reynolds stresses, and represent the momentum transfer from the mean flow to the turbulent fluctuations (Tennekes and Lumley, 1985). In the case of RANS, the Boussinesq assumption implies equal normal Reynolds stresses($\tau_{11} = \tau_{22} = \tau_{33}$). In Wilcox (2006), it is identified a set of flow-cases where this do typically not hold, and three-dimensional flows over curved surfaces are listed.

LES filtering

In LES, the filter represents a spatial averaging that removes scales smaller than the grid spacing (Wilcox, 1998). There are numerous LES filters, whereas the first and simplest one is the volume averaged box filter in Deardorff (1970)

$$U_i(\mathbf{x},t) = \int_{x-\frac{1}{2}\Delta x}^{x+\frac{1}{2}\Delta x} \int_{y-\frac{1}{2}\Delta y}^{y+\frac{1}{2}\Delta y} \int_{z-\frac{1}{2}\Delta z}^{z+\frac{1}{2}\Delta z} u_i^{'}(\boldsymbol{\xi},t) d\xi d\eta d\zeta \ . \tag{2.8}$$

τ_{ij} are denoted the subgrid-scale stresses (SGS) and these stresses are intended to model stresses from eddies in the inertial sub-range (Müller, 2017). This definition introduces much stricter requirements to spatial and temporal resolutions than in RANS. Close to solid boundaries, these scales approach the ones encountered in DNS (Wilcox, 2006). A further discussion on wall-bounded turbulent flows are given in section 2.2. Note, the Boussinesq approximation for LES, amounts to assuming isotropic turbulence at the inertial sub-range, which is motivated by the realization that small scale turbulence tends towards isotropy, while larger scales are flow dependent (Wilcox, 2006).

2.2 Flow around Bluff Bodies

When investigating the fluid forces on a given body, it is useful to differentiate between streamlined and bluff bodies. Typically, for a streamlined body, friction forces are dominating. In the case of bluff bodies, as investigated in this study, flow separation is common and this results in additional form drag (Schlichting et al., 2017). For moderate to high Reynolds numbers, the form drag might be asymmetric and unsteady in nature. An example is the circular cylinder at $Re > 40$ (Sumer and Fredsøe, 1997); this flow causes a periodic lift force on the body, which may be critical in design, as this can cause resonance.

An accurate resolution and modelling of the boundary layer is essential in an accurate prediction of separation and hence also the form drag (Wilcox, 1998). In many situations, laminar-turbulent transition is critical in this aspect. In the following, the flow around bluff bodies are investigated in the light of these phenomena. At the end of this section, the relevant flow physics for the 6:1 prolate spheroid are considered in detail. This is of major importance, as the complexity of the flow physics ultimately determines the suitable level of turbulence modelling (Wilcox, 1998).

Boundary Layers, Transition and Separation

The flow around solid objects may be subdivided into two distinct regions: the boundary layer and the outer flow (Prandtl, 1904). In the boundary layer and in its wake, viscous forces are important, while they are negligible in the outer flow. In the limit of $Re \to \infty$, the steady 2D incompressible steady Navier-Stokes equations simplifies in the boundary layer to

$$u^{'}\frac{\partial u^{'}}{\partial x} + v^{'}\frac{\partial u^{'}}{\partial y} = -\frac{1}{\rho}\frac{dp}{dx} + \nu\frac{\partial^2 u^{'}}{\partial y^2} \ . \tag{2.9}$$

At a wall, due to the no-slip and impermeability conditions (White, 2007), Eq. (2.9) reduces to

$$\nu\frac{\partial^2 u^{'}}{\partial y^2} = \frac{1}{\rho}\frac{dp}{dx} \ . \tag{2.10}$$

As the flow moves in the streamwise direction and the pressure gradient gradually increases due to an outer flow, the streamwise velocity is reduced (Schlichting et al., 2017). This process is depicted in Figure 2.2. In 2D, separation is defined as a point of zero shear stress (Schlichting et al., 2017). I.e.,

$$\tau_w = \mu\frac{\partial u^{'}}{\partial y}|_{y=0} = 0 \iff \frac{\partial u^{'}}{\partial y}|_{y=0} \ . \tag{2.11}$$

This corresponds to the 3rd velocity profile from the left in Figure 2.2. At separation, the boundary layer profile leaves the wall and the downstream backflow pushes it away from the wall. When the

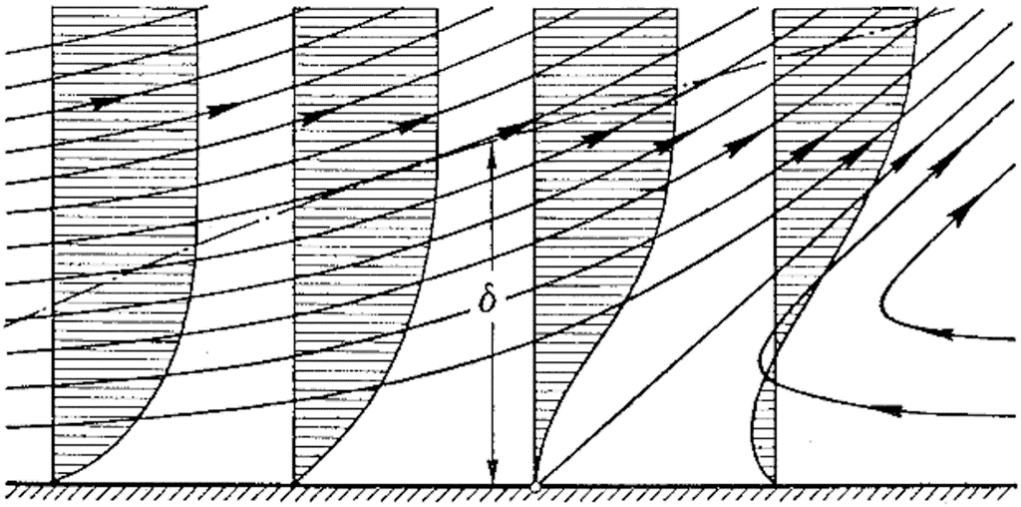

Figure 2.2: Flat plate boundary layer separation (Schlichting et al., 2017).

flow separates, the pressure recovery seen for streamlined bodies do not occur, and this results in form drag. Another important feature of the boundary layer follows from Eq. (2.10). When the pressure gradient equals zero, $\frac{\partial^2 u'}{\partial y^2} = 0$, and this is a necessary requirement for instability in an inviscid parallel shear flow (Drazin, 2002). Hence, the separating shear layers can be unstable and roll up into vortical structures, which possibly may trigger transition (separation induced transition). The equivalent separation form in 3D is often denoted as closed separation and is defined in terms of lines with zero wall shear stress (separation lines) (Schlichting et al., 2017). Downstream of the separation lines, backflow bubbles are present.

The transition mode seen for a flat plate with zero pressure gradient is denoted as natural transition (cf. Figure 2.2). At some critical Reynolds number, flow perturbations propagates into 2D Tollmien-Schlichtling (T-S) waves (2) (Schlichting et al., 2017). These waves initiate transition through interactions, forming 3D structures denoted as turbulent spots (3)-(5). As noted in Jovanovic and Nishi (2017), these structures are highly anisotropic. With increasing Reynolds number, these spots diffuse, interact and produce a fully turbulent flow (6). At high Reynolds numbers, the fully turbulent flow has reduced levels of anisotropy relative to the transition phase (Jovanovic and Nishi, 2017).

For concave objects, as the 6:1 prolate spheroid, it can be shown that the curvature is destabilizing for the 3D disturbances seen in natural transition. This instability causes the creation of Görtler vortices, and further details can be found in Schlichting et al. (2017). With this geometry, the Boussinesq assumption generally do not hold, as the turbulence is anisotropic (Wilcox, 2006).

Lastly, crossflow instabilities are seen in 3D flows. Because of the 3D geometry and the resulting pressure gradients, the flow will develop what is denoted as secondary flows. I.e., velocity components which is orthogonal to the streamwise direction. This velocity profile may become unstable, and this type of instability may cause open separation. Here, the flow separates without the requirement of wall shear stress equalling zero. This instability is further discussed in Schlichting et al. (2017) and Rosenhead (1963).

Note, the aforementioned transition modes interact, making the prediction of transition and flow separation a difficult modelling task (Schlichting et al., 2017). Typically for a bluff body 3D flow, both open and closed separation occur. However, correct modelling of separation and the turbulence onset is crucial in determining the correct flow patterns and vortex dynamics.

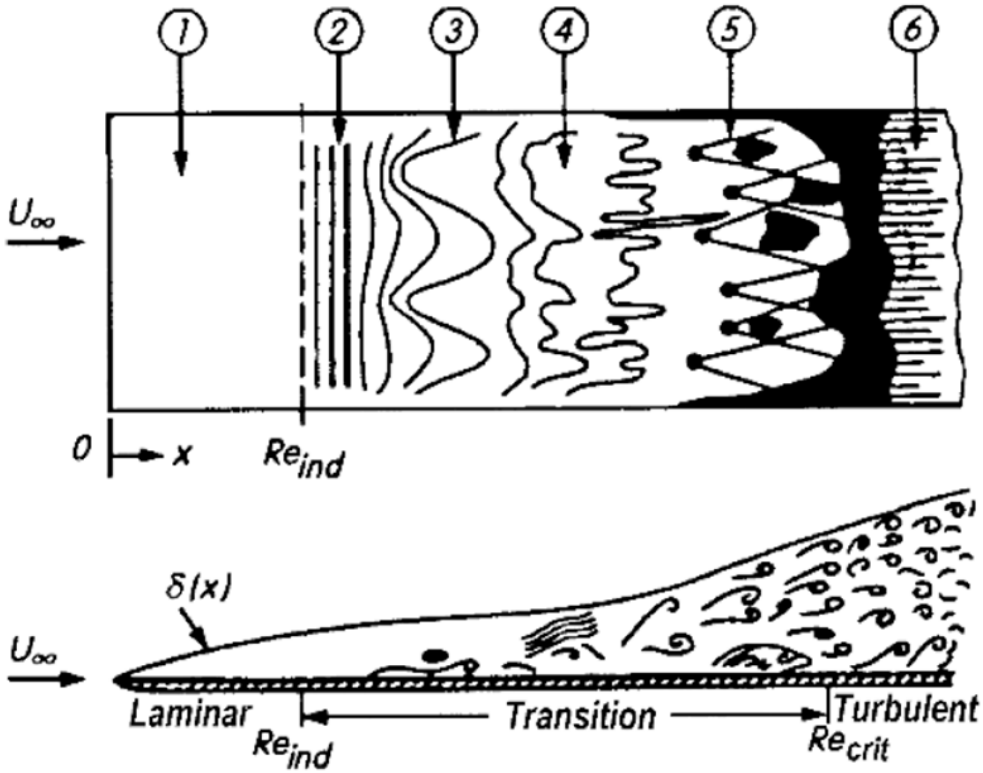

Figure 2.3: Natural transition (Schlichting et al., 2017).

Turbulent Boundary Layers

Following transition to a fully turbulent flow, the mean streamwise turbulent boundary layer is described by the law of the wall (Wilcox, 1998). If transport processes are neglected, as in attached boundary layers, dimensional analysis yields the following relation of the velocity profile

$$u^+ = f(y^+) \ , \tag{2.12}$$

where the following nondimensional variables are used

$$u^+ = \frac{U}{u_*} \ , \quad u_* = \sqrt{\frac{\tau_w}{\rho}} \quad y^+ = \frac{y}{\nu/u_*} \ . \tag{2.13}$$

By physical arguments, the shape of the function f can be determined; closest to the wall, in the viscous sublayer, viscous effects dominate. In the mid region, the buffer layer, both viscous and Reynolds stresses are important and in the outer layer, the log layer, the Reynolds stresses dominate. These different layers are illustrated in Figure 2.4. In the viscous sublayer ($y^+ < 5$)

$$u^+ = y^+ \ , \tag{2.14}$$

and in the log-layer ($30 < y^+ < 200$) it is given by

$$u^+ = \frac{1}{\kappa} ln(Ey^+) \ , \tag{2.15}$$

where κ and E are constants.

For fully turbulent attached flows, it has been shown that the use of the log-layer as a boundary condition is accurate (Eça et al., 2015). However, for flows with laminar regions it can be highly inaccurate, and consequently, the iterative convergence is significantly slowed down (cf. section 2.4). Alternatively to using the log-law, the equations may be resolved down to the viscous sub-layer. When this approach is applied, it is typically denoted as a low-Re number turbulence model. Contrary to log-layer modelling, this approach is not susceptible to errors due to transport processes,

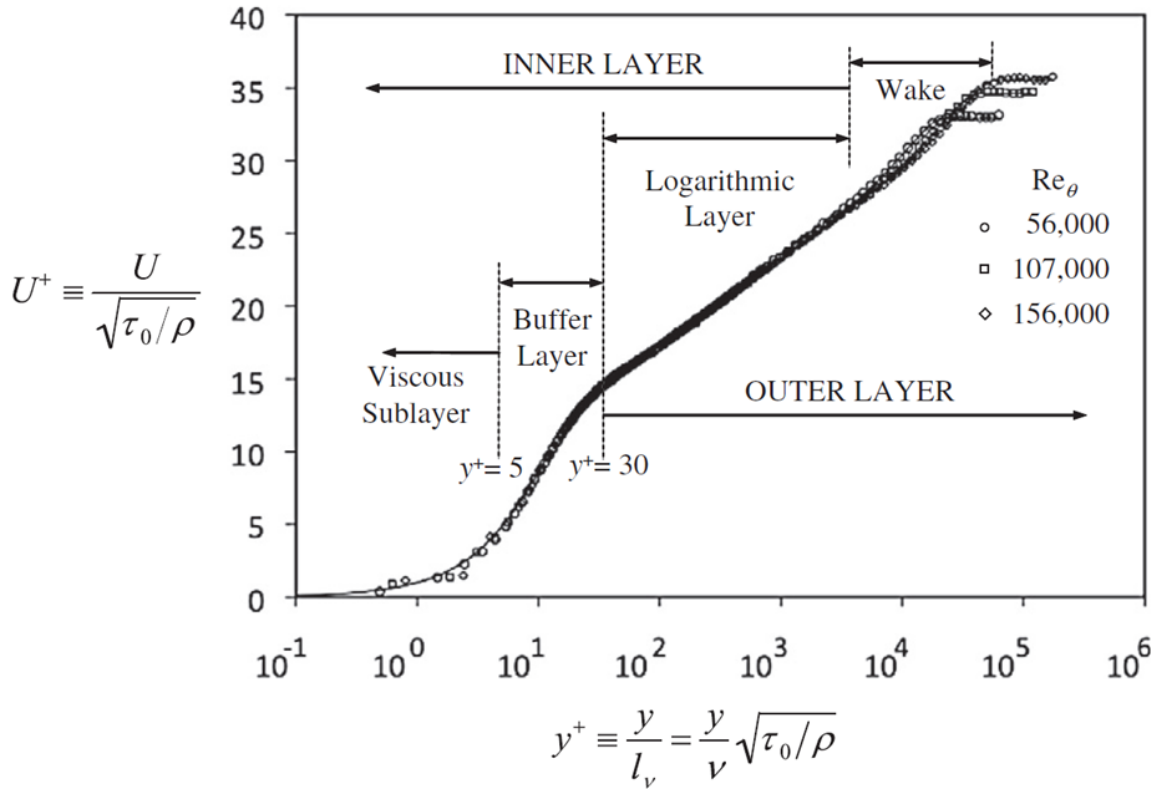

Figure 2.4: Law of the wall ($\tau_0 = \tau_w$) (Kundu et al., 2012).

as only a laminar velocity profile are to be resolved; in the viscous sub-layer, the unresolved component tensor τ_{ij} is assumed negligible compared to the viscous stresses. These assumptions may be used to simplify the k and ω equations (cf. section 2.3), yielding the relations (Liu, 2018)

$$k^+ = C_k (y^+)^{3.23} \ , \qquad k^+ = \frac{k}{u_\tau^2} \ , \tag{2.16}$$

$$\omega^+ = \frac{6}{(\beta_1 y^+)^2} \ , \qquad \omega^+ = \frac{\omega \nu}{u_\tau^2} \ , \tag{2.17}$$

where β_1 and C_k are constants and the eddy viscosity is derived from the above with $\nu_t = \frac{k}{\omega}$. Note, these boundary conditions do only hold in the viscous sub-layer, and a usual criteria for RANS simulations are $y^+_{max} < 1$ (Pereira et al., 2017).

Similarly as with RANS, the boundary layer can either be resolved or modelled in LES. In near wall-resolved LES, the dynamics of the near-wall is resolved directly. Note, the dynamics captured with LES are highly different from RANS because of the different filtering. In Sagaut (2006), it is recommended to satisfy the following inequalities for an accurate resolution of the boundary layer

$$\Delta x^+ < 10 \ , \ \Delta z^+ < 5 \ , \ y^+ < 1 \ , \tag{2.18}$$

where

$$\Delta x_i^+ = \frac{\Delta x_i}{x_i^+} \ , \qquad x_i^+ = \frac{x_i}{\nu / u_\tau} \ , \tag{2.19}$$

and Δx_i denotes the grid spacing in the i-th direction. Here, x is the streamwise direction, while z denotes the crosswise direction.

Vorticity Dynamics

As denoted in Tennekes and Lumley (1985), turbulence is characterized with high levels of fluctuating vorticity. Thus, understanding vorticity dynamics is essential in understanding turbulent flows. The vorticity vector is given as the curl of the velocity vector

$$\boldsymbol{\omega}' = \nabla \times \boldsymbol{u}' \ . \tag{2.20}$$

In understanding the motion of fluid particles and the role of vorticity, the decomposition in Rosenhead (1963) is illustrative. A sphere of fluid is considered, and its motion is regarded as the combination of three modes:

1. Uniform translation with velocity $\boldsymbol{u}'$ at its centre.
2. Rotation with strength and direction $\frac{1}{2}\boldsymbol{\omega}'$.
3. Stretching of the sphere to an ellipsoidal shape.

In addition, vorticity dynamics may be investigated by the vorticity equation, which follows from taking the curl of the momentum equations (2.3) (Tennekes and Lumley, 1985).

$$\frac{\partial \omega_i'}{\partial t} + u_j' \frac{\partial \omega_i'}{\partial x_j} = \omega_j' \frac{\partial u_i'}{\partial x_j} + \nu \frac{\partial^2 \omega_i'}{\partial x_j \partial x_j} \ . \tag{2.21}$$

Hence, the total change of vorticity is balanced by viscous diffusion and stretching/tilting (first term on the RHS). The stretching and tilting term is absent in 2D flows, signifying that turbulence is three-dimensional in nature. Another point of emphasis is the production and destruction of vorticity, which occurs at solid or free surfaces (Rosenhead, 1963). In this study, the spheroid acts as a vorticity sink and source. To illustrate this, consider a 2D boundary layer flow, where the following assumption holds

$$\omega_z' = \frac{\partial v'}{\partial x} - \frac{\partial u'}{\partial y} \sim -\frac{\partial u'}{\partial y} \ . \tag{2.22}$$

Combining Eq. (2.22) with (2.10) yields

$$\frac{1}{\rho}\frac{dp'}{dx} = -\nu \frac{\partial \omega_z'}{\partial y} \ . \tag{2.23}$$

As Eq. (2.10) follows from boundary layer theory, Eq. (2.30) is limited to relatively streamlined bodies. However, this equation states that the boundary layer acts as a vorticity source in the case of favourable gradients ($\frac{dp'}{dx} < 0$) and as a sink for adverse pressure gradients ($\frac{dp'}{dx} > 0$). Hence, the vorticity produced at the walls are convected and diffused to the rest of the flow. In this case, the separation types discussed in 2.2 are crucial in understanding the wake vorticity dynamics.

Further, vorticity appears in the form of coherent flow structures, making them well suited to investigate wake dynamics (Jeong and Hussain, 1995). These flow structures consist of an assembly of vortices, which is typically defined as a concentration of codirectional or nearly codirectional vorticity (Kundu et al., 2012). Further, a vortex line is defined as a curve in the fluid where the vorticity vector is aligned with the tangent of the curve. This is analogous to how a streamline is related to the velocity vector. Next, in a region of nontrivial vorticity, the vortex lines passing through a closed curve form a vortex tube (Kundu et al., 2012).

In being able to analyze the evolution of coherent structures, they first need to be identified with some suitable criterion. First, given the above definition of a vortex, the velocity field only due to motion type 2. is given in polar coordinates as $u_r = 0$ $u_\theta = \frac{\omega'}{r}, u_z = 0$ (Kundu et al., 2012). This amounts to rigid body rotation, where the z-axis is aligned with $\boldsymbol{\omega}'$ and ω' denotes its magnitude. The momentum equations yield the following result for the pressure

$$p(r,\theta) - p_0 = \frac{1}{8}\rho \omega'^2 r^2 \ , \tag{2.24}$$

where p_0 is the pressure at $r = 0$. Thus, the center of a vortex have a pressure minimum. This realization was used in Jeong and Hussain (1995) to devise the λ_2-method that identifies coherent flow structures. The momentum equations are manipulated to find an expression for the hessian of the pressure that only contains terms due to vortical motions

$$-\frac{1}{\rho}\frac{\partial^2 p'}{\partial x_j \partial x_i} = S_{ik}S_{kj} + \Omega_{ik}\Omega kj = \boldsymbol{S}^2 + \boldsymbol{\Omega}^2 \ . \tag{2.25}$$

If p is to have a pressure minimum in the plane, at least two of the hessian's eigenvalues have to be negative(Jeong and Hussain, 1995). I.e., if the eigenvalues of $\boldsymbol{S}^2 + \boldsymbol{\Omega}^2$ are defined as $\lambda_1 \geq \lambda_2 \geq \lambda_3$, it requires that $\lambda_2 < 0$. Note, $\boldsymbol{S}^2 + \boldsymbol{\Omega}^2$ is real and symmetric and will have three real eigenvalues.

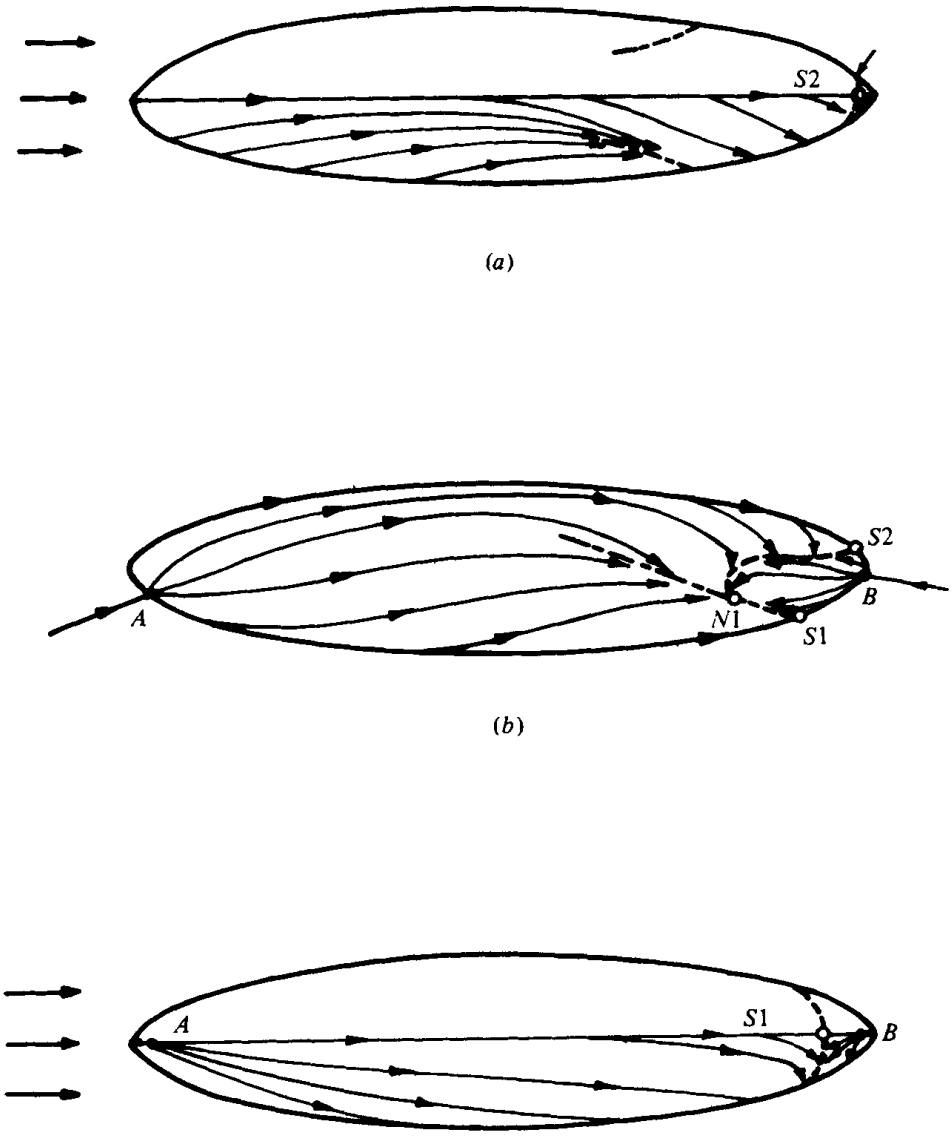

FIGURE 9. Surface flow pattern at moderate incidence (α = 10°): (*a*) top view; (*b*) side view; (*c*) bottom view). ——, surface streamlines; – – –, closed separation; —·—, open separation.

Figure 2.5: Flow separation types at 10° incidence with 3:4 aspect ratio and $Re = 60\ 000$ (Han and Patel, 1979).

Prolate Spheroids at Incidence

Prolate spheroids are well defined bodies of revolution, where the polar axis is larger than the equatorial diameter. When the body is inclined relative to the inflow, flow separation is observed at moderate Reynolds numbers (Jiang et al., 2014). Due to its geometrical simplicity, it has been considered as ideal to investigate three-dimensional separation (Jiang et al., 2014).

As identified in Han and Patel (1979), the flow separation of the prolate spheroid typically consists of both open and closed separation. In early experimental studies, surface shear stresses and velocity distributions in its near wall region were investigated (Han and Patel, 1979) (Fu et al., 1994). In Figure 2.5, streamlines and separation types and locations are indicated for a 10° incidence angle. The flow was assumed to be symmetric about the meridonial and was investigated at incidence angles up to 30°.

In Simpson (1996), separation and near wall velocities were investigated at low incidence angles ($\leq 20°$) and high Reynolds numbers ($\sim 10^6$). The locations of open and closed separation were identified. Additionally, the near wall LDA velocity measurements showed that the near-wall turbulence is anisotropic and thus not comply with the RANS Bousinessq approximation. This is to be expected given the discussion on anisotropy of curved, 3D flows in Wilcox (2006).

In Jiang et al. (2014), the 6:1 spheroid at 45° incidence was investigated at Reynolds numbers 50, 200, 1000. For the two lowest Reynolds numbers, the entire flow is laminar, steady and symmetric about the meridionial plane. Open separation is identified as the dominating separation type for all Reynolds number configurations. The wake is characterized by a counter-rotating vortex pair, which size goes from a minimum at the lower pole to a maximum at the upper pole. At $Re = 1000$, the flow is symmetric about the meridionial plain in the near-body wake. The wake is dominated by a counter rotating vortex pair, which becomes distinctly asymmetric at $x = 4 - 5D$ (cf. Figure 2.7). The wake remains steady until $x = 14D$, where it varies at Strouhals number 0.15. As this is in the range of naturally occurring unsteadiness in bluff-body wakes, it is suggested that the wake is on the verge of becoming unsteady.

Jiang et al. (2015) is a continuation of Jiang et al. (2014), where the unsteadiness and asymmetry of the wake were of particular interest. The configuration is studied at $Re = 3000$, where the wake is in the transitional regime, and is unsteady and highly asymmetric. The resulting sideway force is substantial with a mean of 75% of the mean drag force. Note, the asymmetry do not change in time; the side force do not oscillate about a zero mean, as seen with the von Kármán vortex street for a circular cylinder. No vortex shedding was observed and the upper vortex structures disintegrated into numerous minor structures just downstream of separation. A vortex tube emerged at the lower pole and stayed intact approximately seven diameters downstream (cf. Figure 2.8). The unsteadiness is occurring at the very low St=0.0733, and is assigned to three-dimensional wake effects. The asymmetry of the flow is ascribed to a global instability, which signifies that the instability is inherent in the wake itself. It is argued that this instability is triggered at approximately $Re = 1000$ and is characteristic for higher Reynolds numbers for this configuration.

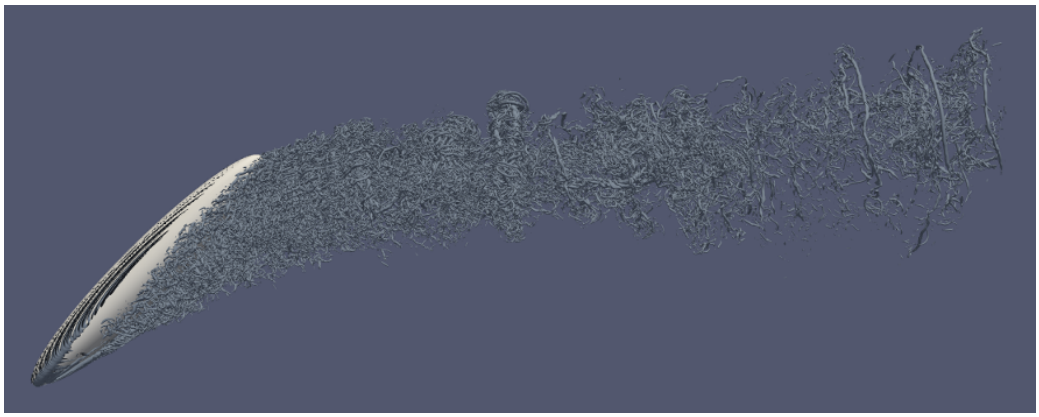

Figure 2.6: Preliminary DNS. $Re = 16000,\ \lambda_2 \in [-2000, -200]$ - contours.

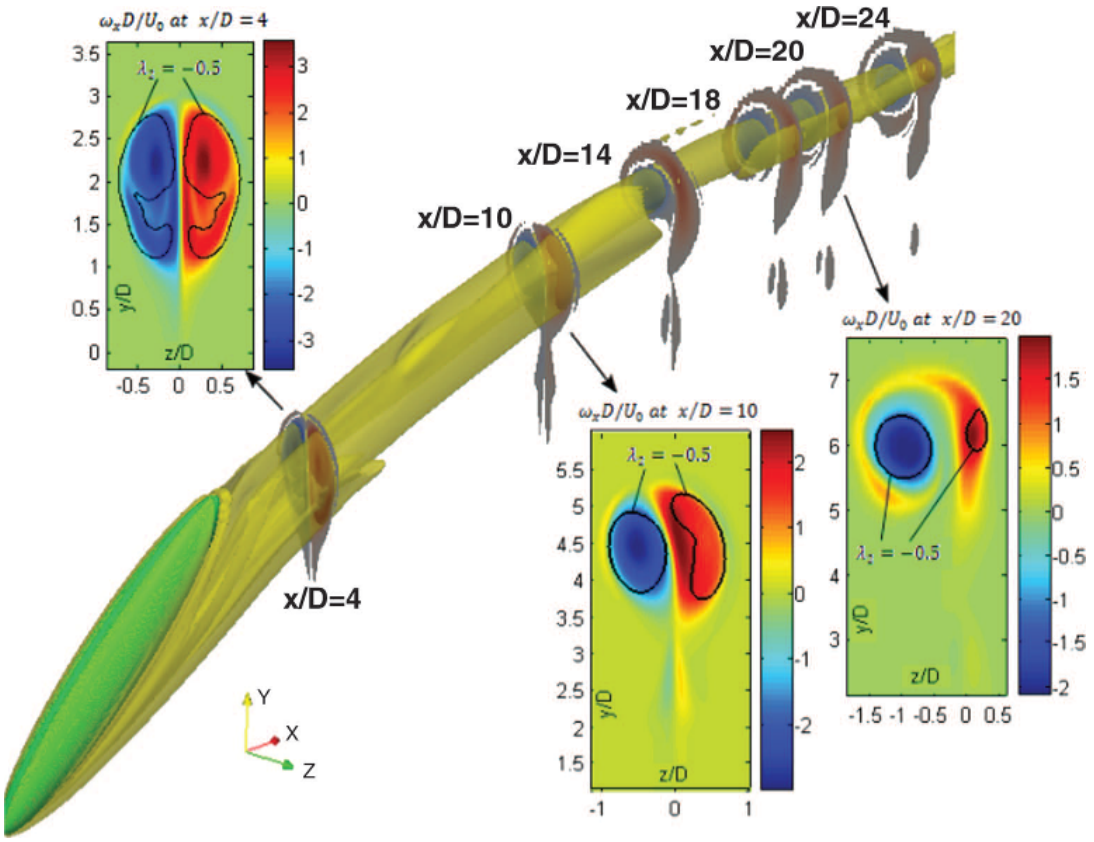

Figure 2.7: $Re = 1000$. $\lambda_2 = -0.5$ - and $\omega_x D/U_0$ -contours (Jiang et al., 2014).

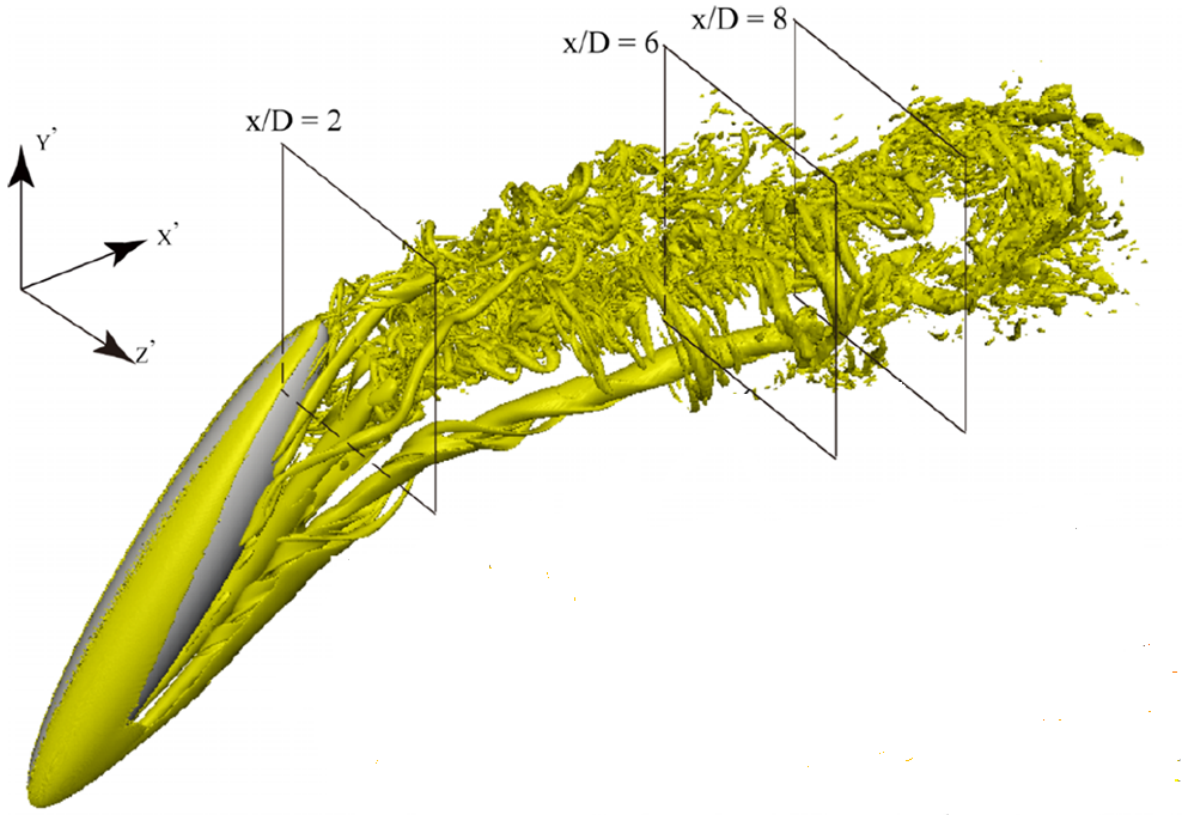

Figure 2.8: $Re = 3000$. $\lambda_2 = -15$ - contours(Jiang et al., 2015).

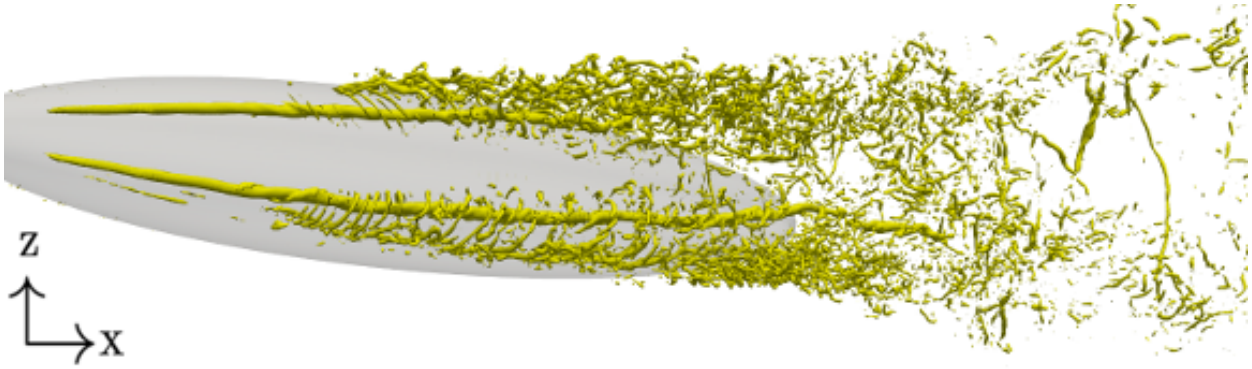

Figure 2.9: Preliminary DNS. $Re = 16000$. Near-body flow topology. Bottom view.

The DNS study at $Re = 16000$ was yet to finish as this thesis was concluded. Thus, the ensuing analysis by the undersigned is based on the preliminary results of this work, where the data from an instantaneous flow field has been investigated (i.e., data which is not statistical representative of the flow). At this point, the flow was fully developed and is assumed suitable for a qualitative assessment of the flow. Cf. section 3.2 and Figure 3.1 for a description of the computational domain and respective coordinate systems.

Figures 2.6, 2.9 and 2.10 show an overview of the flow topology at $Re = 16000$. The global instability identified in Jiang et al. (2015) is still present, as the flow is still highly asymmetric. However, there are major differences in force resultants and wake topology (cf. Table 4.3b and Figure 2.11). There is a reduction in the drag force($\sim 10\%$) and the Strouhals number is approximately half that predicted at $Re = 3000$. The reduction in drag force with increased Reynolds number is indicative of the flow entering a turbulent flow regime; this development is seen for bodies as the smooth circular cylinder and sphere (Kundu et al., 2012). The reduction in Strouhals number is also seen for the circular cylinder during transition to the fully turbulent flow regime (Sumer and Fredsøe, 1997).

The counter-rotating vortex pair originating at the spheroid's lower pole is an important aspect of the flow (cf. Figure 2.9). Crossflow instabilities, curvature and resulting open separation are attributed to the creation of these structures. In addition, note the helical structures surrounding the vortex pair; smaller scale structures are convected into the wake, where the vorticity of the dominating pair gives rise to the helix. This initial topology can further be studied in Figure 2.12a, where the distribution of $\omega_x D/U_0$ at $\bar{\eta} = -0.6$ is given. At this point, there is a small asymmetry in the wake in terms of positioning and intensity; the wake-side vortex(yellow encircling)) has a maximum 3% below the opposing vortex(green encircling).

With increasing Re_{η^*}, the wake topology becomes more chaotic. It is assumed that Kelvin-Helmholtz(KH) (Drazin, 2002) instabilities are formed at the spheroid pressure side (the side with body normal facing upstream)(Personal communication with Håkon Strandnes; April 26th 2018). As these small-scale instabilities are convected into the wake, their accumulated disturbance on the initial topology increases with Re_{η^*}. This effect combined with the separation induced instabilities at the upper pole causes a complicated wake topology. Due to the asymmetry of the flow, the effect of the KH-instabilities is at first most distinguishable at the wake-side; the wake-side primary vortex disintegrates at approximately $x = 1.4D$, while the opposing primary vortex disintegrates at approximately $x = 3.2D$. Figure 2.12b gives an image of the topology at $\eta = 0.6$, $\bar{x} = 1.3D$. The primary vortex pair are still noticeable (cf. encirclings), but smaller scales structures have comparable intensities.

In the intermediate wake, depicted in Figure 2.13, two groupings of vortices can be observed. At $x = 4D$, these groupings are quite distinguishable, but moving downstream they interact and gradually unite. The green grouping is the result of the the wake-side primary vortex and its attracted smaller scale structures. The other grouping is similar in its origin, but is larger in scale and intensity, as this also includes instabilities triggered due to separation at the spheroid's upper pole.

Figure 2.10: Preliminary DNS. $\lambda_2 \in [-2000, -250]$ - contours.

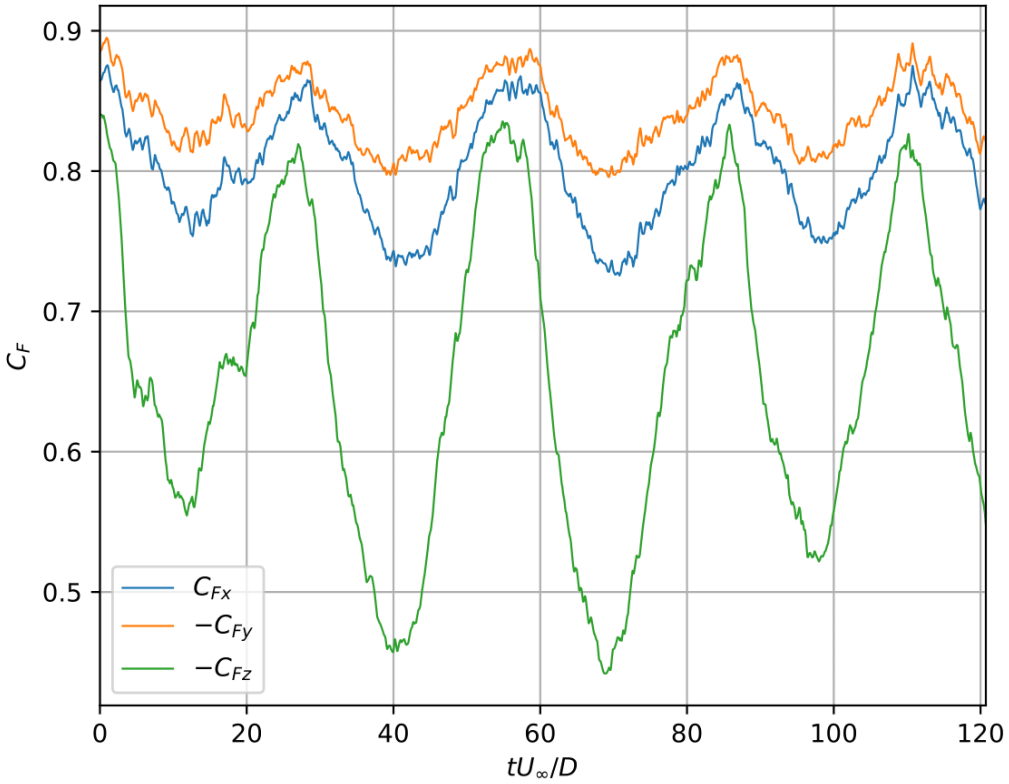

Figure 2.11: Preliminary DNS. $\lambda_2 \in [-2000, -250]$ -contours. Bottom view.

Table 2.1: Preliminary DNS force coefficient statistics.

	CF_X	CF_Y	CF_Z	St
Average	0.79	-0.83	0.66	0.035
RMS	0.80	0.84	0.67	-

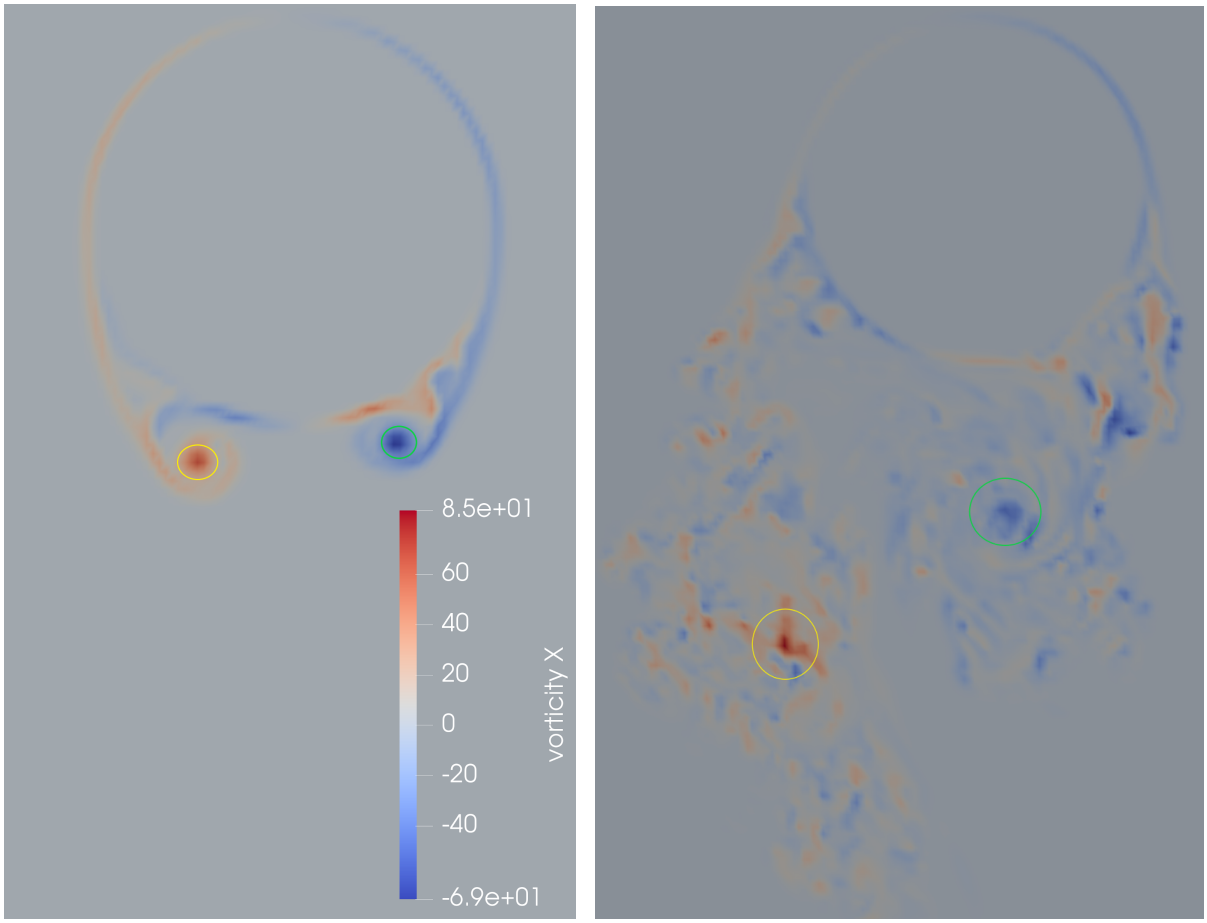

(a) $\bar{\eta} = -0.6$. (b) $\bar{\eta} = 0.6$.

Figure 2.12: Preliminary DNS. $\omega_x D/U_0$ in the $\xi - z$ plane. Facing negative η - direction.

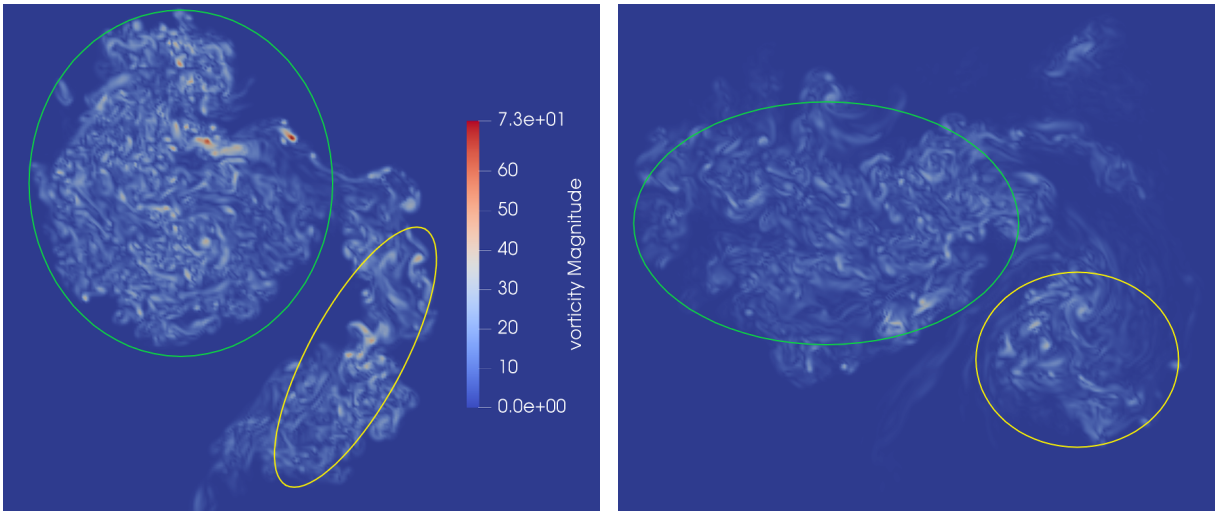

(a) $x = 4D$. (b) $x = 8D$.

Figure 2.13: Preliminary DNS. $\sqrt{\omega_i \omega_i} D/U_0$ in the $y - z$ plane. Facing positive x - direction.

2.3 Turbulence Modelling

In the following, the turbulence models used in this study are presented. They are selected based on the work in Larssen (2017) (cf. Appendix C for an extract) and discussions with my supervisors. From Larssen (2017), the following models were identified as appropriate for modelling of separating bluff body flows: $k-\omega\ SST$, $BSL-EARSM$, $k-\omega\ SST\ SAS$, $k-\omega\ SST\ DES$. Note, besides suitability, models were selected to represent a distinct class of turbulence models. I.e., $k-\omega\ SST$ represents the most robust and accurate of the isotropic RANS models (Larssen, 2017). Similarly, $BSL-EARSM$ represents an anisotropic RANS model, while the two latter represents different type of hybrid models. In this study, a hybrid model denotes a model that has a RANS- and a LES-mode.

The anisotropic RANS model $BSL-EARSM$ is not included in OpenFOAMv5.0, so this model was disregarded. As laminar-turbulent transition is highly important in this test case (cf. section 2.2), the transition model $k-\omega\ SSTLM$ has been included. My supervisors suspected that the above models to not be of sufficiently complexity to replicate the flow features, as the anisotropy and unsteadiness of the flow would not be resolved correctly by RANS or hybrid models (cf. section 2.2). Especially, the small scale features at the nose of the spheroid are believed to be of big importance for the wake dynamics and it was deemed likely that hybrid models are in RANS mode at this point. Hence, the Smagorinsky LES model has been included. This model was chosen as it has proved to work successfully in the qualitatively similar flow studied in Li et al. (2018). However, it is not well suited to predict natural transition (Ducros et al., 1998), and thus the Wall-adapting local-eddy viscosity (WALE) LES model was also included.

$k-\omega\ SST$

Common for most RANS two equation models is a model equation for k. This transport equation is established from modelling the exact equation for k (Wilcox, 1998). In establishing this equation, viscous diffusion is neglected and the diffusion of k is modelled by a gradient-diffusion model. To connect ν_t to k, a local mixing length model is used

$$\nu_t = C_\mu \sqrt{k} L \ . \tag{2.26}$$

This follows from dimensional arguments, where L is a turbulence length scale (Jones and Launder, 1972) and C_μ is a constant. To determine ν_t, the turbulent length scale must be determined and hence a second transport equation is introduced (Wilcox, 1998). There are two prominent examples in this case: the dissipation rate of turbulent kinetic energy $\epsilon = C_D \frac{k^{3/2}}{L}$ ($k-\epsilon$ model) and the specific dissipation rate of turbulent kinetic energy $\omega = \frac{\sqrt{k}}{L}$ ($k-\omega$ model). These two transport equations are based on arguments regarding the physical processes in a flow and dimensional analysis. With this approach important physical processes may not be taken into account (Menter and Egorov, 2010).

Following validation studies, it has become apparent that the $k-\omega$ model is accurate close to walls, but very sensitive to freestream boundary conditions (Menter et al., 2003). The $k-\epsilon$ model has been shown to be good in the freestream and bad close to walls. Hence, as these two models complement each other, Menter (1993) proposed a mixing of the two, the $k-\omega\ SST$ turbulence model. In this model, blending functions are used to switch to the $k-\epsilon$ model in the freestream and to the $k-\omega$ model close to walls. The model formulation in OpenFOAMv5.0 is given as (OpenCFD, 2018*a*)

$$\frac{D\rho k}{Dt} = \widetilde{P_k} - \beta^* \rho\omega k + \frac{\partial}{\partial x_j}[(\mu + \sigma_k \mu_t)\frac{\partial k}{\partial x_j}] \ , \tag{2.27}$$

$$\frac{D\rho\omega}{Dt} = \alpha\rho S^2 - \beta\rho\omega^2 + \frac{\partial}{\partial x_j}[(\mu+\mu_t)\frac{\partial \omega}{\partial x_j}] + 2(1-F_1\rho\sigma_{\omega 2})\frac{1}{\omega}\frac{\partial k}{\partial x_j}\frac{\partial \omega}{\partial x_j} \ , \tag{2.28}$$

$$\nu_t = \frac{a_1 k}{max\{a_1\omega, SF_2\}} \ , \qquad S = \sqrt{2S_{ij}S_{ij}} \ , \tag{2.29}$$

$$P_k = \mu_t \frac{\partial U_i}{\partial x_j}\Big(\frac{\partial U_i}{\partial x_j} + \frac{\partial U_j}{\partial x_i}\Big) \ , \qquad \widetilde{P_k} = min(P_k, 10\beta^* \rho k \omega) \ , \tag{2.30}$$

where $\frac{D}{Dt}\{\}$ denotes the material derivative (Kundu et al., 2012). The blending functions F_1 and F_2 and the constants $\beta, \beta^*, \sigma_k, \sigma_\omega, \sigma_{\omega_2}, \alpha, a_1$ are given in Menter et al. (2003). As this model can be integrated down to the viscous sublayer, it may be used as a so-called low Re number turbulence model (cf. section 2.2).

In Eça et al. (2016), it is identified that the $k-\omega$ SST model does not accurately predict flows, where laminar-turbulent transition is important (cf. section 2.2).

$k-\omega$ SSTLM

Due to the shortfalls in transition prediction modelling of conventional two equation models, transition models have been developed (Eça et al., 2016). A prominent example is the $k-\omega$ $SSTLM$ model, which combines the $k-\omega$ SST model with transport equations for intermittency γ and the momentum-thickness Reynolds number Re_θ (Langtry and Menter, 2009). As Re_θ is an integral quantity, the variable is unsuitable for implementation in a general purpose CFD code. Thus, experimental correlations between the locally calculated vorticity Reynolds number Re_v and Re_θ for a flat plate boundary layer is applied (y-coordinate is orthogonal to the body)

$$Re_v = \rho \frac{y^2}{\mu} S \ , \qquad S = \sqrt{2 S_{ij} S_{ij}} \ , \qquad Re_\theta = \frac{\underset{y}{max}(Re_v)}{2.193} \ . \tag{2.31}$$

Empirical correlations between Re_v and Re_θ are used to estimate natural and separation-induced separation (cf. section 2.2). Note, the model implemented in OpenFOAMv5.0 does not contain the crossflow modification introduced in Watanabe et al. (2009). The rationale behind the $k-\omega$ $SSTLM$ model is that the local quantity Re_v is connected to Re_θ empirically, which is used to determine the production of intermittency, signifying local transition. Followingly, the intermittency works as a switch for the production of turbulent kinetic energy k.

In Eça et al. (2016), the $k-\omega$ $SSTLM$ model shows better agreement with experiments than regular two equation models, but it is shown that the results are highly dependent on the inlet boundary conditions of Re_θ.

$k-\omega$ SST SAS

An alternative to using ϵ or ω in the scale determining equation is kL. Rotta (1972) first established the exact equation for kL and later modelled it to an applicable scale determining equation. However, due to difficulties in calibrating it to the law of the wall (cf. section 2.2), the $k-\epsilon$ model was in the early 70's chosen as the preferred model (Menter and Egorov, 2010). In Menter and Egorov (2010), the kL equation is revisited and an alternative modelling of the source term is performed. This new model may be calibrated to the law of the wall, and more importantly, also introduces a new type of source term not seen in the ω or ϵ model equations. This source term depends on the von Kármán length scale (y-coordinate is orthogonal to body)

$$L_{vk} = \kappa \left| \frac{\partial U / \partial y}{\partial^2 U / \partial y^2} \right| \ . \tag{2.32}$$

This term causes scale determination also from smaller scales. I.e., with spatially varying strain rates, L_{vk} will vary, which in turn causes different turnover frequencies, ω, and potentially a vast range of different vortex structures. In this case, the scale determination is dependent on the flow, and it is hence termed scale-adaptive and thereof the model name, scale-adaptive simulation (SAS). This is in contrast to conventional two equation models, where the turbulent length scale is proportional to the integral length scale $L \sim \delta$, where δ is the thickness of the turbulent layer (boundary layer thickness in a shear flow) (Menter and Egorov, 2010). This is appropriate for steady shear flows, but not for unsteady flows, where it damps out resolved smaller scales. Menter and Egorov (2010) explains this by considering that in conventional two equation models, only the

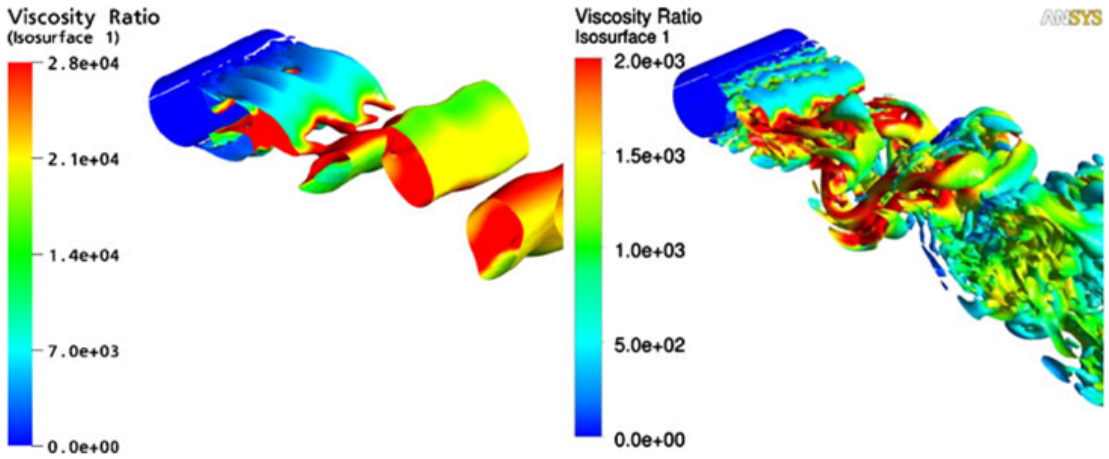

Figure 2.14: Q-contours colored with the eddy viscosity ratio μ_t/μ. $k-\omega$ SST left and $k-\omega$ SST SAS right (Menter and Egorov, 2010)

shear strain is input, which yields the determination of ω. As no more information is provided, as with L_{vk} in $k-\omega$ SST SAS, the above determination of L results. This behavior is clearly seen in Figure 2.14 from Menter and Egorov (2010), where only the primary vortex shedding mode is present for $k-\omega$.

Given that the additional source term is included in a scale determining equation for kL, Menter and Egorov (2010) deems it reasonable that they are to be included in the transport equations for ϵ and ω. Thus, this type of term is introduced into the $k-\omega$ SST model, and the result is the $k-\omega$ SST SAS model. The only difference from the $k-\omega$ SST model is the following term added to the right hand side of the scale determining equation (2.28)

$$Q_{SAS} = \max\Big[\rho\zeta_2 S^2 \Big(\frac{L}{L_{vk}}\Big)^2 - \frac{4\rho k}{\sigma_\Phi}\max\Big(\frac{1}{k^2}\frac{\partial k}{\partial x_j}\frac{\partial k}{\partial x_j}, \frac{1}{\omega^2}\frac{\partial \omega}{\partial x_j}\frac{\partial \omega}{\partial x_j}\Big), 0\Big] \ . \tag{2.33}$$

One issue identified with this model is that the scale adaptive production is only active with a large degree of unsteadiness. Hence, the model may stay in RANS mode for flows that are moderately unsteady and not predict transition from smaller scale instabilities (Menter and Egorov, 2010). An advantage of $k-\omega$ SST SAS to most other hybrid formulations is the switch from RANS to a scale resolving simulation (SRS), which do not have an explicit dependence on grid spacing (Menter and Egorov, 2010).

$k-\omega$ SST DES

In a delayed eddy simulation (DES), a RANS model is used in the attached boundary layer, while a LES model is used in the detached regions. The rationale is to avoid the large computational cost of solving the near wall region with LES and to use LES in the detached unsteady region, which is unsuitable for RANS (Spalart et al., 1997). However, there are some conceptual concerns with DES, as the flow is transferred between regions with different filters. That aside, DES was first developed for the Spalart-Allmaras model and was later developed for $k-\omega$ SST. A major issue with DES is the switch from RANS to SRS mode. It has been shown that this may produce premature separation, and this is denoted as Grid Induced Separation (GIS) (Menter et al., 2003). There have been extensive efforts to remove this deficiency, which have resulted in delayed DES(DDES) (Shur et al., 2008). Unfortunately, this model is yet to be implemented in OpenFOAMv5.0, and the conventional DES formulation has been used. In DES, the switching between RANS and LES is performed with altering the length scale in the dissipation term in the k transport equation. The formulation used in OpenFOAMv5.0 reads (OpenCFD, 2018*b*)

$$D^k_{RANS} = \rho k^{3/2}/L_{RANS} \ , \qquad L_{RANS} = \frac{\sqrt{k}}{C_\mu \omega} \ , \tag{2.34}$$

is altered to

$$D^k_{DES} = \rho k^{3/2}/L_{DES} \ , \qquad L_{DES} = min(L_{RANS}, C_{DES}\Delta) \ , \tag{2.35}$$

where Δ is the LES filter width (cf. 'Smagorinsky' below). Thus, in the LES region the method switches to a Smagorinsky SGS model.

Smagorinsky

The Smagorinsky SGS model (Smagorinsky, 1963) (Versteeg and Malalasekera, 2007) formulation is given as

$$\tau_{ij} = 2\nu_t S_{ij} - \frac{1}{3}\delta_{ij}\tau_{kk} \ , \tag{2.36}$$

where the eddy viscosity is specified as

$$\nu_t = (C_s\Delta)^2|S_{ij}| \ , \tag{2.37}$$

and C_s is a constant. There are numerous definitions of the filter width Δ, but a very common one utilized in this study, is the cube root volume filter

$$\Delta = (\Delta x \Delta y \Delta z)^{\frac{1}{3}} \ . \tag{2.38}$$

Note that ν_t is proportional to the grid spacing squared, which follows from the work of Lily (Pope, 2000). This is in correspondence with Kolmogorov's theory, where the energy content, and thus also the dissipation, is decreasing with scale size in the inertial subrange. A problem with this model is that ν_t is produced also for laminar boundary layer profiles. This disrupts the evolution of linearly unstable waves and hence also transition modelling (Ducros et al., 1998). This is related to the Smagorinsky constant C_s being dependent on the flow regime. In the Dynamic model, this problem is resolved by making C_s a local flow variable(Germano et al., 1991). However, this model introduces a second filtering and requires stabilization (Pope, 2000).

WALE

In WALE, the erroneous transition modelling of the Smagorisnky model is addressed with an alternative modelling of ν_t(Ducros et al., 1998)

$$\nu_t = (C_m\Delta)^2 \frac{(S^d_{ij}S^d_{ij})^{3/2}}{(S_{ij}S_{ij})^{5/2} + (S^d_{ij}S^d_{ij})^{5/4}} \ , \tag{2.39}$$

where C_m is a constant and

$$S^d_{ij} = \frac{1}{2}(g^2_{ij} + g^2_{ji}) - \frac{1}{3}\delta_{ij}g^2_{kk} \ , \qquad g_{ij} = \frac{\partial U_i}{\partial x_j} \ . \tag{2.40}$$

With the above model formulation, no turbulent viscosity is produced in the laminar boundary layer, yielding an improved transition modelling to the Smagorinsky model. Away from the body, the modelling is identical to the Smagorinsky model (Ducros et al., 1998).

2.4 Computational Fluid Dynamics

In CFD, a fluid flow problem is solved by a numerical solution of some set of model equations. In this study, the model equations constitute Eqs. (2.3)-(2.4) and one of the turbulence models outlined in the previous section. There are numerous approaches to solving these equations, but in this study the Finite Volume Method (FVM) is applied. Below, the method is described in brief and thereafter follows a description of the method's error sources. Estimation and control of these error sources are of high importance in V&V in CFD.

The Finite Volume Method

FVM for incompressible, viscous flow is derived from the integral form of Eqs. (2.1)-(2.3)

$$\int_{\partial\Omega} \rho \boldsymbol{u}' \cdot \boldsymbol{n} \; dA = 0 \; , \tag{2.41}$$

$$\begin{aligned} \int_{\Omega} \int_{t}^{t+\Delta t} \frac{\partial \rho \boldsymbol{u}'}{\partial t} \; dt \; dV + \int_{t}^{t+\Delta t} \int_{\partial\Omega} \rho \boldsymbol{u}' (\boldsymbol{u}' \cdot \boldsymbol{n}) \; dA \; dt = \\ - \int_{t}^{t+\Delta t} \int_{\partial\Omega} p' \boldsymbol{n} \; dA \; dt + \int_{t}^{t+\Delta t} \int_{\partial\Omega} (\mu \nabla \boldsymbol{u}') \cdot \boldsymbol{n} \; dA \; dt + \int_{t}^{t+\Delta t} \int_{\Omega} \rho \boldsymbol{f}' \; dV \; dt \; , \end{aligned} \tag{2.42}$$

where Ω denotes a finite control volume, $\partial\Omega$ its boundary and Δt a finite time step (Versteeg and Malalasekera, 2007). In FVM, the entire flow domain is subdivided into numerous control volumes, which are denoted cells (Versteeg and Malalasekera, 2007). In each cell, the flow variables are given a discrete location (e.g. at the faces or the cell center). Given this formulation, the above equations may be approximated by the use of these discrete values. I.e., face values may be interpolated by use of cell values or vice versa, and derivatives may be approximated by finite differences. Hence, for each cell, a non-linear system of equations are expressed in terms of the discrete flow variables (the second term from the left hand side in Eq. 2.42 is non-linear). Further, as Eqs. 2.41 and 2.42 constitute an elliptic-parabolic system of PDEs (Müller, 2017), boundary conditions need to be prescribed at all boundaries. This also holds for turbulent transport quantities as k or ω. The boundary conditions may be prescribed in the form of values (Dirichlet) or gradients (Neumann) (Kreyszig et al., 2015).

To solve this non-linear algebraic system of equations, an iterative procedure is used (Versteeg and Malalasekera, 2007). I.e., p' and $\boldsymbol{u}'$ are guessed at initiation; the convective fluxes are approximated with the guessed field u'^{*}, resulting in a linear system for updated velocities $\boldsymbol{u}'$. However, the solution of the discretized equations, denoted a predictor step, do usually not satisfy mass conservation. Thus, corrections to $\boldsymbol{u}'$ and $\boldsymbol{p}'$ are needed.

In the original pressure-correction algorithm SIMPLE by Spalding and Patankar (Patankar and Spalding, 1972), Eq. (2.42) is simplified to generate a direct coupling between pressure corrections and velocity corrections. These relations are inserted into Eq. (2.41) to generate a Poisson-like equation for the pressure corrections. After solving this equation the pressure and the velocities may be corrected (a corrector step). This procedure continues until convergence, where the continuity error may be used in a convergence requirement. After convergence, the equations are integrated in time and the procedure is repeated at the new time step. This process continues until the simulation reaches the end time.

Another prominent pressure-correction algorithm is PISO (Versteeg and Malalasekera, 2007). This is an extension of SIMPLE, where the predictor and corrector step is followed by a second corrector step. A schematic description of the PISO algorithm is given in Figure 2.15. This figure depicts how PISO is used to solve one time step.

Solving the filtered equations is algorithmically very similar to solving the unfiltered ones. Turbulent quantities are guessed at initiation, and after finishing the final corrector step, transport equations for the turbulent properties, e.g. k and ω, are solved. However, the inclusion of turbulent quantities generally slows down convergence, and grid requirements, especially in hybrid methods and LES, may introduce numerous numerical difficulties (Jasak, 2018).

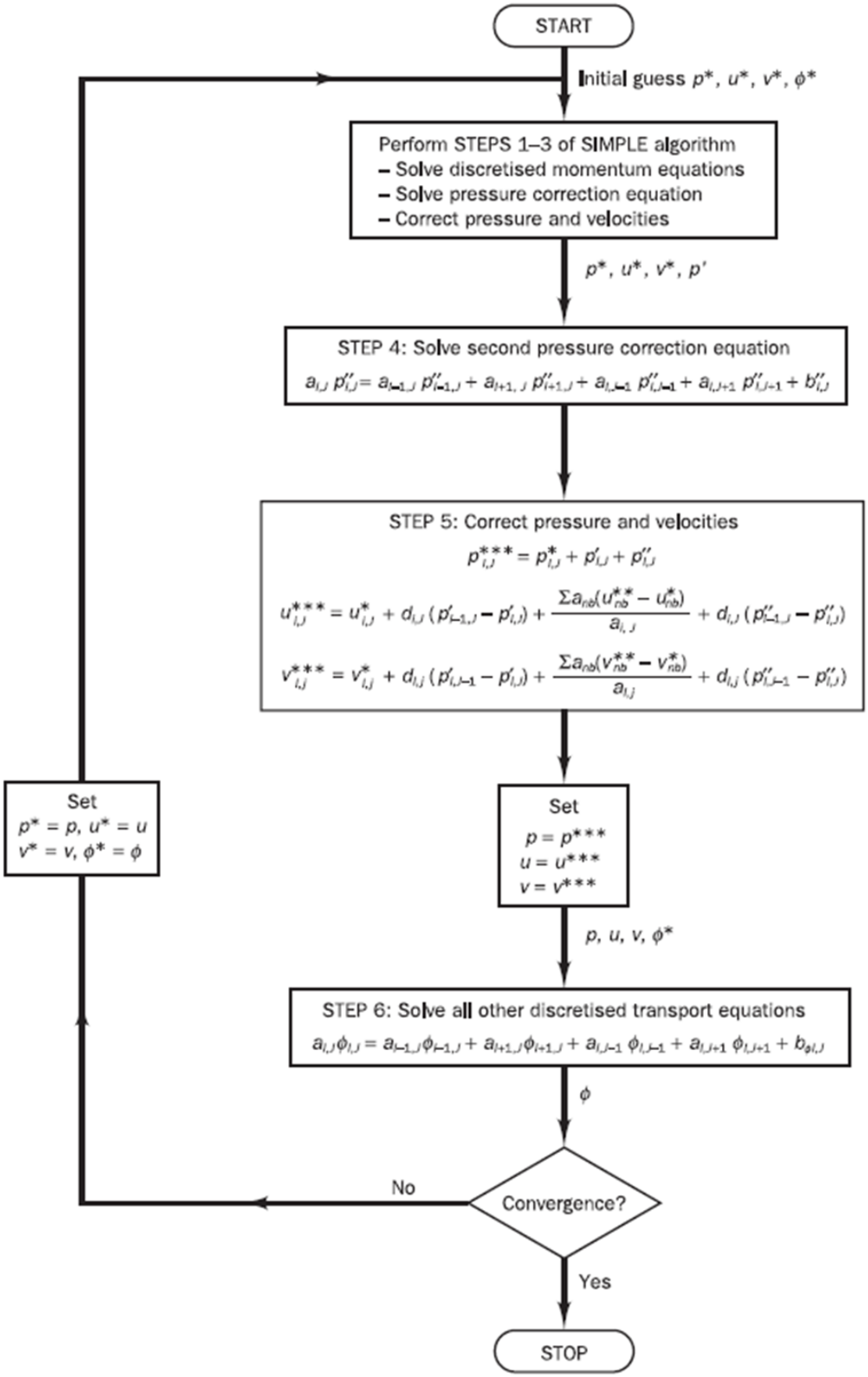

Figure 2.15: Flowchart of the PISO algorithm (Versteeg and Malalasekera, 2007)

Numerical Errors in FVM

In applying FVM to solve the filtered equations and a turbulence model, there will be numerical errors (cf. next section for the definition of an error). The total error may be subdivided into three categories (Eça and Hoekstra, 2009)

- Round-off error
- Iterative error
- Discretization error

Round-off error follows the finite computer precision. With double precision as applied in OpenFOAMv5.0, Eça and Hoekstra (2009) state that for smooth flows this error is negligible compared to the two other sources.

The iterative solution of linear systems of equations and the iterative correction methods introduce a numerical error. As mentioned in the previous section, these iterative procedures are due to the non-linearity of the systems of equations. The iterative error may be monitored by a norm of the residual, and the residual is defined as

$$\boldsymbol{r} = \boldsymbol{A}\boldsymbol{\phi} - \boldsymbol{b} \ , \tag{2.43}$$

where $\boldsymbol{A}\boldsymbol{\phi} = \boldsymbol{b}$ is the linear system under investigation. Alternatively, the error may be monitored by the norm of the change from one iteration to the next. Three examples of norms are the L_∞-norm, the L_{RMS}-norm and the L_1-norm, which read

$$L_\infty = \underset{i}{\mathrm{MAX}}(|\boldsymbol{\phi}_i^{(n)} - \boldsymbol{\phi}_i^{(n-1)}|) \ , \quad L_{RMS} = \sqrt{\frac{\sum_{i=1}^{N_p}(\boldsymbol{\phi}_i^{(n)} - \boldsymbol{\phi}_i^{(n-1)})^2}{N_p}} \ , \tag{2.44}$$

$$L_1 = \frac{1}{N_p}\sum_{i=1}^{N_p}|\boldsymbol{\phi}_i^{(n)} - \boldsymbol{\phi}_i^{(n-1)}| \ , \qquad 1 < i < N_p \ , \tag{2.45}$$

where N_p is the total number of grid points and n is the iteration counter. The L_1-norm of the residual or its relative change is used as default in OpenFOAMv5.0 to estimate iterative convergence (OpenCFD, 2018*c*).

The discretization error is caused by the fact that one can only use a finite number of control volumes (Roache, 1998). Dependent on the chosen discretization, e.g. a cell-based FVM, the discretized equations include flow quantities and derivatives at faces. Thus, these must be approximated by use of interpolation and finite differences, respectively. Dependent on the scheme, these errors are proportional to the grid spacing by some order p. E.g., the central FVM is 2nd order accurate, while the standard upwind method is first order accurate (Versteeg and Malalasekera, 2007). Thus, as the grid spacing are refined, the discretization error is reduced. However, the observed convergence order is usually lower than the theoretical order for complex flows. This difference is due to effects of boundary conditions, turbulence modelling and other aspects affecting the numerical solution. The method to calculate the observed order of convergence is given in the next section along with the use of Richardson extrapolation to estimate extrapolated flow variables. Additionally, a method that estimates the numerical uncertainty caused by the discretization errors is presented.

In estimating the discretization error, an inherent assumption in all such methods is that iterative errors are negligible compared to the discretization errors. To establish the accuracy of this assumption for a given simulation, a criterion is developed in Eça and Hoekstra (2009). The method of manufactured solutions (Roache, 1998) was used to obtain values for iterative and discretization errors, and this was utilized to establish a criterion for a negligible iterative error. The investigation showed that the iterative error measured with L_∞-norm is a good estimator; the iterative error do not affect the observed convergence order if the L_∞-norm is 2-3 orders of magnitude lower than the estimated discretization error (cf. next section). Additionally, it was shown that the L_{RMS}-norm was not an accurate estimator for the iterative error.

2.5 Verification and Validation in ASME V&V 20-2009

Verification and Validation (V&V) in CFD concerns assessing the accuracy of a numerical simulation (Roache, 1998). In this context, verification involves determining whether a code correctly solves the incorporated mathematical model. When this is established, code validation can be pursued. This process aims to assess whether the incorporated mathematical model adequately represents the physical problem. Before providing a more detailed account of this process, the following introduces definitions used in ASME (2009), which are adopted in this study. Let D denote the experimental value, S the simulated value and T the true value of some quantity. Further, the validation comparison error is defined as

$$E = S - D \ . \tag{2.46}$$

The error in S and D are defined as

$$\delta_S = S - T \quad , \quad \delta_D = D - T \ . \tag{2.47}$$

Combining (2.46) and (2.47) yield

$$E = \delta_S - \delta_D \ . \tag{2.48}$$

The errors in S can be subdivided into three categories:

- δ_{model} due to modelling approximations and assumptions
- δ_{input} due to errors in input parameters
- δ_{num} due to errors in the numerical solution of the equations (cf. previous section)

$$\delta_s = \delta_{model} + \delta_{input} + \delta_{num} \ . \tag{2.49}$$

Using the subdivision in Eq. (2.49), Eq. (2.48) may be rearranged to

$$\delta_{model} = E - (\delta_{num} + \delta_{input} - \delta_D) \ . \tag{2.50}$$

Further, a validation standard uncertainty u_{val} can be defined to represent the combined error of all the error terms. I.e.,

$$\delta_{model} \in [E - u_{val}, E + u_{val}] \ . \tag{2.51}$$

If the error terms are assumed independent, their respective uncertainties to a given confidence level is given as (ASME, 2009)

$$u_{val} = \sqrt{u_{num}^2 + u_{input}^2 + u_D^2} \ . \tag{2.52}$$

Conclusively, the process of establishing the model error interval to a certain confidence level consists of establishing the validation comparison error E and the uncertainties associated with the numerical solution, input parameters and experimental solution. In the following, this process is outlined.

Estimation of Numerical Uncertainty u_{num}

The first step in the verification process is denoted as code verification. This usually amounts to applying the method of manufactured solutions (ASME, 2009). By doing so, one may verify that the code solves the incorporated mathematical model correctly. This is a one-time affair performed after code completion. In the case of OpenFOAM and commercial CFD codes, this process has been performed.

After the code has been verified, solution verification follows. Given that all grids are able to resolve all scales of a simulation (flow and turbulence model dependent), a systematic grid refinement study is used to estimate a Richardson extrapolated value of S and u_{num}. That aside, if S is assumed to have a power series representation in the grid spacing metric h with dominating order p, p may be estimated from simulations on three grids (ASME, 2009). p is denoted as the observed order of convergence. It is a requirement that the grid refinement must be consistent throughout the grid. In this study, the grid spacing metric is defined as in ASME (2009), $h_i = [\frac{V}{N_i}]^{1/3}$. N_i denotes the total number of grid cells for a mesh indexed i and V is the volume of the flow domain. In this case, it is assumed that the power series may be truncated to the leading order term of order p; it is assumed that the grid is in the asymptotic range.
Followingly, the procedure for estimating p and the extrapolated value S^{ext} is given as
$h_1 < h_2 < h_3, \quad S_i = S(h_i), \quad r_{21} = h_2/h_1, \quad r_{32} = h_3/h_2, \quad \epsilon_{32} = S_3 - S_2$ and $\epsilon_{21} = S_2 - S_1$,

$$p = \frac{1}{lnr_{21}}[ln|\epsilon_{32}/\epsilon_{21}| + ln(\frac{r_{21}^p - sign(\epsilon_{32}/\epsilon_{21})}{r_{32}^p - sign(\epsilon_{32}/\epsilon_{21})}] \ . \tag{2.53}$$

Further, p is used to calculate the extrapolated value with use of Richardson extrapolation

$$S = S^{ext} = \frac{r_{21}^p S_1 - S_2}{r_{21}^p - 1} \ . \tag{2.54}$$

Lastly, the numerical uncertainty at 95% confidence is given by

$$u_{num} = GCI_{21} = \frac{Fs}{r_{21}^p - 1}|\tilde{\epsilon_{21}}| \ , \qquad \tilde{\epsilon_{21}} = S_1 - S_2 \ . \tag{2.55}$$

For three-grids and more, $Fs = 1.25$. This safety factor is empirical and is given in Roache (1998), following his case studies. The above quantity, u_{num}, is denoted as the grid convergence index (GCI).

Note, for complex CFD simulations, the required grid refinement may be very expensive, as the grid size for reaching the asymptotic range may be prohibitive (Eça and Hoekstra, 2014). Hence, Eça and Hoekstra (2014) developed an alternative approach, providing uncertainty estimates when the solution is not in the asymptotic range. To calculate an estimate of the uncertainty, more terms are included in the power series and it is determined by a least squares fit, requiring simulations on at least 4 grids. Based on the fit, the observed convergence order follows, which yields the extrapolated value and u_{num}.

Estimation of Parameter uncertainty u_{input}

There are two approaches to establish the input parameter uncertainty. The first method is denoted as the sensitivity coefficient method in ASME (2009). A first order Taylor series expansion in parameter space is used to estimate the input parameter uncertainty for n uncorrelated random input parameters

$$u_{input}^2 = \sum_{i=1}^{n}(\frac{\partial S}{\partial X_i}u_{X_i})^2 \ , \tag{2.56}$$

where X_i is as an input parameter and u_{X_i} is the corresponding standard uncertainty. The derivatives may be approximated by finite differences. E.g., by a central difference approximation, one has

$$\frac{\partial S}{\partial X_i} = \frac{S(X_1, .., X_i + \Delta X_i, ..., X_n) - S(X_1, .., X_i - \Delta X_i, ..., X_n)}{2\Delta X_i} + O(\Delta X_i^2) \ , \tag{2.57}$$

where ΔX_i is some appropriate finite step in input parameter X_i. By using central differences, $2n + 1$ simulations needs to be performed to estimate u_{input}. An alternative to the above method is using a Monte Carlo technique. Such a technique have the advantage of also capturing non-linear behavior in parameter space. However, this technique is often prohibitively expensive in CFD, as thousands of simulations may be needed to obtain statistical convergence (ASME, 2009).

Estimation of validation uncertainty u_D

Estimation of u_D from experimental data follows an established standard given in ASME (2014). As validation in this case is performed with DNS, this standard can not be utilized to estimate u_D. Further, ASME V&V 20 does not cover the use of DNS in validation. There is relatively little literature on this subject. If one make a similar subdivision of u_D as for δ_s (cf. (2.47))

$$\delta_D = \delta_{DNS} = \delta_{model} + \delta_{input} + \delta_{num} \ . \tag{2.58}$$

The modelling error in the incompressible Navier-Stokes equations is assumed negligible, $\delta_{model} = 0$. In the present DNS study, the inflow is laminar, and blockage effects are assumed negligible, resulting in no input parameter uncertainty, $\delta_{input} = 0$. However, the numerical error, δ_{num}, is still present. As discussed in Oliver et al. (2014), the estimation of this term is more complicated than in the RANS or LES case. If iterative errors and round-off errors are termed negligible, the numerical errors are only dependent on the discretization error. However, due to the high accuracy of DNS compared to RANS and LES, it is relevant to consider the finite statistical sampling of DNS statistics. In Oliver et al. (2014), Richardson extrapolation in a generalized Bayesian framework is used to include this effect. The authors note that the use of this procedure may not be tractable for large DNS simulations, but rather be used to develop best-practice guidelines and rule of thumb estimates. The study also included test cases, and amongst them, the wall channel flow at $Re_\tau = \frac{u_\tau \delta}{\nu} = 180$ in Hoyas and Jiménez (2008).

Validation Uncertainty and Multivariate Extension

After performing the above procedure, the model uncertainty for a given quantity may be established using Eqs. (2.52) and (2.51). Additionally, the different contributions to the model uncertainty may be compared to assess the most critical sources of uncertainty. I.e., should a more accurate experiment or a simulation be pursued to reduce u_{val}? In Hills (2005), the procedure is extended to multivariate problems with the metric

$$r = \sqrt{\boldsymbol{E}^{\boldsymbol{T}} \boldsymbol{V}_{\boldsymbol{val}}^{-\mathbf{1}} \boldsymbol{E}} \ , \tag{2.59}$$

where N validation comparison errors are assembled in the vector $\boldsymbol{E}$. $\boldsymbol{V_{val}}$ is the covariance matrix given by

$$\boldsymbol{V_{val}} = \boldsymbol{V_S} + \boldsymbol{V_D} + \boldsymbol{V_{input}} \ . \tag{2.60}$$

If numerical and experimental uncertainties are uncorrelated, $\boldsymbol{V_S}$ and $\boldsymbol{V_D}$ are diagonal matrices with entries u_{num}^2 and u_D^2, respectively. If the Sensitivity coefficient method is applied with n uncertain input parameters, $\boldsymbol{V_{input}}$ is given as

$$\boldsymbol{V_{input}} = \boldsymbol{X_S} \boldsymbol{V_l} \boldsymbol{X_S^T} \ , \tag{2.61}$$

where $\boldsymbol{V_l}$ is a $n \times n$ diagonal matrix with entries u_{X_i}. X_s is the $N \times n$ sensitivity matrix

$$\begin{bmatrix} \frac{\partial S_1}{\partial X_1} & \cdots & \frac{\partial S_1}{\partial X_n} \\ \vdots & \ddots & \vdots \\ \frac{\partial S_N}{\partial X_1} & \cdots & \frac{\partial S_N}{\partial X_n} \end{bmatrix} \ . \tag{2.62}$$

If the uncertainties of the N variables are estimated as normally distributed, r should be χ^2 distributed (Hills, 2005). Then, a reference value r_{ref} may be defined as the expected value plus one standard uncertainty

$$r_{ref} = \sqrt{N + \sqrt{2N}} \ . \tag{2.63}$$

If $r/r_{ref} > 1$, the modelling error are not consistent with the experimental observation. With $r/r_{ref} < 1$, the differences in simulation and experiments are within the level of u_{val}.

Chapter 3

Problem Setup

3.1 CFD Code

All simulations are performed in OpenFOAMv5.0, which is an open-source computational toolbox capable of simulating a wide variety of different fluid flow processes. Amongst others, it is able to simulate incompressible turbulent flows, applying RANS, hybrid and LES turbulence models. The finite volume method in OpenFOAM is using co-located storage and an unstructured polyhedral grid (OpenCFD, 2018*d*). The code is parallellized using message passing interfacing (MPI) and subdomain decomposition.

3.2 Computational Domain and Boundary Conditions

The configuration under study is a prolate spheroid with an aspect ratio of $\lambda = c/a = 6:1$, where 'c' denotes the half-length of the major axis while 'a' denotes the half-length of the minor axis. The spheroid is inclined 45° relative to the uniform inflow U_0. There are two coordinate systems in use, one global (x, y, z) and one body-fixed (η, ξ, z), both originating in the spheroid centroid (cf. Figure 3.1). Additionally, the body fixed coordinate system will only be utilized in its normalized form $(\bar{\eta}, \bar{\xi}, \bar{z})$, where the normalization is with the respective half-length (e.g. $\bar{\eta} = \eta/3D$). In addition, the coordinate transformation $\eta^* = \eta + c$ will be utilized in the non-dimensional form $Re_{\eta^*} = \eta^* D/U_0$ (similar to a flat plate Reynolds number).

The computational domain equals that used in the forthcoming DNS study, having dimensions $(51.5D \times 25D \times 27D)$ in the $x,\ y,\ z$ -directions, respectively. D denotes the minor axis of the spheroid (cf. Figure 3.1). The Reynolds number Re considered is 16000, where $Re = U_0 D/\nu$. The boundary conditions are depicted in Figures 3.2 and 3.3, and are further discussed in the following. They have been devised following the guidelines in Versteeg and Malalasekera (2007) and the earlier papers on this flow configuration for lower Reynolds numbers (Jiang et al., 2014) (Jiang et al., 2015).

Inlet Conditions

For all models, the streamwise velocity component at the inlet is prescribed to unity and the crosswise components are set equal to zero. The zero gradient condition is applied to the pressure. Regarding the turbulence quantities, the incoming flow is assumed laminar(similar to the DNS study). Hence, the Smagorinsky and WALE models are prescribed with zero ν_{SGS} at the inlet (Schlüter et al., 2004).

If the RANS models are to converge, some limited turbulence must be prescribed. The turbulence intensity is specified to $I = 0.5\%$ and the viscosity ratio ν_t/ν to unity, and this is based on research practice (Pereira et al., 2017) (Vaz et al., 2016). The turbulence intensity is defined as $I = u/U_0$, where u is the root-mean-square of the turbulent velocity fluctuations. I.e.,

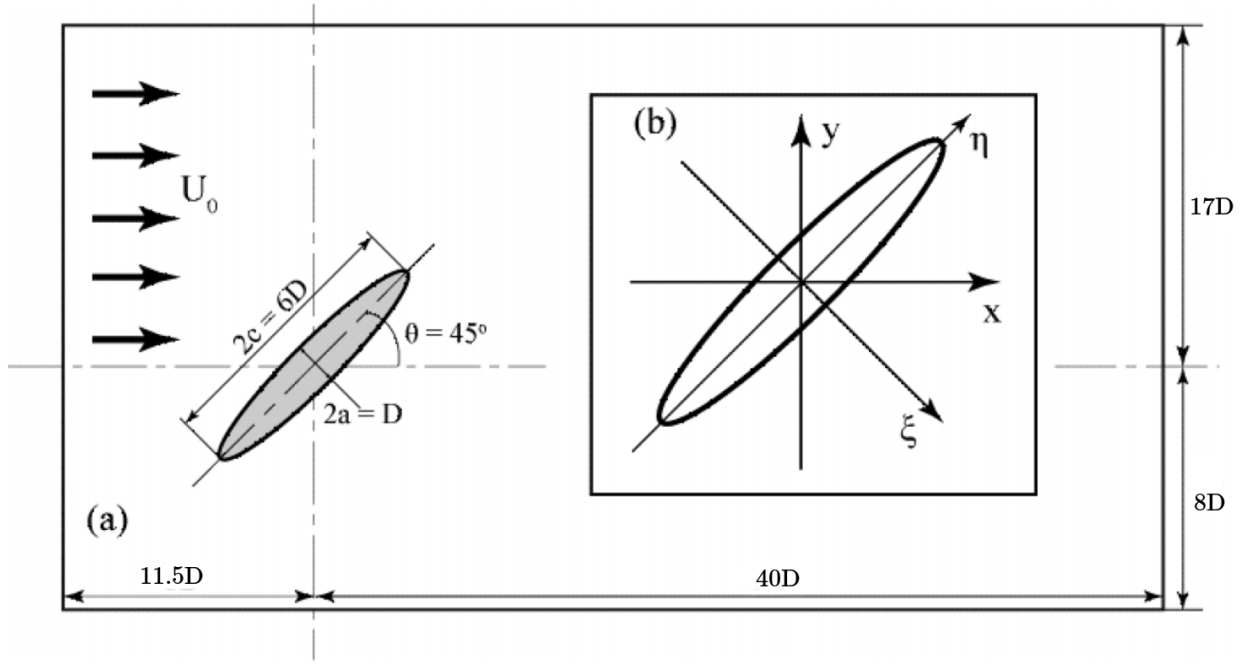

Figure 3.1: Domain topology at the meridionial plane (Jiang et al., 2015).

$$u = \sqrt{\frac{1}{3}(u_1^2 + u_2^2 + u_3^2)} = \sqrt{\frac{2}{3}k} \ . \tag{3.1}$$

Combining the definition of the turbulence intensity with Eq. (3.1), yields an expression for k given I and U_0

$$k = \frac{3}{2}(U_0 I)^2 \ . \tag{3.2}$$

Next, the viscosity ratio is used to derive the inlet ω-values. From the definition of ω, one have

$$\omega = \frac{k}{\nu_t} = \frac{k}{\nu_t}\frac{\nu}{\nu} = \frac{k}{\nu}(\frac{\nu_t}{\nu})^{-1} \ , \tag{3.3}$$

and the eddy viscosity is given as $\nu_t = k/\omega$.

For the $k-\omega$ $SSTLM$ model, the intermittency is set equal to 1 at the inlet, equaling laminar flow. Further, Re_θ at inlet is given by the expression

$$Re_{\theta t,inlet} = \begin{cases} 1173.51 - 589.428I + 0.2196I^{-2}, & I \leq 1.3 \ , \\ 331.50(I - 0.5658)^{-0.671}, & I > 1.3 \ , \end{cases} \tag{3.4}$$

where the turbulence intensity I is specified in terms of percentage (Rumsey, 2018).

Top, Bottom, Front, Back and Outlet Conditions

For all turbulence quantities and velocity components at the top, bottom, front, back and outlet boundaries, the zero gradient condition is applied. This correspond to the flow being assumed fully developed at each respective boundary in the direction of its normal vector (e.g. in the positive x-direction at the outlet boundary). The zero gradient condition is also applied to the pressure on the back, front, top and bottom boundaries, following the above argument. At the outlet, p is set equal to zero and this works as the reference pressure, which is strictly needed in incompressible flows, where pressure is only determined relative to some reference (Müller, 2017).

Wall Conditions

At the wall, the zero gradient condition is applied for the pressure (Versteeg and Malalasekera, 2007). As discussed in section 2.2, the mean turbulent boundary layer may either be resolved by integrating through the viscous sub-layer or by applying wall functions. Following the importance of transition in this flow and the poor transition modelling of the log-law (Eça et al., 2016), all RANS models are integrated down to the viscous sublayer. Thus, all models in this thesis are to satisfy the requirement of $y^+ < 1$. The corresponding wall modelling in OpenFOAM is presented in Table 3.1. A thorough description of the different wall models in OpenFOAM is given in Liu (2018). For the $k-\omega$ $SSTLM$ model, the zero gradient condition was applied to both γ and Re_{θ_t} (Langtry and Menter, 2009).

Table 3.1: Applied wall functions.

	OpenFOAM wall function
k	kLowReWallFunction
ω	omegaWallFunction
ν_t, ν_{SGS}	nutUSpaldingWallFunction

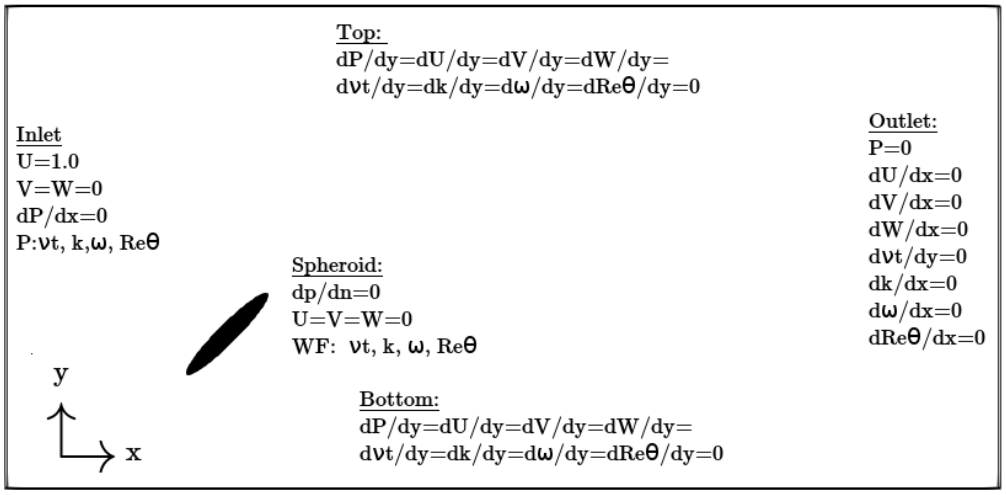

Figure 3.2: Boundary conditions in the x-y plane, WF: Wallfunction , P: Prescribed.

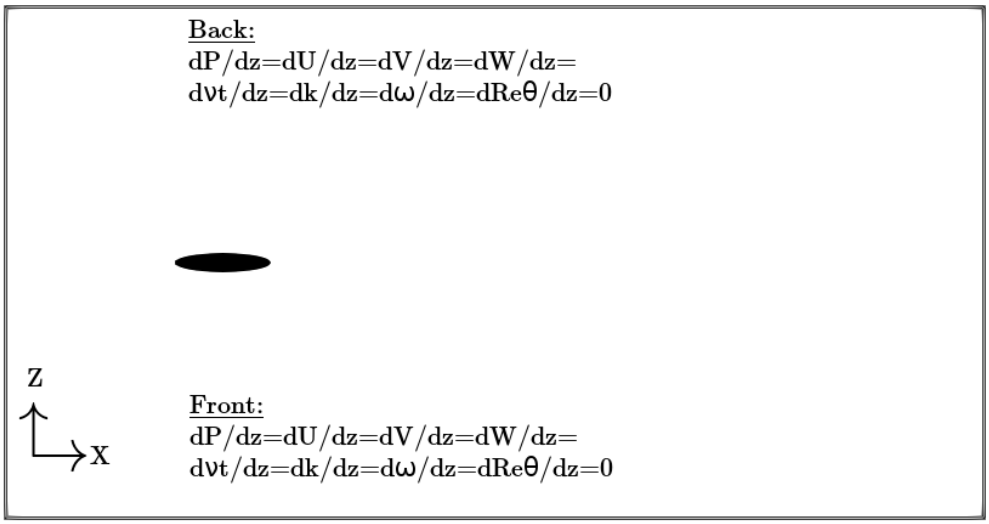

Figure 3.3: Boundary conditions in the x-z plane.

3.3 Grid Sets and Meshing Methodology

The meshing was performed in the OpenFOAM affiliated utilities blockMesh and snappyHexMesh. In blockMesh, the domain size and the number of cells at the coarsest refinement level are specified (Jackson, 2018). This mesh is a fully-structured hexahedral mesh. Next, snappyHexMesh is used to refine the mesh around solid objects and in other specified refinement regions. The solid objects are represented by CAD files (stl. or obj. format). Further, the user specifies a number of refinement levels and at each refinement level, the mesh density is scaled by a factor of 0.125, as cell sides are halved (0.5^3). In addition, close to solid objects, the user can specify the boundary layer mesh design in terms of cell thicknesses, refinement ratios and much more (Jackson, 2018). Lastly, the user specifies mesh quality control parameters. When snappyHexMesh is finished running, the mesh quality can be checked with the utility checkMesh.

All meshes passed the checkMesh utility with its default settings. I.e., critical mesh quality criteria such as max orthogonality, skewness and aspect ratio were all satisfied (Jackson, 2018). Further, the mesh design included two refinement regions, which were made to provide the necessary resolution in the wake of the spheroid. In Figure 3.4a, a slice of the mesh at $z = 0$, shows the topology of the two refinement regions in the meridional plane. Further, in Figures 3.4b and 3.4c, the boundary layer design is depicted.

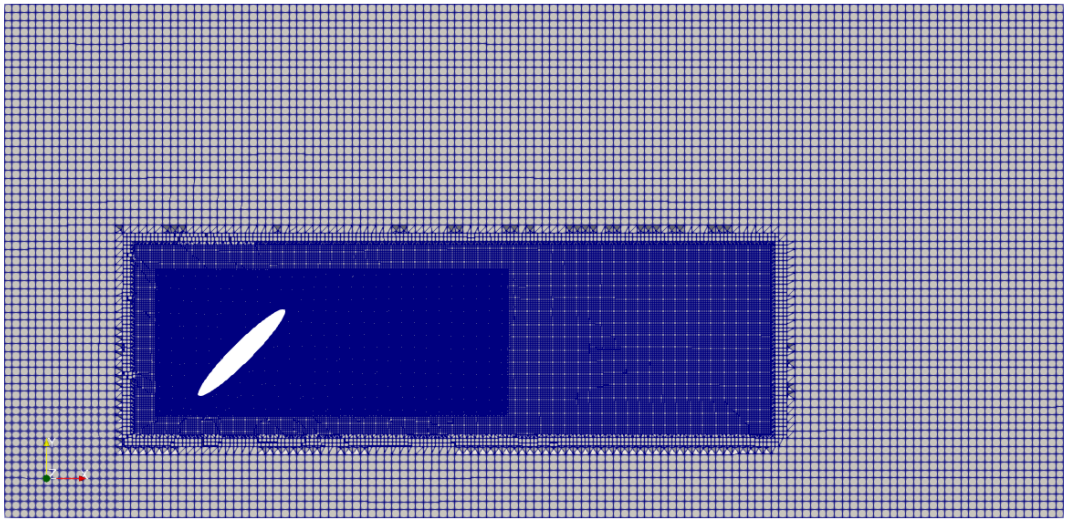

(a) Mesh topology at the meridional plane.

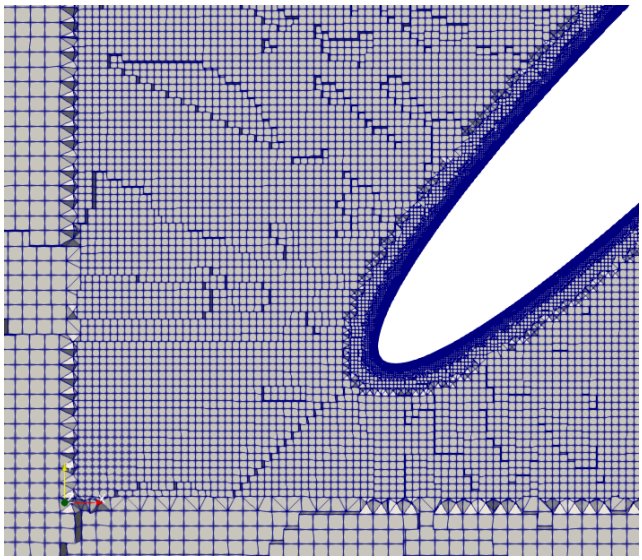

(b) Inner refinement box and boundary layer.

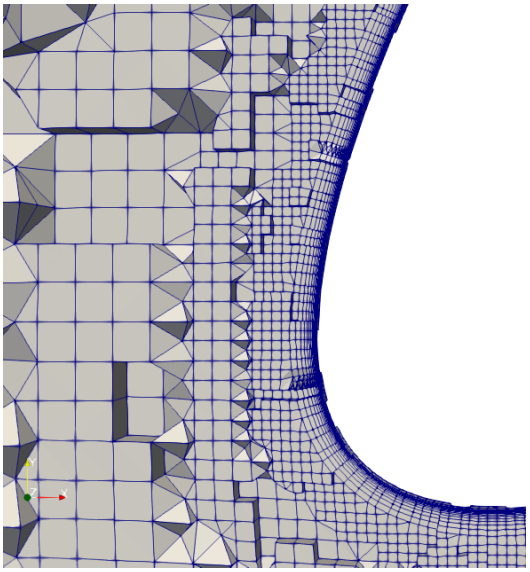

(c) boundary layer close-up.

Table 3.2: Mesh sizes, refinement factors and y^+_{max} for all grids.

	M1	M2	M3	M4
N_{target}	6M	9M	13.5M	20.25M
N_{actual}	6.1M	9.1M	14.0M	21.2M
r	-	1.14	1.15	1.15
y^+_{max}	0.625	0.475	0.305	0.250

To perform a V&V study, three requirements may be identified from section 2.5

1. All scales of the filtered flow must be resolved.
2. The mesh refinement needs to be consistent throughout the grid.
3. All meshes have to be in the asymptotic range.

The first requirement is mainly relevant for the coarsest mesh of a grid set assigned to some set of filtered equations (E.g. RANS or LES). To comply with this requirement, the meshing effort started at the boundary layer. As outlined in sections 2.2, for RANS and LES models, y^+ shall be kept below 1. However, y^+ depends on the flow, so this requirement makes an iterative procedure of meshing and simulation necessary. Using OpenFOAM's yPlus utility, the maximum y^+ was monitored and the grid was adjusted such that $y^+_{max} < 1.0$. The maximum value of y^+_{max} of all models for each grid is given in Table 3.2. Note, OpenFOAM has no utility for monitoring the LES requirements on x^+ or z^+, so this was unfortunately not monitored (cf. sections 2.2 and 4.5).

To investigate the rest of the grid, ParaView 5.4.1 was used to look for discontinuities in pressure fields. This would entail not smooth enough meshes, where consistency may be partly lost(Personal communication with Professor Bernhard Müller during a TEP4165 lecture at NTNU Trondheim in November 2017). This may slow or even prevent convergence in accordance to the Lax equivalence theorem (Lax and Richtmyer, 1956). After a smooth pressure field is ensured, the coarsest mesh is said to fulfill the above requirement: the coarsest mesh resolves all scales of the filtered flow. This is only regarded as a necessary condition and is far from sufficient in determining if the requirement is satisfied. I.e., qualitative differences may be observed at finer grids, indicating that the requirement do not hold. This is particularly relevant for hybrid and LES models, where appropriate wall-modelling and grid spacings are more challenging than in RANS.

After the coarsest mesh is developed, refined meshes must be developed in accordance to the second requirement. In snappyHexMesh, it is not possible to define a refinement ratio and apply it to an earlier defined grid. Hence, the refinement process is relatively cumbersome with the use of snappyHexMesh. To develop refined meshes, targets for the total number of grid cells N were set to cover a range of different mesh sizes suitable for RANS and LES calculations. Four meshes were developed, where the three coarsest meshes, M1, M2 and M3, were used for RANS, while the finer meshes, M2, M3 and M4, were used for hybrid simulations (lower number denotes coarser mesh). The refinement is specified in terms of a factor r^*, representing the relative increase in the total number of cells N. I.e, $N_{New} = r^* N_{Old}$. In this study $r^* \approx 1.5$; this was chosen as it ensures a refinement factor $r > 1.1$(cf. section 2.5), which is recommended in Roache (1998). In Table 3.2, the target and the achieved mesh sizes are presented
In order to perform a consistent refinement throughout the grid, some scaling factor was used to refine the initial base mesh in blockMesh and to adjust the thickness of the innermost cells in the boundary layer in snappyHexMesh. Thus, if one assumes that snappyHexMesh ensures a smooth internal mesh, the mesh specifications at the boundaries are assumed to ensure a mesh refinement consistent with the above refinement ratio. Thus, this procedure was used to develop M2-M4 in accordance with the target mesh sizes.

Compliance with the third requirement is discussed in length in section 3.5. Note, investigation of this requirement is performed by comparing the GCI of the coarse and medium grid to the GCI for the medium and fine grid.

3.4 Numerical Settings

The numerical schemes used in this thesis are inspired by Robertson et al. (2015). Here, three test cases of bluff body flows where utilized to determine effective schemes in terms of accuracy and speed. Recommendations were made for RANS and hybrid models. The notation used in the OpenFOAM documentation is adapted in this thesis (OpenCFD, 2018*e*).

$$\underbrace{\int_\Omega \frac{\partial \rho \boldsymbol{u}'}{\partial t}\, dV}_{time} + \underbrace{\int_{\partial\Omega} \rho \boldsymbol{u}'(\boldsymbol{u}' \cdot \boldsymbol{n})\, dA}_{divergence} = -\int_{\partial\Omega} p' \boldsymbol{n}\, dA + \underbrace{\int_{\partial\Omega} (\mu \nabla \boldsymbol{u}') \cdot \boldsymbol{n}\, dA}_{Laplacian} + \int_\Omega \rho \boldsymbol{f}'\, dV\ . \tag{3.5}$$

The schemes applied in this thesis are given in Table 3.3, and the corresponding OpenFOAM scripts are given in Appendix D. A thorough description of the different schemes are given in OpenCFD (2018*e*). First, the schemes applied in Robertson et al. (2015) were tested, but using 'leastSquares' for the gradient scheme proved to be unstable. Hence, the gradient scheme was set to the default option 'Gauss linear'. Further modifications were performed after discussions with Håkon Strandnes.

In addition to the above, Jasak (2018) proposed a set of best practice guidelines for OpenFOAM numerical schemes. Regarding 'divergence' schemes for Eq. (3.5) for hybrid and LES methods, it is noted that special care must be taken, and that upwind schemes are to be avoided because of their high numerical diffusivity. However, obtaining convergence for hybrid and LES models proved difficult. For hybrid methods, the same scheme as used in RANS had to be utilized, 'bounded Gauss linearUpwind', as less diffusive schemes were unstable. For LES, initially 'Gauss linear' was attempted, but this proved unstable. This scheme is unbounded, which may cause nonphysical high frequency oscillations(Versteeg and Malalasekera, 2007). A thorough discussion on properties of convection schemes, including the boundedness property, is given in Versteeg and Malalasekera (2007). To stabilize the solution, the scheme 'Gauss filteredLinear2' was utilized. In this scheme, limited amounts of upwind are added to limit the unboundedness of the regular 'Gauss linear'. The amount of limiting is set in terms of a constant k, where $k = 1$ amounts to fully limited, while $k = 0$ amounts to 'Gauss linear'. The minimum value of k where the simulation stayed stable, was found to be $k = 2.5\%$. Note, k is minimized to limit the numerical diffusivity.

Table 3.3: OpenFOAM Numerical Schemes.

	OpenFOAM Name
Time	CrankNicolson 0.9
Gradient	Gauss linear
Divergence U	bounded Gauss linearUpwind / Gauss filtreredLinear2 0.025 0.0
Divergence turbulence	bounded Gauss limitedLinear 1
Laplacian	Gauss linear corrected
Pressure-velocity coupling	PISO

Concerning temporal discretization, the time steps were set to achieve maximum Courant numbers of 0.8 ($\Delta t \sim 10^{-3}$). This may be considered as a conservative criteria for RANS-simulations, but was still pursued to ensure high temporal accuracy.

PISO was identififed as the most effective pressure-velocity coupling algorithm in Robertson et al. (2015), and was used in this thesis.

Regarding floating point arithmetics, double point precision is the default setting in OpenFOAMv5.0 and was used in all simulations.

Iterative errors in OpenFOAMv5.0 are controlled by use of the L_1-norm of the residual (cf. section 2.4). The undersigned has not found research underpinning the suitability of the L_1-norm as an estimator for the iterative error. The L_1-norm is a global measure similar to L_{RMS}, and following Eça and Hoekstra (2009) it is assumed to be an unsuitable criteria. However, in lack of other options, it is assumed that this criteria yields iterative errors negligible compared to the discretization errors. The default OpenFOAM tolerances were utilized (cf. Appendix D).

3.5 V&V Procedure

Following the material covered in sections 2.5, 3.3 and 3.4, both round-off and iterative errors may be assumed negligible to the discretization errors. Hence, the procedure outlined in ASME (2009) with the multivariate extension in Hills (2005) was utilized.

The parameter uncertainty has been neglected as the computational requirement was deemed prohibitive. Note, except WALE and Smagorinsky models, all turbulence models are subjected to parameter uncertainty in k and ω.

Asymptotic Range Assumption and DNS Uncertainty Estimate

To ensure that the simulations are in the asymptotic range, the following relation, which is valid in the asymptotic range (Roache, 1998), was monitored

$$GCI_{32} = r_{21}^{p} GCI_{21} \ . \tag{3.6}$$

This was done by monitoring the error in this assumption GCI_{Error}, which is defined as

$$GCI_{Error} \coloneqq \frac{GCI_{32}}{r_{21}^{p} GCI_{12}} - 1 \ , \qquad GCI_{32} = \frac{Fs}{r_{32}^{p} - 1} |\tilde{\epsilon_{32}}| \ . \tag{3.7}$$

To estimate the 95 % uncertainty interval of the DNS result, the study by Oliver et al. (2014) was utilized. Even though the flow case in this study vastly differs a channel flow, it was used in lack of more suitable references. In this study, the PDF of the relative error in the skin friction coefficient was established. In this case, 0.1 % is a conservative estimate of the numerical uncertainty (including discretization and sampling error). As the force coefficients are integrated variables similar to the skin friction coefficient, it is used as a reference PDF in this thesis. As the flow in this thesis is more complex, I assume the uncertainty to be somewhat larger, but in the same order of magnitude. Hence, I will use 0.5% as an estimate of the 95 % confidence interval for the relative numerical uncertainty for all force coefficients (corresponding to u_D in section 2.5).

Validation Metric Calculation

The Richardson extrapolated values and the numerical uncertainty of the verification points for a given model are estimated by use of Eqs. (2.53)-(2.55). Followingly, the comparison error vector $\boldsymbol{E}$ is assembled. As parameter uncertainty is neglected, V_{val} will be a diagonal matrix with entries at row and column i given as

$$V_{val_{ii}} = u_{num_i}^2 + u_{D_i}^2 \ , \tag{3.8}$$

where u_{num_i} and u_{D_i} are the numerical and DNS uncertainty for verification point i, respectively. Next, the verification metric r in Eq. (2.59) simplifies to the simple expression

$$r = \sqrt{\sum_{i=1}^{N} \frac{E_i^2}{u_{num_i}^2 + u_{D_i}^2}} \ , \tag{3.9}$$

where N is the total number of verification points. Finally, r/r_{ref} is calculated and interpreted according to section 2.5.

As the RANS, hybrid and WALE results were not in qualitative agreement with the DNS solution (cf. chapter 4), no other verification points than the force coefficients were utilized in the V&V procedure. If qualitative agreement had been achieved, more challenging verification points as for example time-averaged velocities at some location in the wake, could have been included.

3.6 Simulation Methodology and Post-Processing

All simulations aimed at obtaining statistical convergence, and this was monitored with the force coefficient time series. The force coefficients are defined as

$$CF_i = \frac{F_i}{\frac{1}{2}\rho U_0^2 \frac{\pi}{4} d^2}, \quad CM_i = \frac{M_i}{\frac{1}{2}\rho U_0^2 \frac{\pi}{4} d^3}, \quad i = x, y, z \ , \tag{3.10}$$

where d is the diameter of a volume-equivalent sphere, which for the 6:1 spheroid is $d = 1.817D$ (Jiang et al., 2015). As discussed in section 4, some of the simulations did not obtain statistical convergence and required to be analyzed at a given time instant which not necessarily is statistical representative of the model predictions.

The flow was post-processed using Paraview 5.4.1. This application provides powerful visualization possibilities for large data sets. In this thesis, the characterization of the wake topology of the different models has been of prime interest. Towards this end, λ_2 and $\boldsymbol{\omega}$ was investigated (cf. section 2.2). Applying OpenFOAM's post-processing utilities *lambda2* and *vorticity*, λ_2 and $\boldsymbol{\omega}$ were calculated and later visualized in Paraview. λ_2 was investigated in the form of iso-surfaces, whereas $\boldsymbol{\omega}$ was displayed in the form of 2D slices at various locations. Additionally, predictions of k and ν_{SGS} has been analyzed; production of these quantities indicates model prediction of laminar-turbulent transition. The selected post-processing quantities has been inspired by the earlier work on this flow configuration for lower Reynolds numbers (Jiang et al., 2014) (Jiang et al., 2015).

3.7 Computing Facilities

This research was supported in part with computational resources at NTNU provided by NOTUR, `http://www.sigma2.no`. The utilized Vilje HPC cluster has 1404 computing nodes, where each node has 2 Intel Xeon E5-2670 2.6 GHz 16-core CPUs and 32 GB RAM (NTNU-HPC-GROUP, 2018*a*). A HBA infiniband is used for inter-nodal communications. The number of nodes utilized was determined from a Vilje OpenFOAM performance study (NTNU-HPC-GROUP, 2018*b*), and ranged from 5 to 20 nodes.

Chapter 4

Results and Discussion

This chapter will present the results and discussion of the simulations. In sections 4.1-4.3, the results and discussion of the flows predicted by the, hybrid and LES models are given. Next, in section 4.4, the results of the V&V study are presented and discussed. Lastly, a discussion on the observed flow physics and suitable turbulence modelling is given in section 4.5. This section also includes a discussion on the methodology utilized in this study. I.e., shortfalls in the present thesis and proposals for improvements in pre-processing, V&V and post-processing in a future study. Further, force coefficient time series and statistics are given in Appendix A and B, respectively. Figures 4.1-4.2 give an overview of the wake topology for LES and hybrid models.

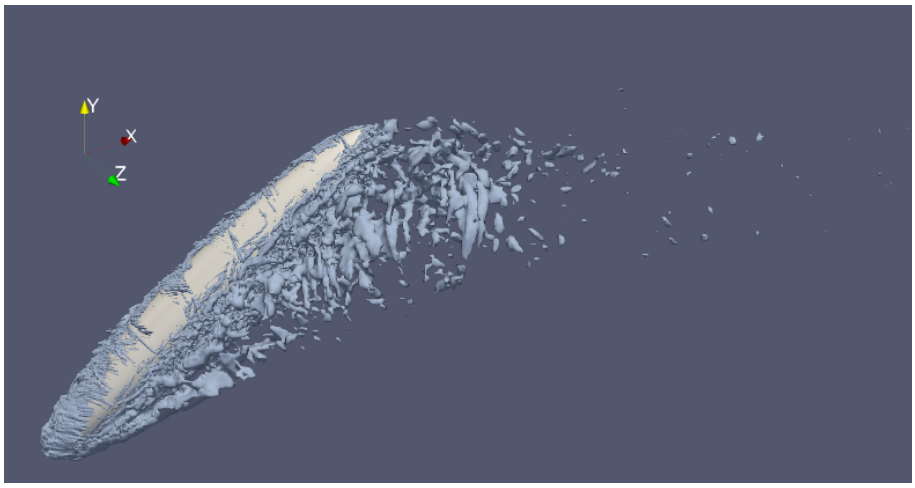

Figure 4.1: Smagorinsky. $\lambda_2 = -5$ - contours.

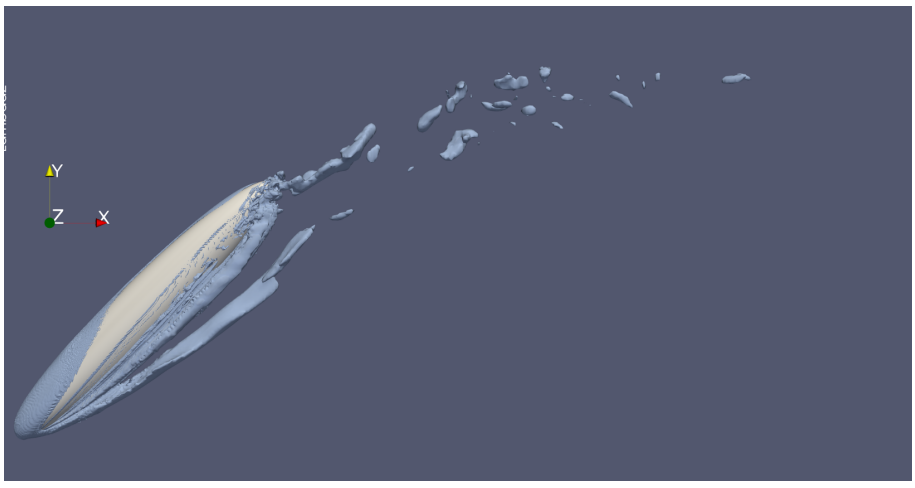

Figure 4.2: $k-\omega$ SST SAS. $\lambda_2 = -5$ - contours.

4.1 LES

For LES models, the results differ qualitatively with different grid spacings. For meshes M2 and M4, an oscillating wake was predicted (cf. Appendix A). At M3, WALE was unstable while Smagorinsky simulated an asymmetric wake. These qualitative differences violate the assumptions in ASME (2009), and thus a formal V&V study was not pursued. Instead, a less formal validation procedure was conducted, where the simulated force coefficients and characteristic features of the flow where compared to the DNS results (cf. section 2.2). This was pursued for the Smagorinsky model at mesh M3, as this result was in best qualitative accordance with the DNS results.

Results obtained at meshes M2 and M4 for both LES models used the 'Gauss linear' divergence scheme (cf. section 3.4). The solutions were stable, but predicted an oscillating wake (cf. Appendix A). The reasons thereof remain unclear. However, it is believed that mesh M2 might not be fine enough to satisfy the requirement of only modelling scales in the inertial-sub range (cf. section 2.1). The very fine aspect ratio in grid M4 (ratio between smallest and largest cell) is believed to be problematic, as this may cause loss of convergence (cf. section 2.2). I.e., by applying a smooth refinement (cf. section 3.3), the spheroid wall resolution becomes very fine (finer than the one applied in the DNS study). Additionally, the requirements on the near-body grid on x^+ and z^+ have not been ensured and may have a significant effect.

The reason for believing that there are issues with modelling and/or numerics in the simulations on meshes M2 and M4 follows the correctly predicted asymmetry in the simulation with Smagorinsky at mesh M3. After the initiation of the simulation, the wake starts to oscillate with an increasing amplitude. As the diffusivity is reduced, these oscillations increase in strength. When the diffusivity is low enough, the oscillation reaches a critical strength, where the wake remains on one side of the spheroid. This asymmetry is typically preserved for a period of 150 s. Figure 5.5a depicts the force coefficient time history when asymmetry was preserved. Due to no statistical convergence, an instantaneous flow field was investigated at $t = 279.1$ s.

Results

Figures 4.3-4.5 give an overview of the flow topology. Note, scaling issues with λ_2 make the comparison with the DNS results only qualitative in nature. That aside, the primary vortex pair can be seen in Figure 4.4 and 4.5. The scales of these structures are limited in comparison to the DNS results, as the wake-side vortex disintegrates at approximately $x = 0.15D$ and the opposing vortex at approximately $x = 0.8D$. In DNS, it was $x = 1.4D$ and $x = 3.2D$.

In Figure 4.6a, the vorticity of the primary vortex pair at $\bar{\xi} = -0.6$ is investigated. The wake-side and opposing vortex have strengths(maximum $\omega_x D/U_0$) of 39 %(yellow encircling) and 49 %(green encircling) relative to the DNS results. Moving in the positive η^*-direction, the primary vortex structures quickly disintegrate. This is clearly seen in Figure 4.6; the vortices at $\bar{\eta} = 0.6$ relative to at $\bar{\eta} = -0.6$ amounts to 23 % in the the wake side vortex and 19 % in the opposing vortex, respectively. In DNS, the strengths amounted to 127 % and 71 %.

This topology is convected to the intermediate wake, depicted in Figure 4.7. The maximum vorticity magnitudes in these slices are 15 % and 17 % of the DNS results at $x = 4D$ and $x = 8D$. However, there are groupings of vorticity, which are similar in topology to the DNS (cf. encirclings)

Thus, the Smagorinsky model predicts a flow which is similar to the DNS, but have weaker vortical structures which disintegrates more quickly. As the characteristic features of the flow are weaker in LES, so is the asymmetry of the flow. This can clearly be seen in the force coefficient statistics in Table 4.3b. Note the 21 % underprediction of the sideway force.

Further, where the DNS predicts small scale KH-instabilities on the pressure side of the spheroid, larger scale structures are predicted by the Smagorinsky model. Figure 4.8 shows a close-up of these structures. Their size, orientation and length to breadth ratios suggest they are separated shear layers, which have rolled up into vortical structures. As the mean flow is moving in the direction of the wake, flow separation occurs on the wake-side of the spheroid along its length. Based on section 2.2, the separation and following roll up of vortical structures is assumed to follow from a combination of separation, curvature and crossflow induced instabilities.

Table 4.1: Smagorinsky force coefficients statistics and comparison errors.

	CF_X	CF_Y	CF_Z
Average	0.816	-0.856	0.522
RMS	0.816	0.856	0.532
E_{avg}	0.026	-0.026	-0.138
E_{RMS}	0.016	0.016	-0.138

The distribution of ν_{SGS} in the $x-y$ plane and the $\eta-z$ plane is given in Figures 4.9 and 4.10. Figure 4.10 indicates that separation induced instabilities are triggered at the lower pole, whereas natural and separation induced transition occur at the spheroids upper pole (there are high velocities at this point)(cf. section 2.2). The lower pole production suggests that the asymmetry of the flow is already felt at this point. Next, Figure 4.9 indicates that separation induced instabilities are triggered at the upper pole. The production of ν_{SGS} occurring at $\eta \sim -0.5$, is assumed to follow from wake instabilities, produced by interactions between the primary vortex pair and smaller scale structures.

Discussion

The deviations to DNS in coherence and strength of the primary vortex pair may be attributed to various sources. It is difficult to determine a separation location exactly as the λ_2 contours do not provide a decisive location. However, Figures 4.4 and 4.5 suggest that separation occur at an earlier location than seen in the DNS results, and this suggests a weaker vortex pair. It is believed that the deviation in the prediction of the primary vortex pair has substantial ramifications for the rest of the flow field. This may be related to additional viscosity introduced through modelling and numerical schemes. I.e., the simulation introduces numerical diffusivity $\nu_{numerical}$ through the 'Gauss filteredLinear2'-divergence scheme, yielding a too high effective viscosity, $\nu_{effective} = \nu + \nu_{SGS} + \nu_{numerical}$ (cf. section 3.4). Here, the Smagorinsky model incorrectly produces ν_{SGS} in wall-bounded laminar flows, and hence increases $\nu_{effective}$ further. It is believed that this increased effective viscosity results in a weaker primary vortex pair, as the mechanism causing this pair is affected.

When comparing Figures 2.11 and 4.3, there is a clear difference in the structures on the spheroid's suction side. It is believed that the Smagorinsky model is unable to predict the smaller scale KH-instabilities seen for DNS, because of its inability to model wall-bounded laminar flows properly. A possible resolution of this issue is the application of the WALE model. However, good enough grid resolution at the spheroid wall might be equally important (cf. section 3.3). The aforementioned issues might be as important in the modelling of the spheroid's suction side. E.g. Figure 4.9 displays the production of ν_{SGS} in the vicinity of the primary vortex pair. Here, SGS modelling and grid resolution are essential in predicting the disintegration of the primary vortex pair accurately.

In essence, it remains substantial further work to finish the V&V-study of LES-models for this flow configuration. However, it should be noted that the Smagorinsky model do predict the flow asymmetry, and this suggests that LES-models are able to capture the global instability of the flow (cf. section 2.2). More efforts with pre-processing are assumed to improve the predictions substantially. I.e., the boundedness issue with mesh M3 could possibly be resolved with a higher quality grid. Towards that end, LES mesh practices should be followed in terms of x^+, z^+ and smoothness (cf. section 4.5). Followingly, the 'Gauss linear' scheme could be utilized, eliminating the numerical viscosity of the solution. In addition WALE might be stable with this improved grid, and with its superior modelling of wall-bounded laminar flows, the results might improve. The sum of these efforts would reduce the effective viscosity and is assumed to provide a primary vortex pair more in accordance with DNS, and a stronger asymmetry.

.

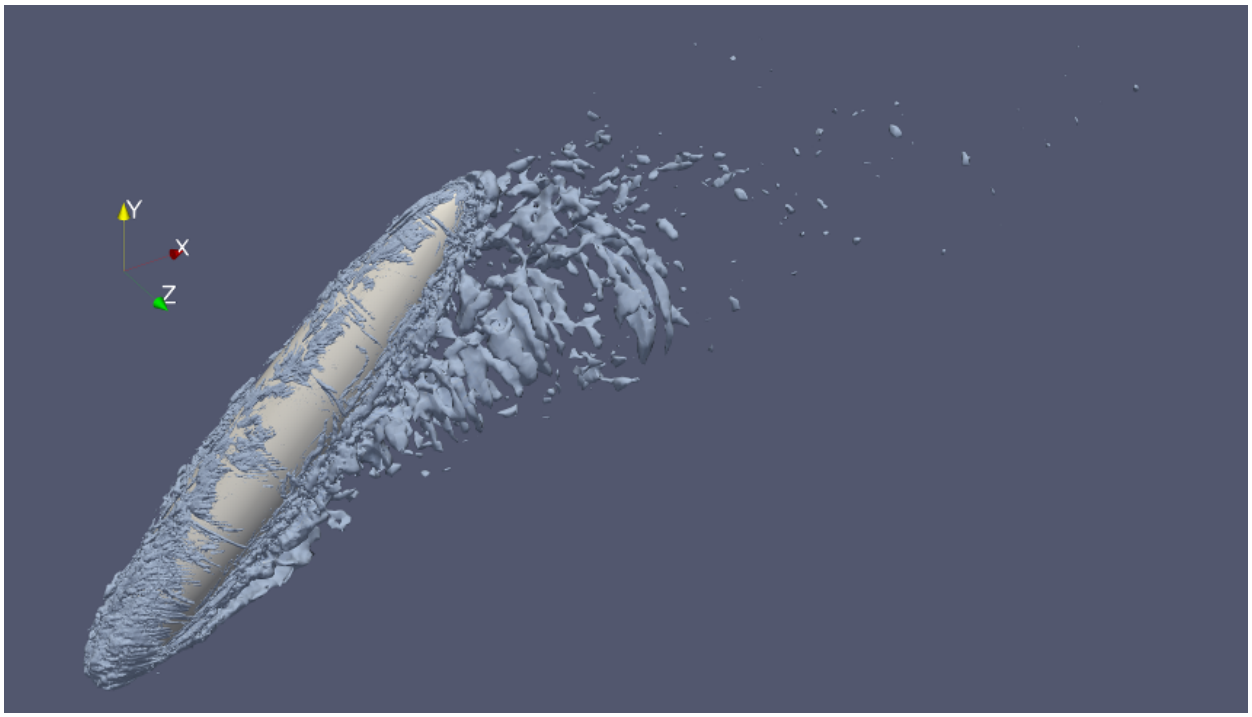

Figure 4.3: Smagorinsky. $\lambda_2 = -5$ - contours. Overall topology.

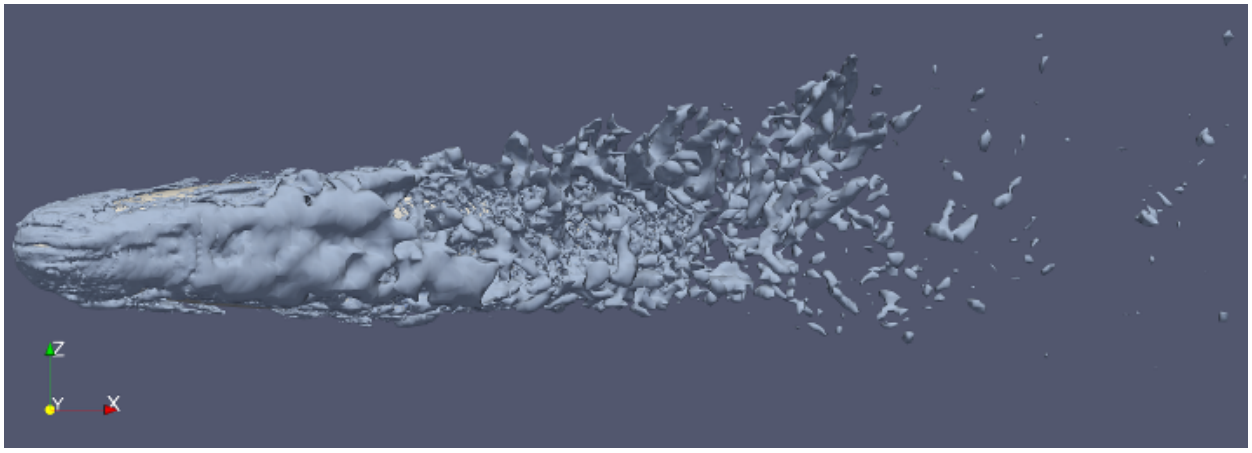

Figure 4.4: Smagorinsky. $\lambda_2 = -5$ - contours. Bottom view.

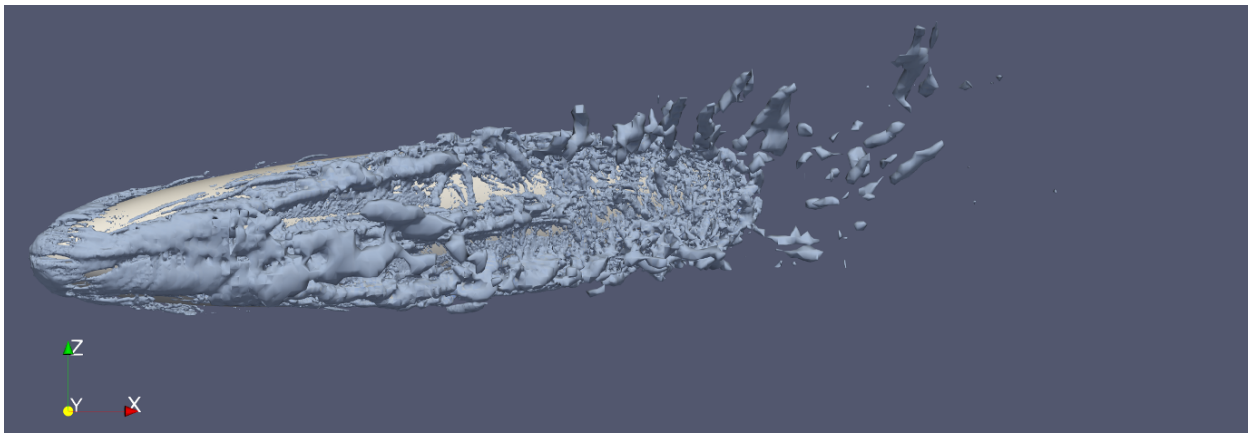

Figure 4.5: Smagorinsky. $\lambda_2 = -10$ - contours. Bottom view.

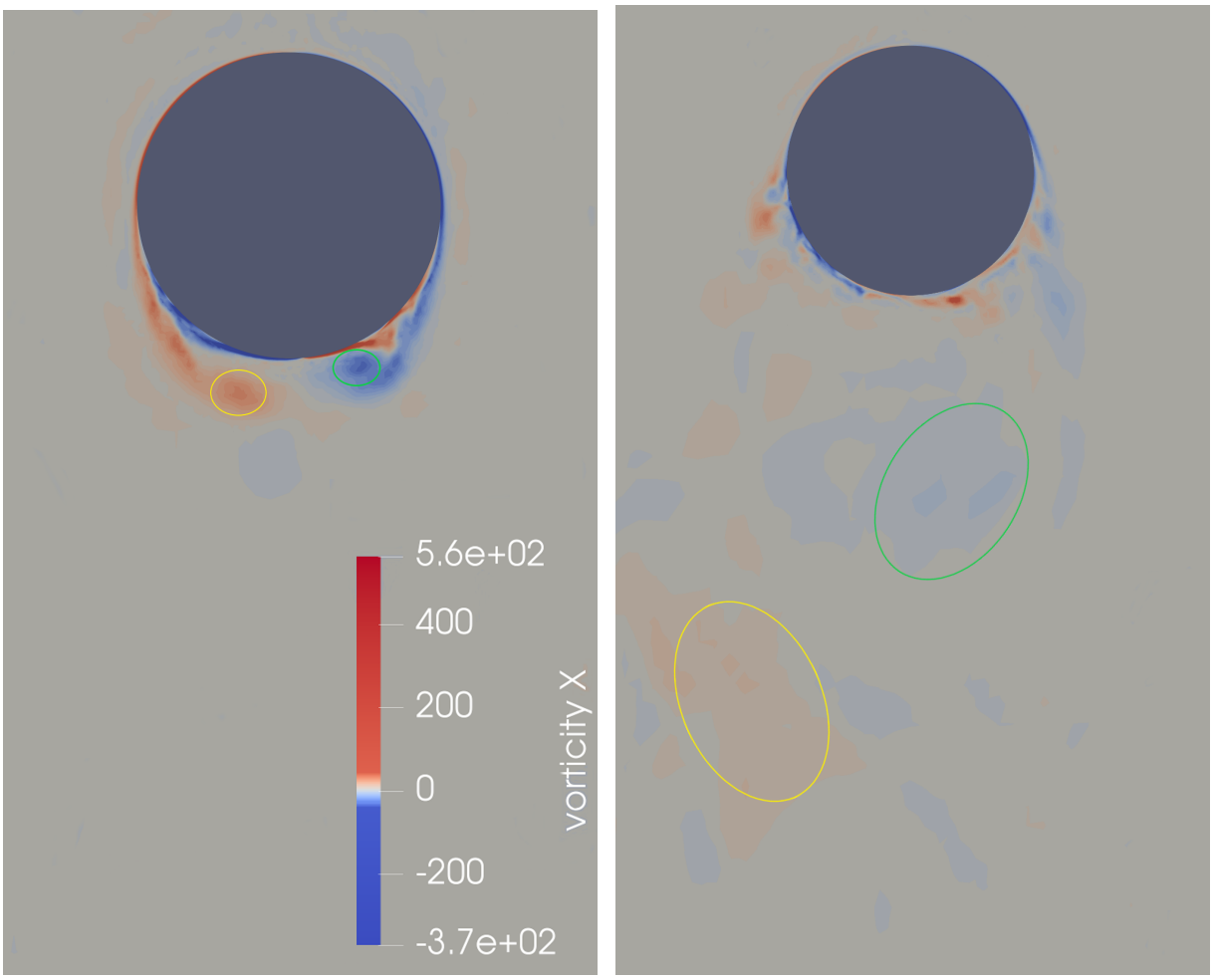

(a) $\bar{\eta} = -0.6$. (b) $\bar{\eta} = 0.6$.

Figure 4.6: Smagorinsky. $\omega_x D/U_0$ in the $\xi - z$ plane. Facing negative η-direction

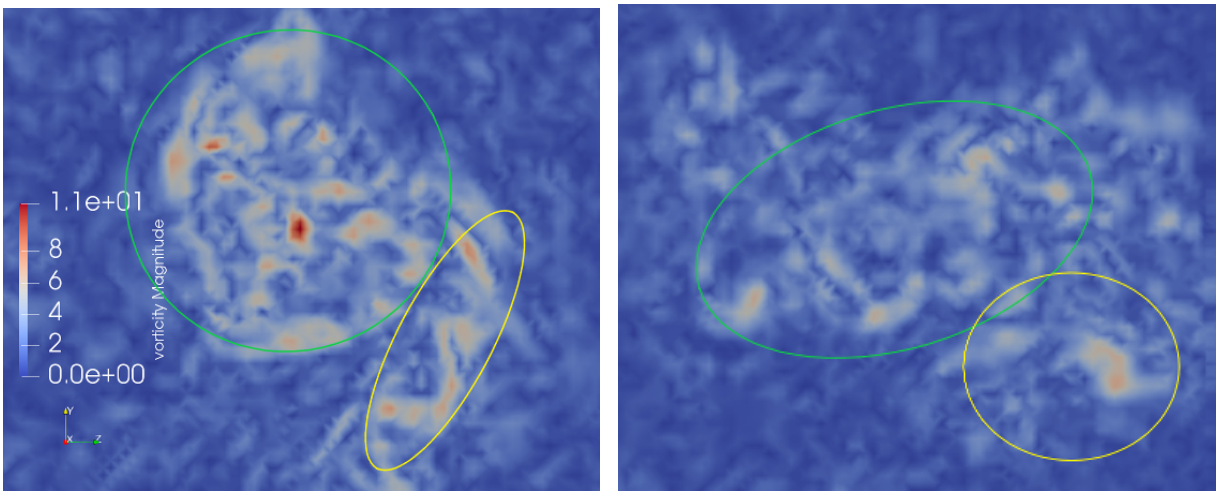

(a) $x = 4D$. (b) $x = 8D$.

Figure 4.7: Smagorinsky. $\sqrt{\omega_i \omega_i} D/U_0$ in the $y - z$ plane. Facing positive x-direction.

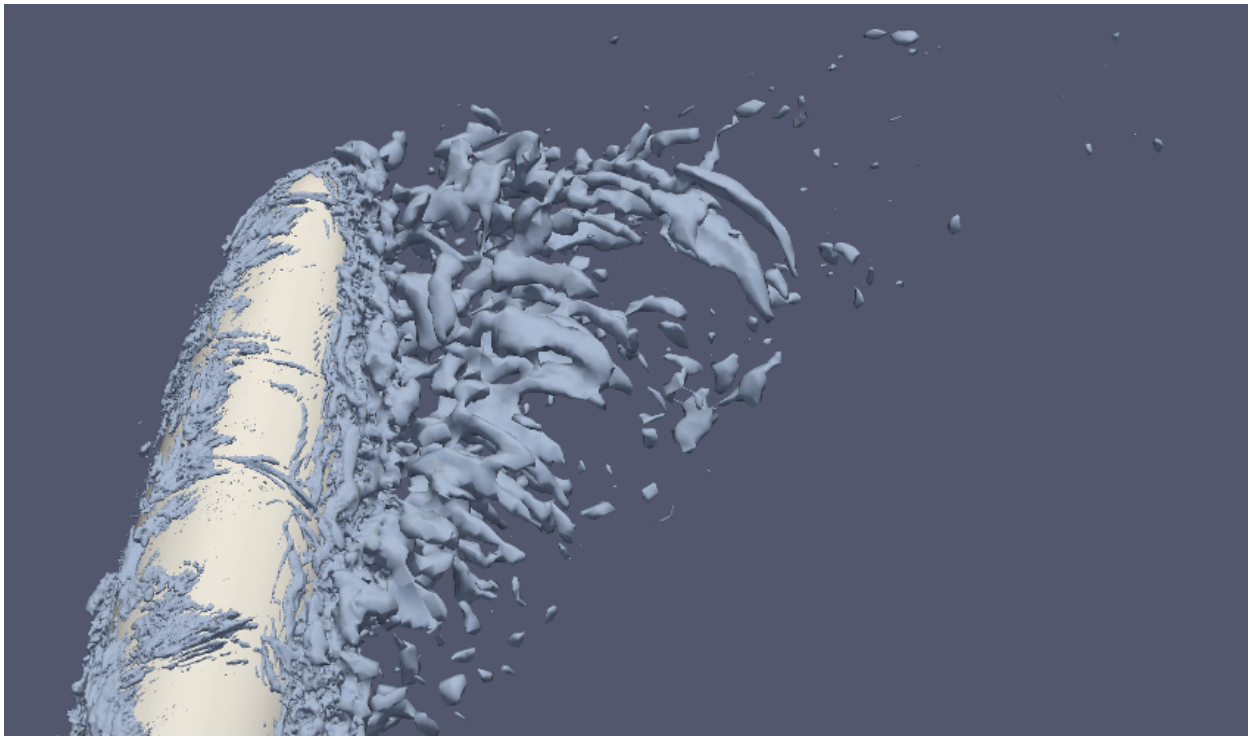

Figure 4.8: Smagorinsky. $\lambda_2 = -5$. Structures at the upper pole.

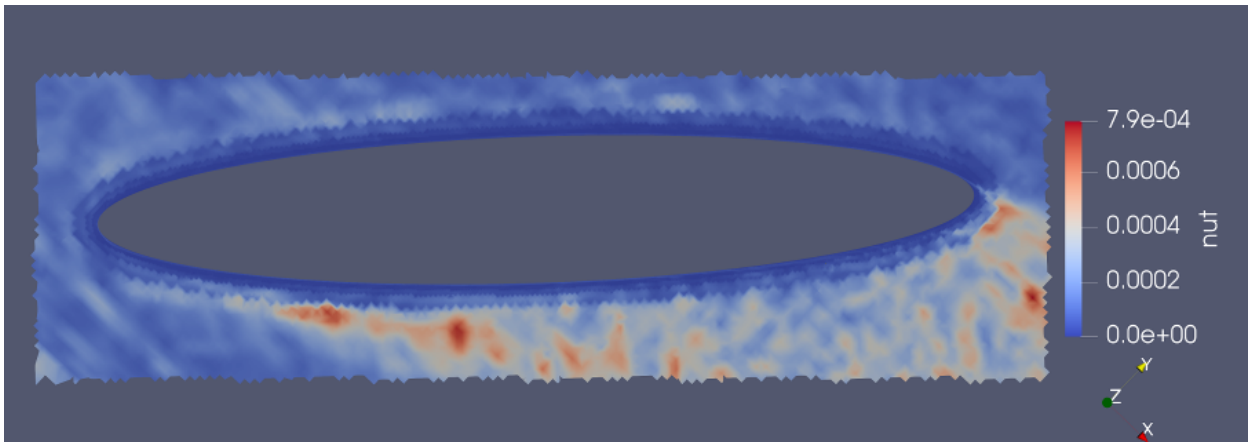

Figure 4.9: Smagorinksy. SGS viscosity ν_{SGS} in the meridional plane.

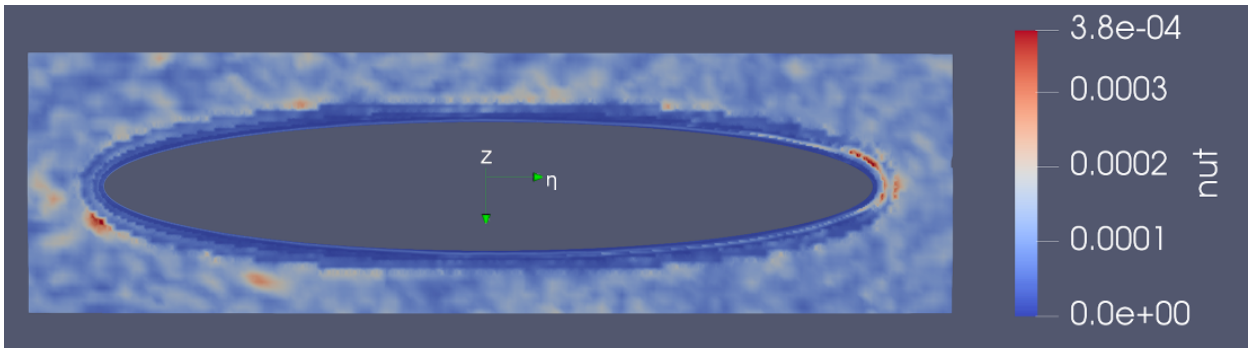

Figure 4.10: Smagorinksy. SGS viscosity ν_{SGS} in the $\eta - z$ - plane at $\xi = 0$.

4.2 Hybrid

The hybrid models is assumed to have qualitative grid independence, and was used in a formal V&V study, applying ASME (2009). Hence, only the results from grid M3 is discussed. Before discussing the results, please note section 3.4 concerning the convection scheme utilized for hybrid models. Initially, the unbounded 'Gauss linear' scheme was used, but it proved to yield unstable calculations which exceeded the floating point precision after approximately 80 time steps. This amounts to the same problem as seen with LES. The preliminary results showed an oscillating wake qualitatively similar to the LES results for grids M2 and M4 (cf. Appendix A). To obtain a stable result and force statistics, the same scheme as applied in RANS was utilized. Without doubt, this have had a significant effect on the result, as it introduces substantial numerical diffusivity that effectively damped the oscillations. Additionally, $k-\omega\ SST\ SAS$ predicts a significant increase in force coefficients from grid M3 to M4. This suggests that the assumption of qualitative grid independence might be questionable and this is further discussed in section 4.5. The Richardson extrapolated force coefficient statistics and time series are reported in Table 4.2 and Appendix A.

Results

The hybrid models predict symmetry about the meridionial plane (cf. Figures 4.11-4.13). In having qualitative similar near body flows, the two models also predict similar body forces. I.e., steady forces in x- and y-directions and only small wiggles around a zero mean force in the z-direction (cf. Table 4.2).

The predicted flow topology is similar to that seen in Figure 4.20, depicting the $k-\omega\ SST$ topology; a primary vortex pair, a secondary counter-rotating pair and small scale structures separating at the spheroid's sides (encirclings in Figure 4.11 identifies these features as done in Figure 4.20). This topology is discussed in detail in the next section. The smaller scale structures originating at the spheorid's upper pole is highlighted in Figure 4.15.

The strength(maximum $\omega_x D/U_0$) of the primary vortex pair in the near body wake is investigated in Figure 4.14. $k-\omega\ SST\ SAS$ and $k-\omega\ SST\ DES$ at $\bar{\eta}=-0.6$ predict a symmetric pair with strengths of 36.9 % and 60.0 % of the mean DNS value, respectively. The vortex pair are completely symmetric for both models. The difference in strength between these two models subsides with increasing $\eta*$, and the vorticity dynamics are very similar at $\bar{\eta}=0.6$, 14.3 % $\pm$ 0.5 % of the DNS mean value.

The further downstream development of these structures are presented in Figure 4.16. At $x=2.5D$, the vortex structures are still symmetric and the primary vortices are distinguishable. However, for $x \gtrsim 5.5D$, the wake is unstable as it becomes asymmetric and ruptures into numerous minor structures. These structures gradually dissipates and have maximum magnitudes($\sqrt{\omega_i\omega_i}D/U_0$) of 2.3 % ($k-\omega\ SST\ SAS$) and 3.0 % ($k-\omega\ SST\ DES$) at $x=39D$ compared to at $x=2.5D$.

Regarding production of turbulent kinetic energy, Figure 4.17 displays significant variations in the production of k for $k-\omega\ SST$, $k-\omega\ SST\ SAS$ and $k-\omega\ SST\ DES$. At the lower pole, $k-\omega\ SST\ SAS$ predicts transition, which, based on the position, is assumed to be separation induced (cf. section 2.2). This is not seen for $k-\omega\ SST$ and $k-\omega\ SST\ DES$. Note, the only difference in the turbulence model formulations between $k-\omega\ SST$ and $k-\omega\ SST\ SAS$ is the second source term in the ω equation, Q_{SAS} (cf. Eq. (2.33)). Hence, this term is assumed to be active at the lower pole. Due to the similarity between $k-\omega\ SST$ and $k-\omega\ SST\ DES$, it is assumed that $k-\omega\ SST\ DES$ is in RANS mode at the entire spheroid surface. The same trend is seen at the upper pole; $k-\omega\ SST$ and $k-\omega\ SST\ DES$ yield the same predictions, whereas $k-\omega\ SST\ SAS$ predicts substantially higher production. For all models, the dominant source of k near the body is separation induced transition at the spheroid upper pole. Finally, Figure 4.18 displays k in the meridional plane for the two hybrid models. It is apparent that $k-\omega\ SST\ SAS$ does not predict further production in the wake, whereas $k-\omega\ SST\ DES$ does. The maximum levels of k for $k-\omega\ SST\ DES$ is at approximately $x \sim 11D$.

Table 4.2: Hybrid models force coefficients statistics and comparison errors.

(a) $k-\omega$ *SST SAS* .

	CF_X	CF_Y	CF_Z
Average	0.734	-0.829	0.007
RMS	0.734	0.829	0.089
E_{avg}	-0.066	0.001	-0.586
E_{RMS}	-0.066	-0.011	-0.581

(b) $k-\omega$ *SST DES* .

	CF_X	CF_Y	CF_Z
Average	0.754	-0.878	0.002
RMS	0.754	0.878	0.003
E_{avg}	-0.036	-0.048	-0.658
E_{RMS}	-0.046	0.038	-0.667

Discussion

Concerning the primary vortex pair, it is clear that both hybrid models underpredict its strength. Following the above discussion, $k-\omega$ *SST SAS* is assumed to be in its SRS mode at the lower pole, and its transition prediction causes an inaccurate modelling at the lower pole. The additional source term of the ω-equation (cf. section 2.2) do not yield improvements over the conventional $k-\omega$ *SST* model, as its prediction of the primary vortex pair is closer to the DNS result in terms of strength. The unsteadiness caused by the separation induced instabilities at the upper pole is believed to trigger the SRS mode of $k-\omega$ *SST SAS*.

Regarding $k-\omega$ *SST DES*, it is believed that this model is in RANS mode at the lower pole, given the similar RANS distributions of k. This combined with the inaccurate prediction of the primary vortex pair indicate that smaller scales and unsteadiness are of importance at the lower pole (features not captured in RANS mode). In the vicinity of the upper pole, it is believed that $k-\omega$ *SST DES* acts in its SRS mode because of the observed smaller scale structures. Additionally, the force coefficients deviate to those seen for $k-\omega$ *SST*, implying that the model is in its SRS mode close to the spheroid.

The detached eddies at the upper pole are assumed to cause both hybrid models to be in their SRS mode in the wake. This causes production of anisotropic turbulence. These structures make the wake slightly asymmetric at $x = 2.5D$, and eventually destabilize the primary vortex configuration downstream ($x = 5-6D$). It is assumed that this unsteadiness are stronger with lower numerical diffusivity and ultimately trigger the wake oscillations. The present simulations, however, are similar to that seen in Jiang et al. (2014) for $Re = 1000$, where the symmetric wake turns unstable at $4-5D$. This suggests that the RANS filtering and numerical schemes damps out instabilities and effectively solve a lower Reynolds number problem. Note, the turbulence in the immediate vicinity of the upper pole, given the above assumptions, are isotropic following the isotropic RANS modelling.

As further discussed in section 4.5, a clear determination of the turbulent length scale would be highly useful in assessing this result. With a clear distinction of the different modelling regions (RANS or SRS), the discussion of the effect of the different regions would be more accurate.

The hybrid models do not qualitatively reproduce the flow (this is determined formally in section 4.4). In order to improve the predictions, the most critical aspect is the numerical schemes. Similarly to the LES simulations, the unboundedness of the 'Gauss linear' divergence scheme yields unstable solutions, whereas upwind schemes add too much numerical diffusivity. Following additional efforts into pre-processing, the problem with unboundedness might be resolved. However, the results with 'Gauss linear', prior to instability, displayed a highly oscillating wake. In removing the numerical diffusivity, more unsteadiness is observed, and correspondingly a larger portion of the domain is assumed to be resolved in SRS mode. Nevertheless, regions of isotropic RANS modelling may inaccurately model the near-body flow and this may have significant ramifications for the wake. The early results with an oscillating wake is a testament thereof; the simulations with anisotropic modelling, LES, show stronger oscillations than seen for RANS. Hence, the isotropic near-wall modelling might be deteriorating in obtaining qualitative resemblance with the DNS results.

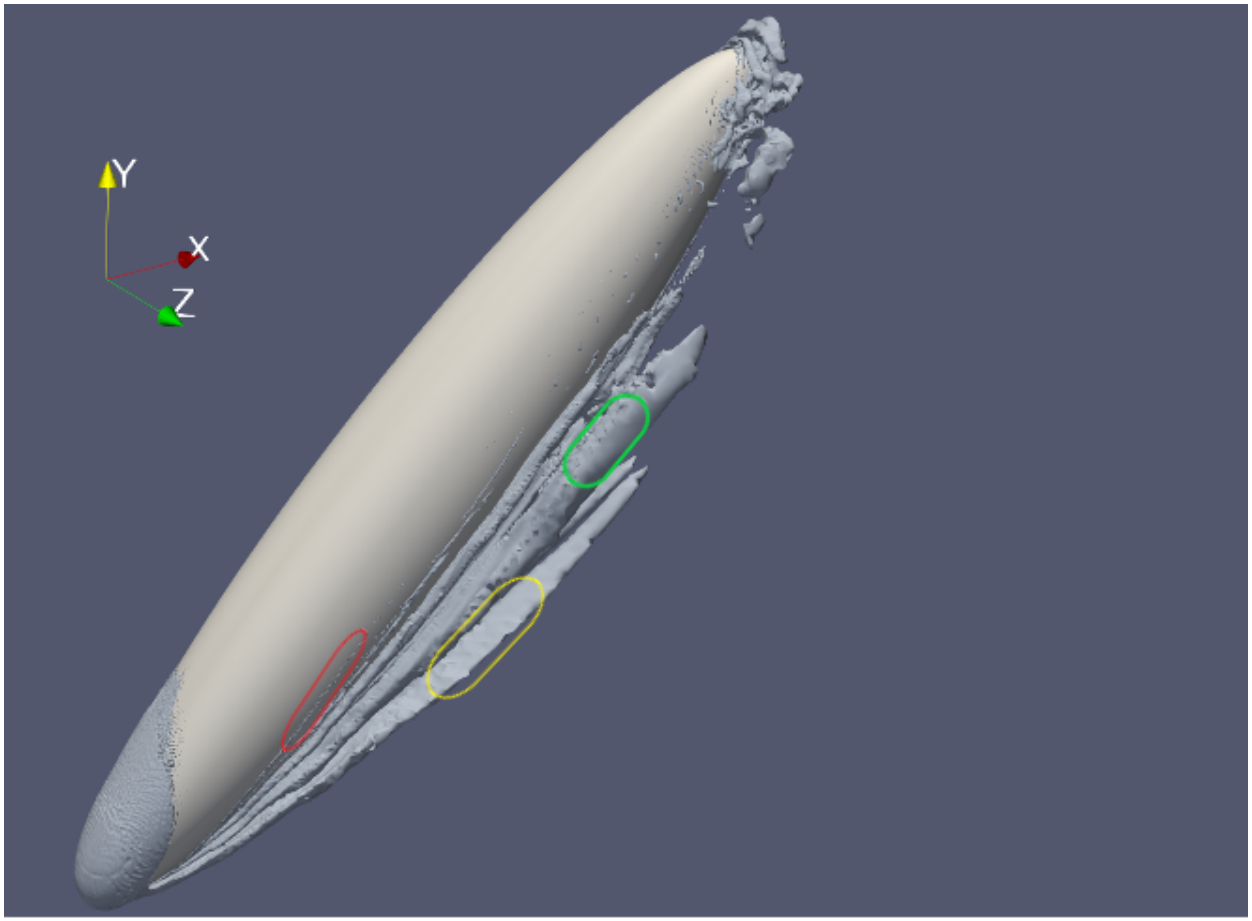

Figure 4.11: $k-\omega$ *SST DES*. $\lambda_2 = -10$ - contours. Overall topology.

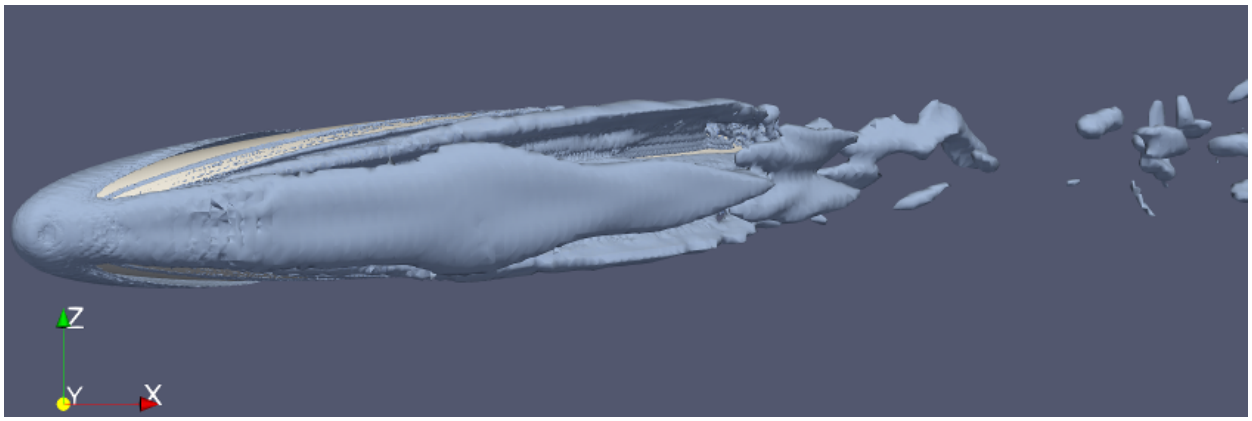

Figure 4.12: $k-\omega$ *SST SAS*. $\lambda_2 = -5$ - contours. Bottom view of primary vortex pair.

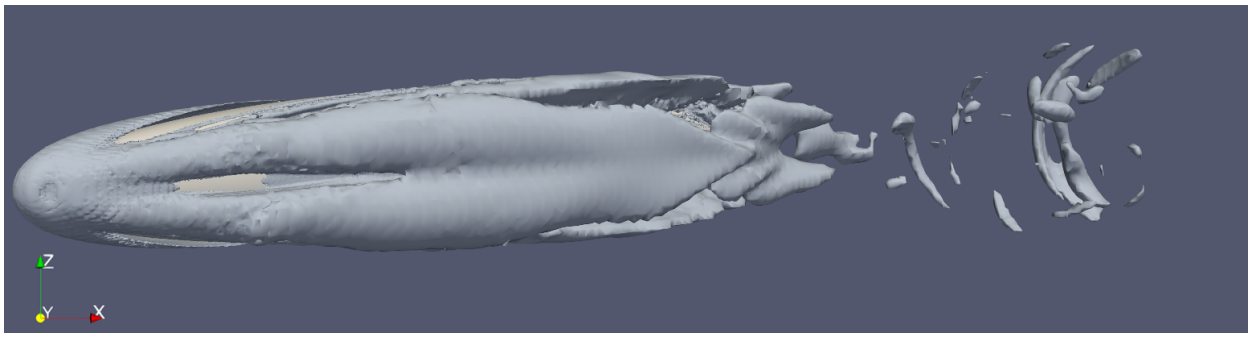

Figure 4.13: $k-\omega$ *SST DES*. $\lambda_2 = -5$ - contours. Bottom view of primary vortex pair.

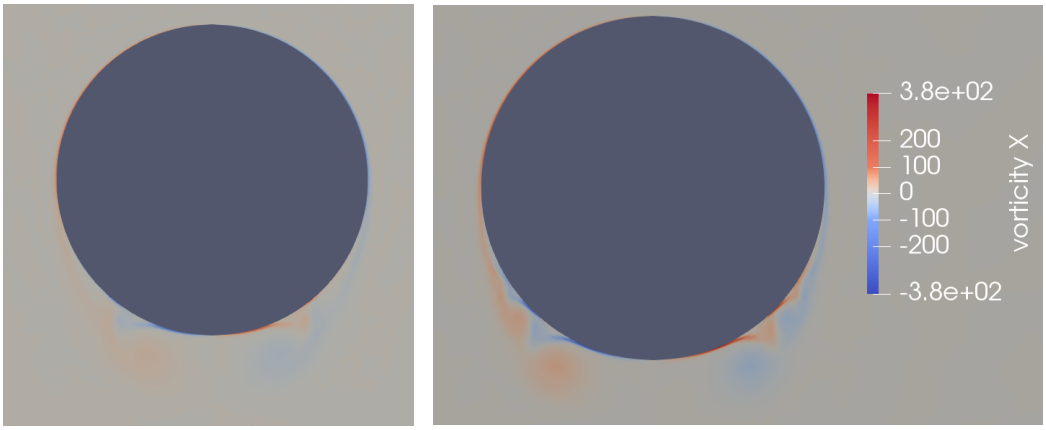

(a) $k-\omega$ *SST SAS* . $\eta = -0.6$.

(b) $k-\omega$ *SST DES* . $\eta = -0.6$.

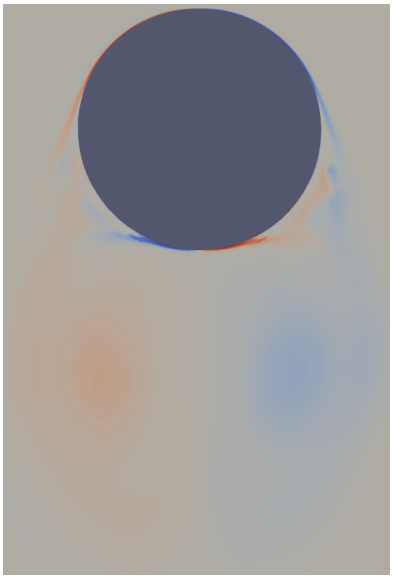

(c) $k-\omega$ *SST SAS* . $\eta = 0.6$.

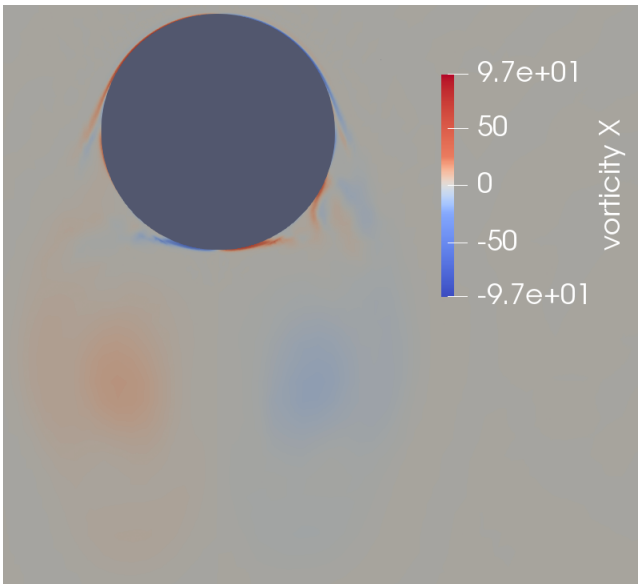

(d) $k-\omega$ *SST DES* . $\eta = 0.6$.

Figure 4.14: Hybrid models. $\omega_x D/U_0$ in the $\xi - z$ plane. Facing negative η-direction. Vertically aligned figures share color map.

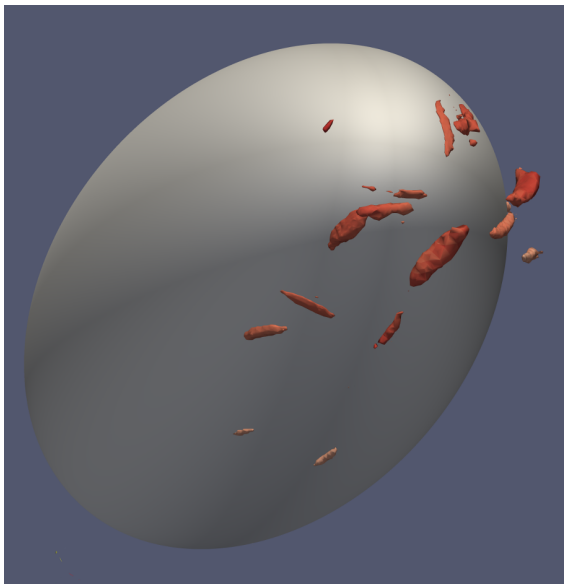

(a) $k-\omega$ *SST SAS* .

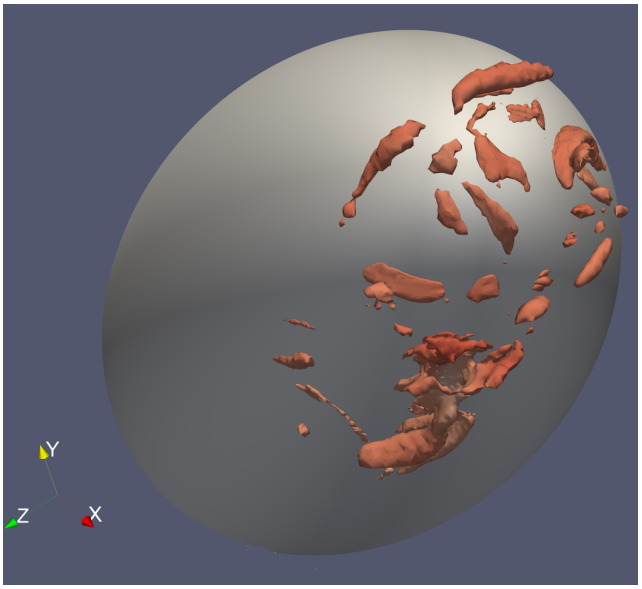

(b) $k-\omega$ *SST DES* .

Figure 4.15: Hybrid models. $\lambda_2 = 150$ - contours. Structures at the upper pole.

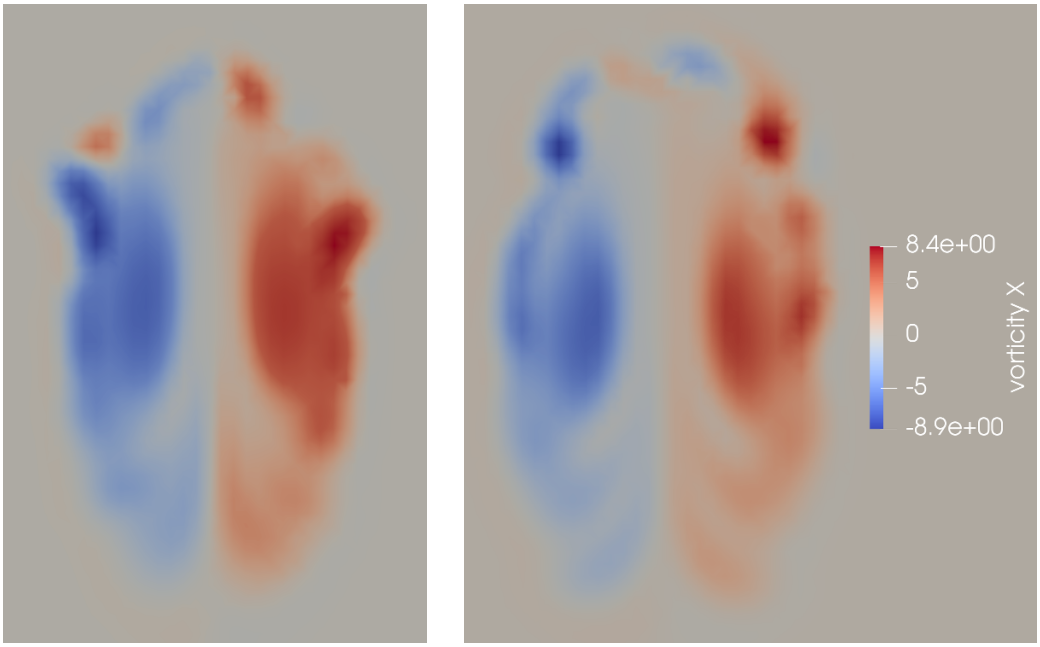

(a) $k-\omega$ *SST SAS* . $x = 2.5D$.

(b) $k-\omega$ *SST DES* . $x = 2.5D$.

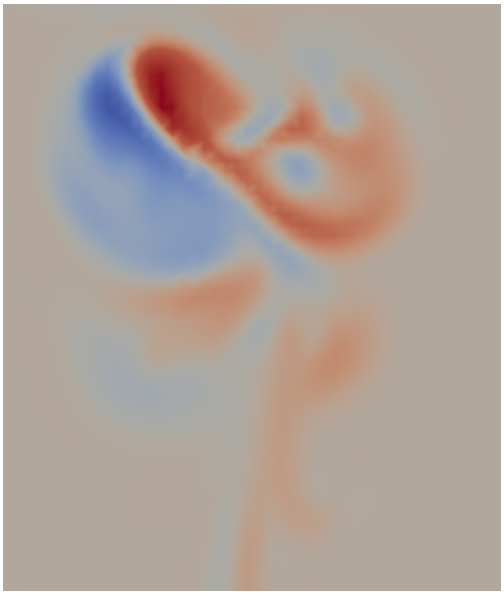

(c) $k-\omega$ *SST SAS* . $x = 6D$.

(d) $k-\omega$ *SST DES* . $x = 6D$.

(e) $k-\omega$ *SST SAS* . $x = 10D$.

(f) $k-\omega$ *SST DES* . $x = 10D$.

Figure 4.16: Hybrid models. $\omega_x D/U_0$ in the $y-z$ plane. Facing positive x-direction.

(a) $k-\omega$ SST .

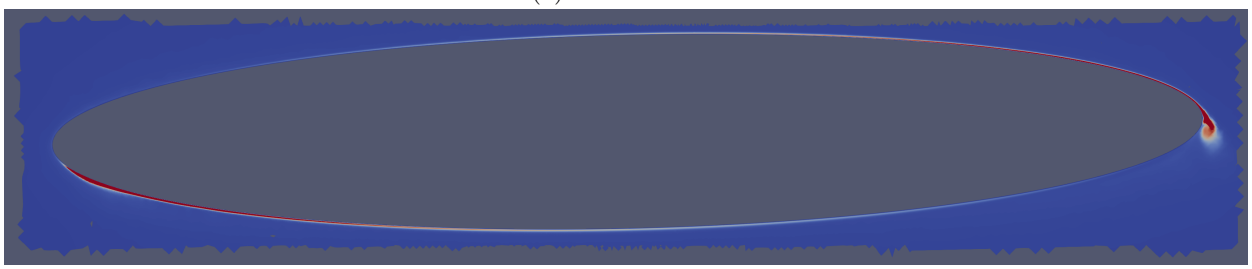

(b) $k-\omega$ SST SAS .

(c) $k-\omega$ SST DES .

Figure 4.17: Hybrid models. Predictions of near-body turbulent kinetic energy.

(a) $k-\omega$ SST SAS .

(b) $k-\omega$ SST DES .

Figure 4.18: Hybrid models. Predictions of turbulent kinetic energy in the meridional plane.

Table 4.3: RANS models force coefficient statistics and comparison errors.

(a) $k-\omega$ SST .

	CF_X	CF_Y	CF_Z
Average	0.760	-0.872	0.005
RMS	0.760	0.872	0.006
E_{avg}	-0.030	-0.042	-0.655
E_{RMS}	-0.040	0.032	-0.664

(b) $k-\omega$ $SSTLM$.

	CF_X	CF_Y	CF_Z
Average	0.757	-0.870	0.000
RMS	0.757	0.870	0.001
E_{avg}	-0.033	-0.040	-0.660
E_{RMS}	-0.043	0.030	-0.669

4.3 RANS

The RANS results are qualitatively similar for grids M1, M2 and M3. Thus, the assumption that all scales are appropriately resolved for a given model is assumed satisfied for the two RANS models(cf. section 3.3). Hence, a formal V&V study was pursued and this is reported in section 4.4. In the following, grid M2 was used to analyze the flow. Cf. Table 4.3 for Richardson extrapolated force coefficient statistics and Appendix A for time series. As seen in the statistics and figures, the two models predict a highly similar flow. Thus, when appropriate, only the predictions of $k-\omega$ SST are presented.

Results

The RANS models predict symmetry about the meridionial plane (cf. Figures 4.20-4.22). The two models essentially predict the same force coefficient time histories; steady forces in x and y -directions and small oscillations around a zero mean force in the z-direction.

The near-body topology, which is common for both models, is displayed in Figures 4.20-4.23 and have the following main features. The yellow encircling in Figure 4.20 identifies the primary vortex pair, which originates close to the spheroid lower pole. This pair is symmetric. Further, the green encircling identifies the secondary vortex pair, counter-rotating relative to the primary pair. This is most clearly depicted in Figure 4.23a. The red encircling highlights small scale structures, separating along the spheroid's spanwise direction. Figure 4.23 indicates that these structures act as a vorticity source to the primary vortex pair. However, towards the upper pole, the supply of vorticity is limited, as the primary vortex pair is convected downstream. Separation occurs at the spheroid upper pole, and this is depicted by strong λ_2-contours in Figure 4.19.

Concerning the strength(maximum $\omega_x D/U_0$) of the primary vortex pair, at $\bar{\eta} = -0.6$ and at $\bar{\eta} = 0.6$ it amounts to 44.6 % and 13.8 % of the mean DNS values (cf. Figure 4.23). These value are identical for both models to within 0.01 %.

The wake downstream development is depicted in Figure 4.24. At $x = 2.5D$, the wake is close to symmetric, but small structures, mainly from separation at the upper pole, are also present. The configuration becomes slightly unstable in the interval $x \in (4D, 10D)$, but the primary vortex pair stays intact. At $x = 12D$, the configuration retains stability and gradually dissipates downstream.

Regarding production of turbulent kinetic energy, the two models yield similar predictions at the lower pole: no separation induced transition (cf. Figure 4.25). At the spheroid's downstream facing side (suction side), it is predicted increased levels of k with increasing η^*. This is assumed to follow from natural transition; as the flow around the spheroid have similarities with the flow around a 2D airfoil, there is an increased velocity at the spheroids suction side. With increased velocities, high velocity gradients cause production of turbulent kinetic energy (cf. Eq. (2.30)). This corresponds to the model approximation of natural transition. $k-\omega$ $SSTLM$ do predict slightly higher production than $k-\omega$ SST, but the models predict values in the same order of magnitude. Moving to the spheroid's upper pole, both models predict separation induced transition. However, $k-\omega$ $SSTLM$ do this is in a far greater degree than $k-\omega$ SST (approximately a factor of 20 in difference). At $x \sim 10D$, both models predict substantial production of k (cf. Figure 4.26). $k-\omega$ $SSTLM$ yields the highest levels of k, but the the predictions are of the same order of magnitude.

Discussion

The two RANS models underpredict the strength and downstream development of the primary vortex pair. Hence, important physical mechanisms of the flow are not captured, and this is assumed to be related to general isotropic RANS characteristics. I.e., isotropic turbulence modelling and the damping of smaller temporal and spatial scales.

The one big difference between the predictions of the two RANS models is the amount of separation induced transition at the upper pole. $k-\omega$ $SSTLM$'s 'separation correction' is active and yields higher predictions of k than those seen for $k-\omega$ SST. As crossflow instabilities are of big importance in this flow, the inclusion of a $k-\omega$ $SSTLM$ model with such a correction would have been interesting (cf. (Watanabe et al., 2009)). From Figure 4.26, it is apparent that wake instabilities cause significant production of k for both models. Given the similar values of k in the wake for the two models, the same development of the primary vortex pair is observed; diffusion eventually stabilizes the topology, which maintains the integrity of the primary vortex pair. Followingly, the improved transition modelling of $k-\omega$ $SSTLM$ over $k-\omega$ SST do not have a significant effect in providing improved qualitative resemblance with DNS.

As aforementioned, it is believed that fundamental features of RANS filtering are attributable to the qualitatively wrong results (cf. section 4.4 for the formal assessment). Firstly, RANS filters out smaller scale temporal and spatial scales (Menter and Egorov, 2010), and this is believed to dampen out wake instabilities, and consequently the wake asymmetry. Secondly, isotropic modelling of the near body flow is assumed to be inaccurate (cf. section 2.2). In order to confirm this suspicion, generation of Reynolds stresses from the DNS results would have been revealing (cf. section 4.5). In essence, the results are indicative of RANS modelling being unsuitable for this flow configuration. However, the issue of anisotropic turbulence could be addressed with EARSM or Reynolds stress models. The problem with damping of the wake instabilities, however, is a fundamental characteristic of RANS, making RANS modelling unsuitable in this region.

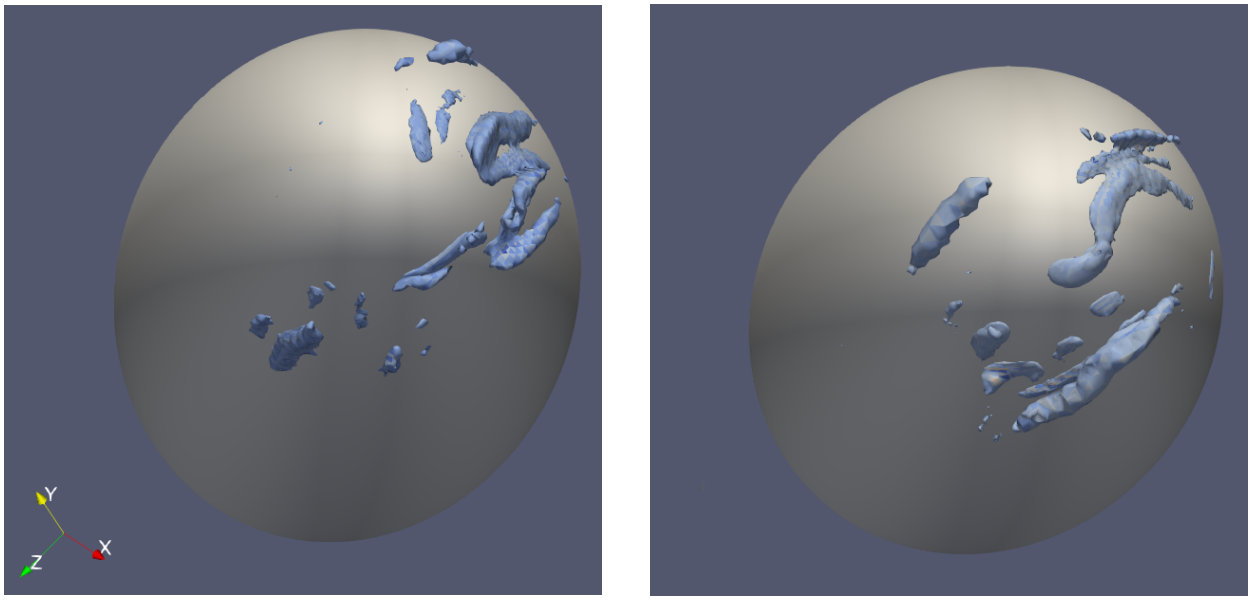

(a) $k-\omega$ SST . (b) $k-\omega$ $SSTLM$.

Figure 4.19: RANS models. $\lambda_2 = 150$ - contours. Structures at the upper pole.

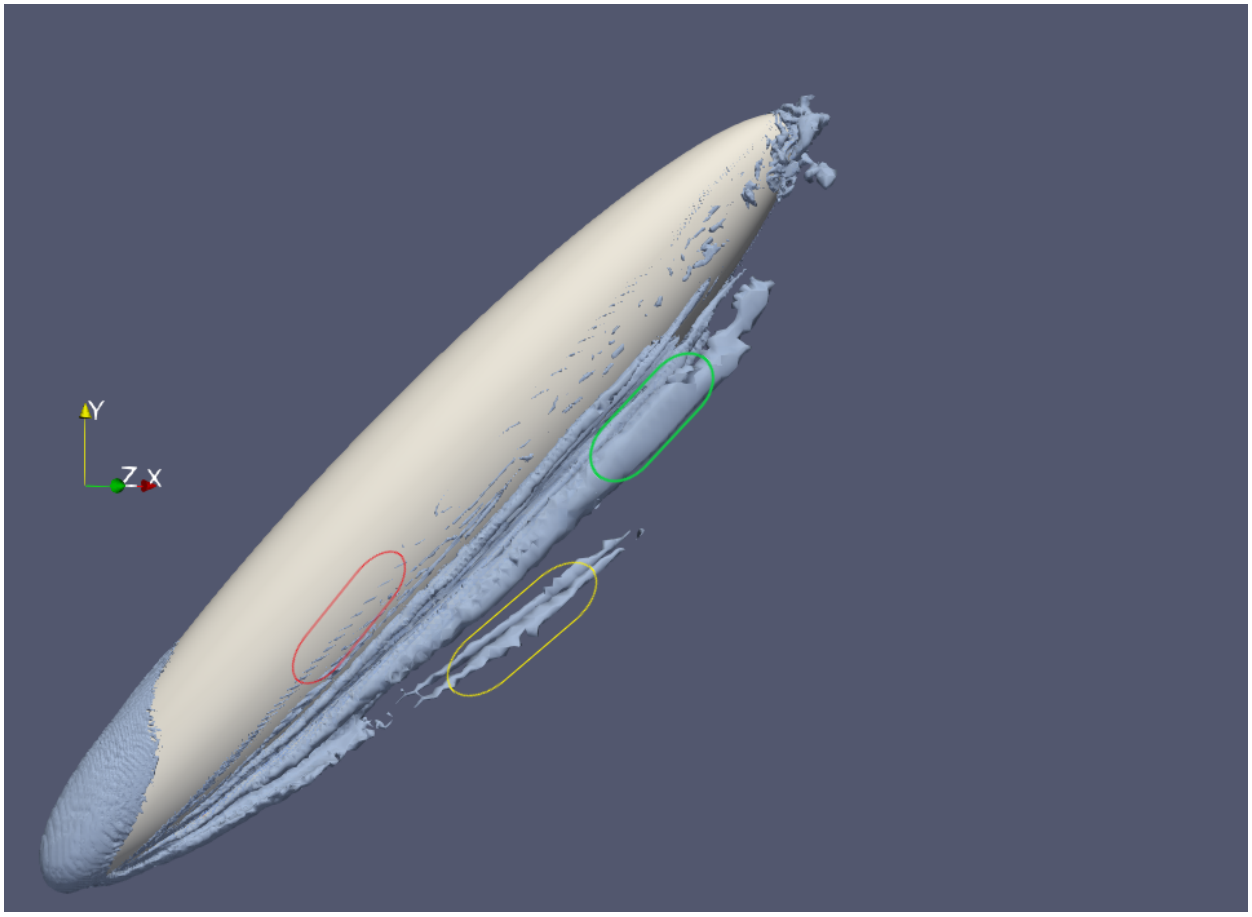

Figure 4.20: $k-\omega$ SST . $\lambda_2 = -10$ - contours. Overall topology.

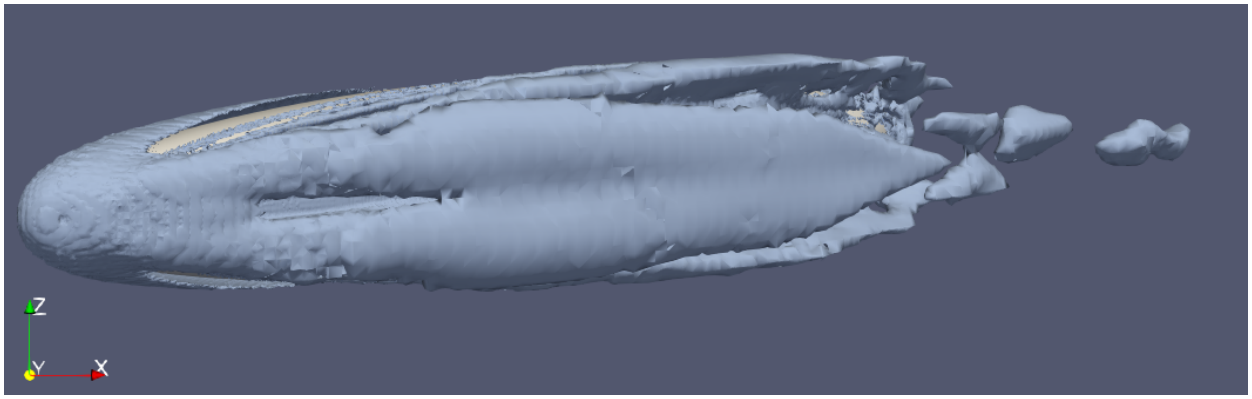

Figure 4.21: $k-\omega$ SST . $\lambda_2 = -5$ - contours. Bottom view of primary vortex pair.

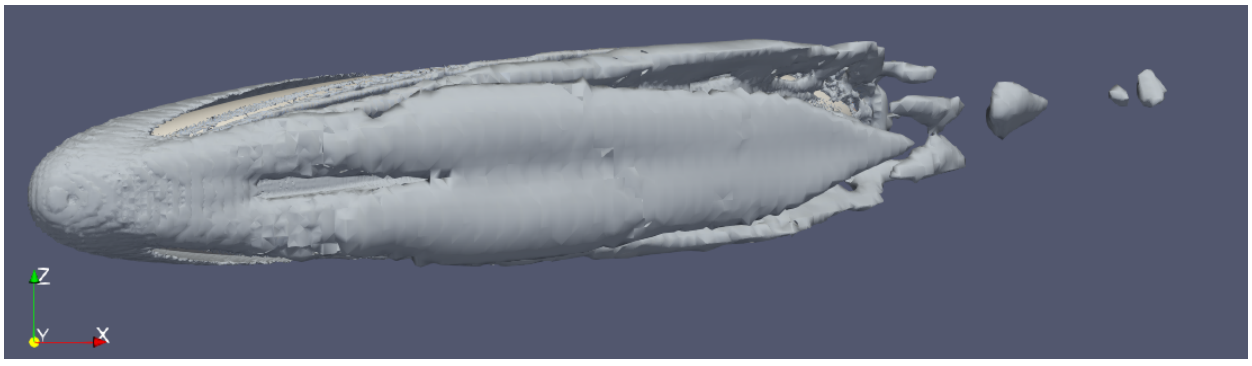

Figure 4.22: $k-\omega$ $SSTLM$. $\lambda_2 = -5$ - contours. Bottom view of primary vortex pair.

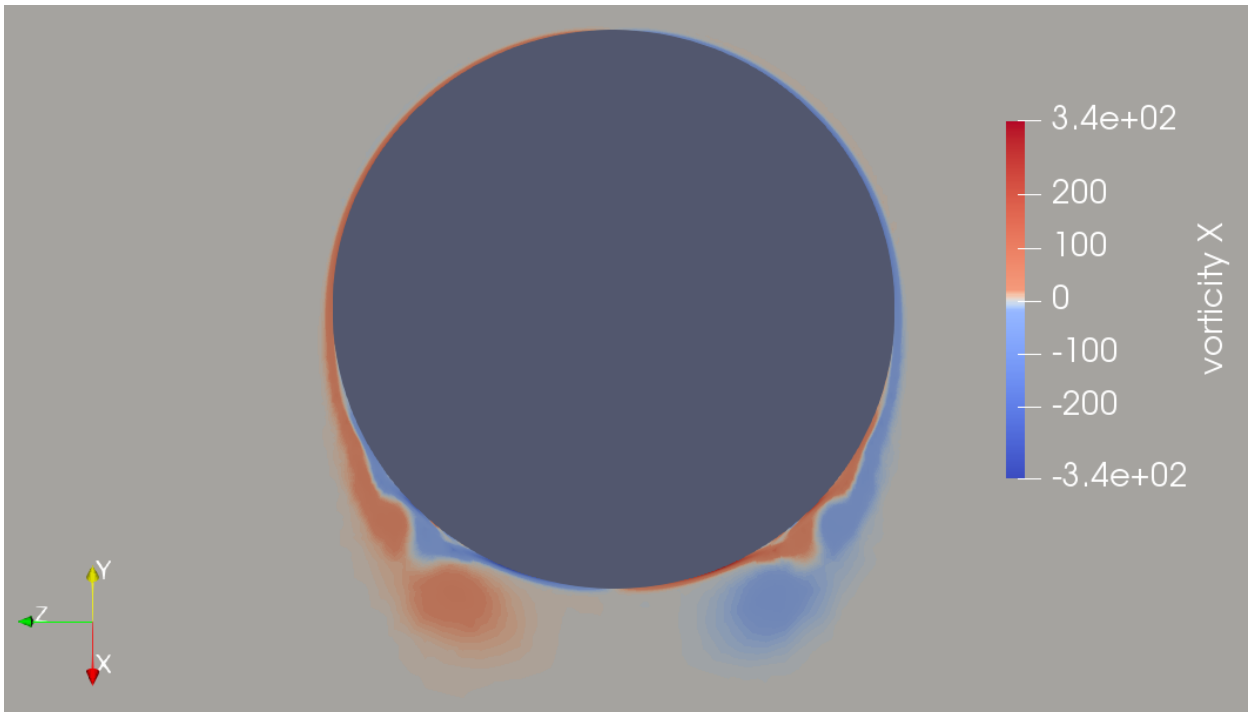

(a) $\bar{\eta} = -0.6$.

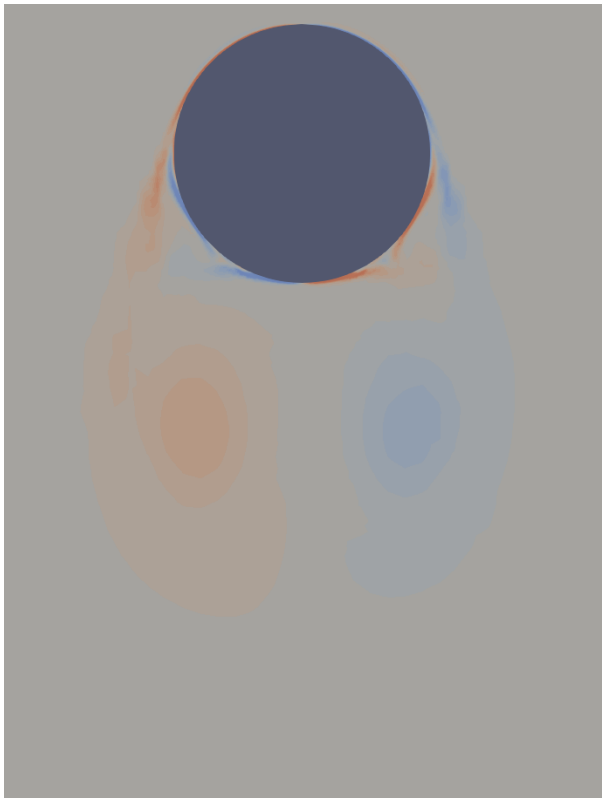

(b) $\bar{\eta} = 0.6$.

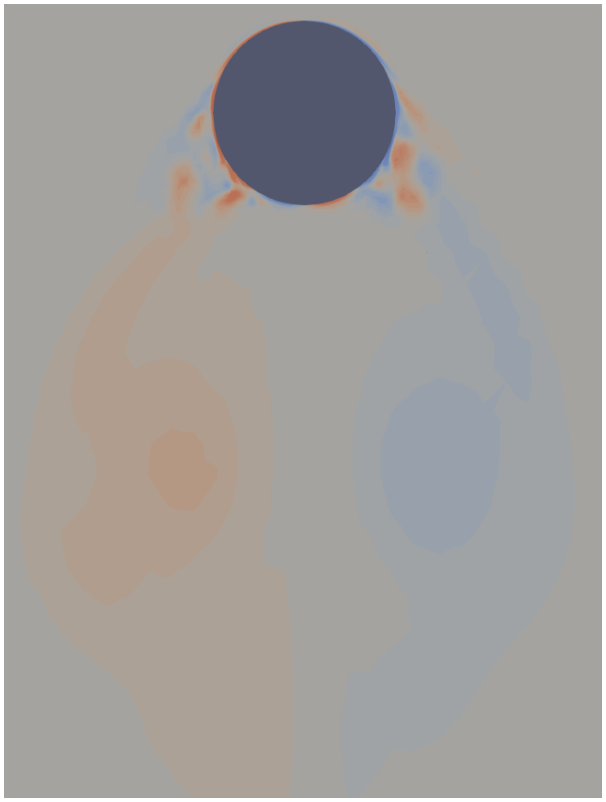

(c) $\bar{\eta} = 0.9$.

Figure 4.23: $k - \omega$ SST . $\omega_x D/U_0$ in the $\xi - z$ plane. Facing negative η-direction.

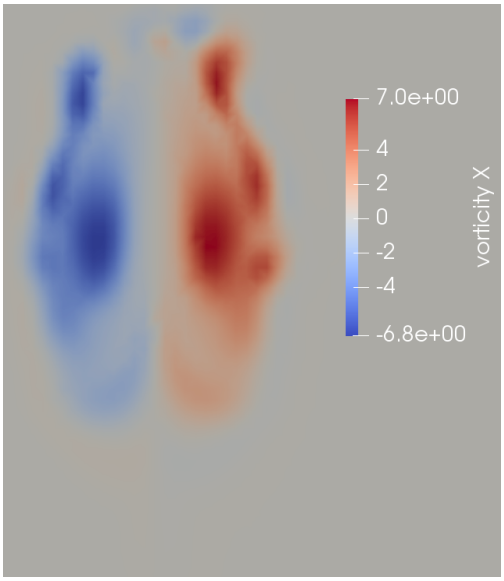

(a) $x = 2.5D$.

(b) $x = 4D$.

(c) $x = 6D$.

(d) $x = 8D$.

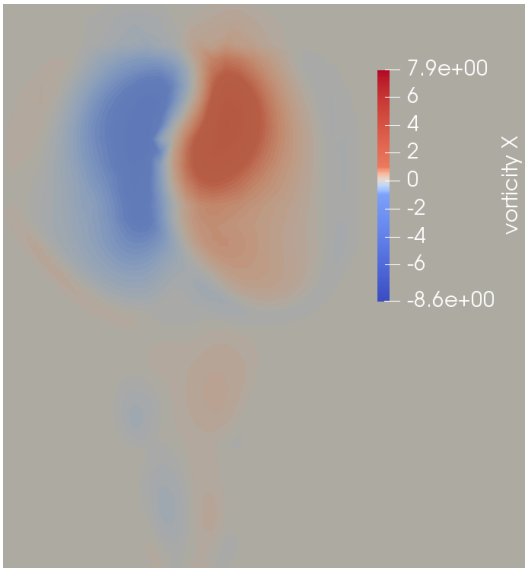

(e) $x = 10D$.

(f) $x = 12D$.

Figure 4.24: $k - \omega$ SST . $\omega_x D/U_0$ in the $y - z$ plane. Facing positive x-direction. Figures (a)-(d) share color map, and Figures (e)-(f) share color map.

(a) $k-\omega$ SST .

(b) $k-\omega$ $SSTLM$.

(c) $k-\omega$ $SSTLM$.

Figure 4.25: RANS models. Predictions of near-body turbulent kinetic energy and intermittency.

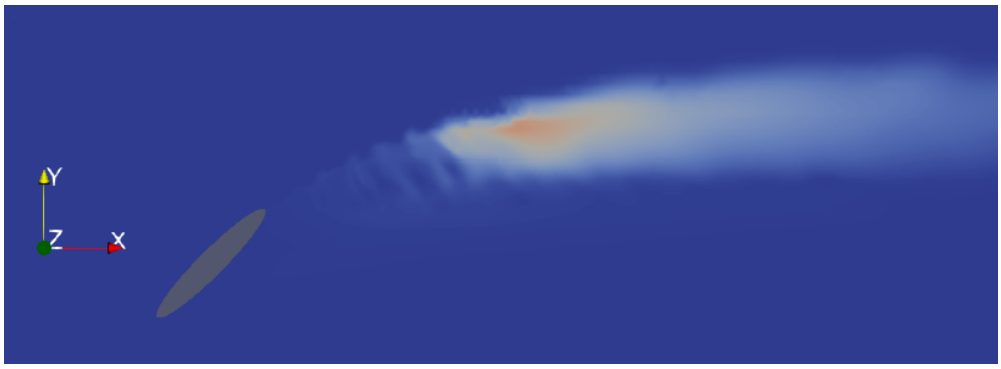

(a) $k-\omega$ SST .

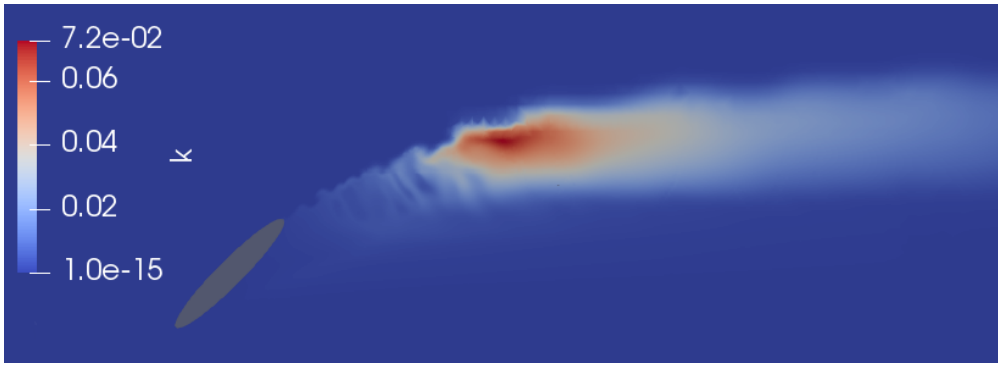

(b) $k-\omega$ $SSTLM$.

Figure 4.26: RANS models. Predictions of turbulent kinetic energy in the meridional plane.

4.4 Verification & Validation

In Appendix B, the results of the verification and validation study for the RANS and hybrid models are presented. I.e., average and RMS force coefficients for all grids, extrapolated values, numerical uncertainties and errors in the asymptotic range assumption. Figures 4.27-4.28 are qualitatively representative for the RANS and hybrid models, which indicates a flow field that is highly symmetric about $z = 0$. As clarified in section 4.1, a formal V&V study was not pursued for the LES models. Table 4.4 gives the multivariate metric r/r_{ref} for RANS and hybrid models (cf. section 2.5).

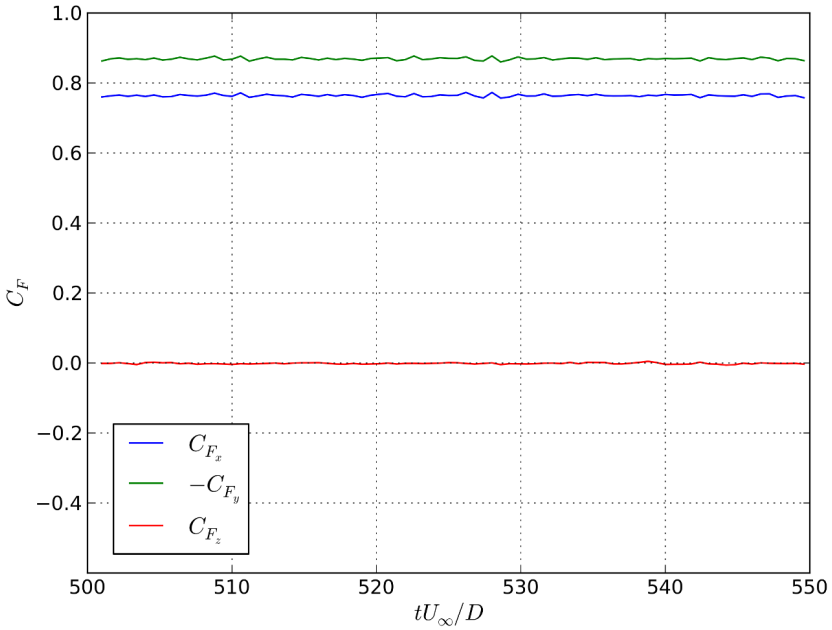

Figure 4.27: $k-\omega$ *SST* (M2).

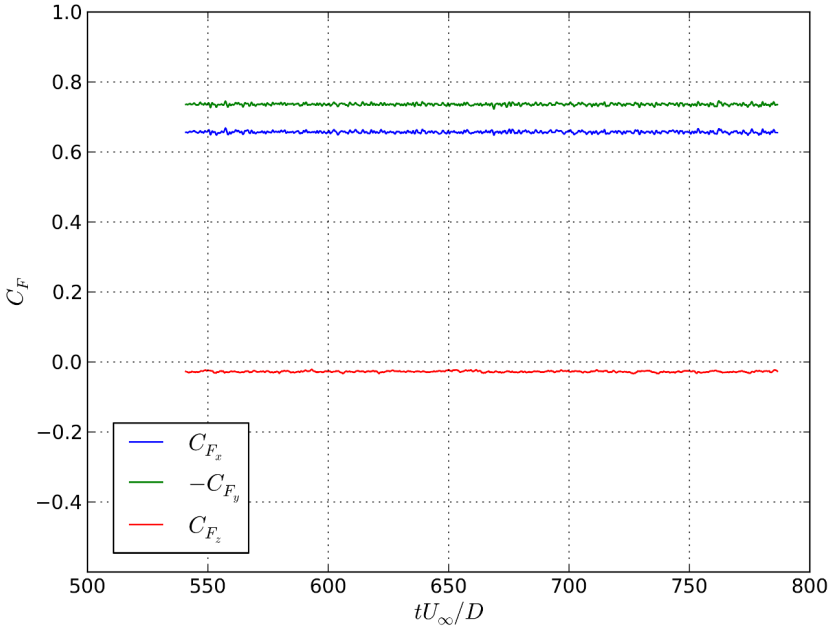

Figure 4.28: $k-\omega$ *SST SAS* (M3).

Table 4.4: Multivariate metric for RANS and hybrid models.

	$k-\omega\ SST$	$k-\omega\ SST\ LM$	$k-\omega\ SST\ SAS$	$k-\omega\ SST\ DES$
r/r_{ref}	11799	43.7	3.2	16.2

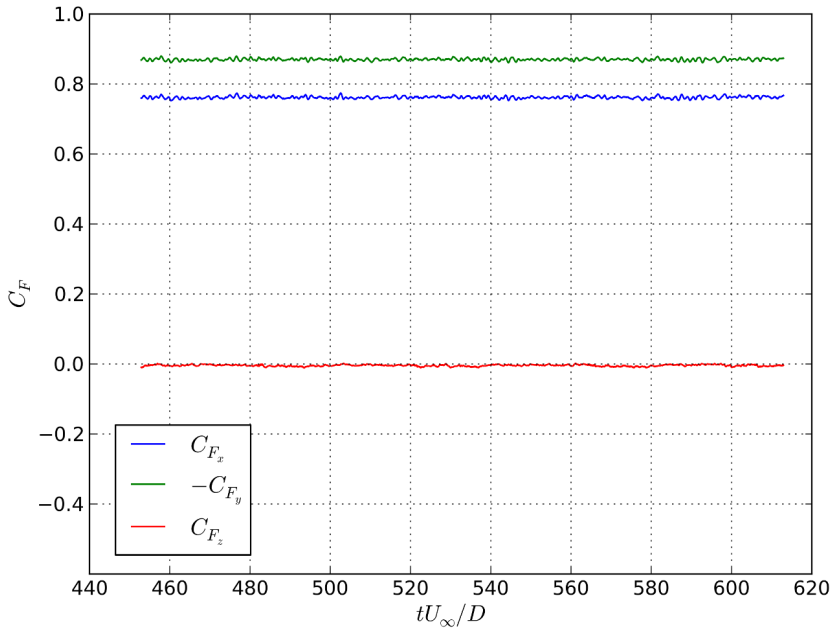

Figure 4.29: $k-\omega\ SST\ DES$ (M3).

Following the assumptions in section 3.5 and that RANS and hybrid simulations show qualitative similar results at different grid spacings, the validity of the V&V study is only dependent on one assumption: that the verification points may be described by an asymptotic expansion in the grid spacing, where higher order terms are neglected. I.e., the verification points are in the asymptotic range. The error in this assumption is reported in Appendix A (cf. Eq. 3.7). The maximum errors for $k-\omega\ SST$ and $k-\omega\ SSTLM$ are 8.0 % and 9.2 %, respectively. For the hybrid models, the calculations yielded irregular results. I.e., the results did not change with grid spacing or the change was not indicative of converging behavior (producing unreasonable convergence orders and accordingly useless GCI estimates).

Thus, the results indicate that the verification points are not in the asymptotic range for the coarsest mesh for the RANS models. However, there are limited guidelines on the uncertainty in the V&V results, given an error in the asymptotic range assumption. If an error of 9.2 % in the asymptotic range assumption invalidates the estimate of the numerical uncertainty, is unknown to the undersigned. The hybrid models' irregular behavior indicates that the models are not in the asymptotic range. A problematic feature of hybrid models in regards to V%V is that the modelling regions will change with different grids. Thus, applying the assumption of verification points being in the asymptotic range, is a questionable assumption.

A more accurate estimate for the numerical uncertainty could have been produced with the more work intensive procedure in Eça and Hoekstra (2009). This procedure is more general than the one applied in this study, possibly describing the behavior of both RANS and hybrid models. However, as the validation comparison errors are clearly dominating the numerical uncertainty, this was not pursued. I.e., as the RANS and hybrid models have $r/r_{ref} >> 1$, it is apparent that the models do not qualitatively reproduce the flow. An improvement in the estimate of u_{num} is assumed to not change this assessment. Note, the large deviations in r/r_{ref} for the different models are mainly caused by differences in estimates of u_{num}, following a more or less regular Richardson extrapolation. I.e., the numerical uncertainty is smaller for the RANS than the hybrid models, as the Richardson extrapolation is in better accordance with the asymptotic range assumption.

4.5 General Remarks

Physical Characteristics of the Flow

If all models are compared, considering their respective characteristics, some essential features of the flow may be identified.

The differences between RANS and Hybrid predictions in the wake suggest that unsteadiness is of major importance. The RANS filtering damps out small scale wake oscillations effectively, whereas hybrid models with added numerical diffusivity, predicts an unsteady wake. Considering in addition the hybrid results prior to stabilization, it is assumed that the wake instabilities are attributable to the wake oscillations (as conjectured in Jiang et al. (2015)). I.e., the hybrid model's SRS mode are able to capture the unsteadiness of the flow. The importance of capturing the unsteadiness to obtain the flow asymmetry is more clearly seen with the LES simulations. As the successful LES simulation progresses from initiation, the wake starts to oscillate with a steadily increasing amplitude. When the wake reaches a critical amplitude, it remains on one side and the asymmetry of the flow is established. Following the trend with higher amplitudes for lower numerical diffusivity, it is suspected that the oscillations are to increase further as the numerical diffusivity is removed entirely. With a stronger asymmetry, it is assumed that the wake modelled with Smagorinsky would preserve the asymmetry indefinitely.

As both hybrid and LES models are able to resolve unsteady wakes, this feature can not explain the difference in results of LES and hybrid models. This holds especially for $k-\omega\ SST\ DES$, which SRS mode is the Smagorinsky model (except the different model coefficient). It is assumed that the difference is caused by the differing near-body modelling of the two approaches. Turbulence anisotropy is assumed to be an important feature of the flow (cf. section 2.2)(unfortunately, data on the flow anisotropy where not available at the conclusion of this thesis). Since the flow is mainly attached, the hybrid models are in RANS mode near the body. The utilized RANS modes are all isotropic and thus provide the wake with mostly isotropic turbulence. This is believed to be inaccurate and thus distort the wake instabilities. This follows from the comparison between hybrid and LES results, where the hybrid results do not oscillate with large enough amplitudes to obtain the asymmetry. The Smagorinsky model are able to predict anisotropic Reynolds stresses, so this is believed to yield the higher oscillations and ultimately result in asymmetry. Note, the Smagorinsky results and the hybrid results prior to stabilization are comparable, as the hybrid model retains stability longer than what Smagorinsky needs to reach asymmetry.

Another feature of the flow, not captured by any of the included models, is the small scale KH-instabilities at the spheroid pressure surface. RANS attempts to model the effect of these structures, whereas LES is intended to resolve them. The Smagorinsky model is assumed to not be able to predict these structures as the model are unable to model wall-bounded laminar flows accurately, and because of insufficient near wall resolution (cf. section 2.2).

Appropriate Turbulence Modelling

Following the above, it is assumed that the appropriate modelling of this flow needs to capture near-wall anisotropy and wake unsteadiness. I.e., this is required to predict the flow's main characteristic, the wake asymmetry. It is identified two different type of models that are suspected to be able to predict this type of flow.

Hybrid models with an anisotropic RANS mode will satisfy these requirements. In this case, RSM is believed to be too costly, whereas EARSM-models are of greater interest. These types of models are not included in standard commercial solvers, but are in use and under development in academia (cf. Abe (2018), Gopalan and Jaiman (2015)). A problem with devising such a model is an accurate and robust anisotropic RANS model. That no EARSM-model is available in OpenFOAMv5.0 is indicative of accuracy and robustness issues. Additionally, the blending and transfer of turbulence from the RANS to the SRS region are difficult problems. Note, the triggering and evolution of KH-instabilites at the spheroid surface will be modelled with RANS.

LES are able to include the effects of anisotropy and unsteadiness. However, this study has proven that obtaining good LES results, from a practical point of view, may be troublesome. As

this flow case is highly sensitive to additional diffusivity, one cannot stabilize the solver easily without effecting the result significantly. That aside, it is believed that the Smagorinsky model is well suited to give an even better estimate of the topology and resulting force statistics. However, WALE and the Dynamic model are able to model wall-bounded laminar flows. These models are believed to improve the predictions of the primary vortex pair and the KH-instabilites on the spheroid pressure side. I.e., these features are assumed to be highly sensitive to this feature of the Smagorinsky model.

Conclusively, to model this highly three-dimensional, separating flow, anisotropic hybrid and LES models are believed to be the two appropriate model types. In terms of cost and model availability, LES might presently be preferable over anisotropic hybrid models; Numerous LES models are readily available in commercial solvers, whereas anistropic RANS models are not. Further, for flows where laminar-turbulent transition is of importance, RANS models should satisfy $y^+ < 1$ (Eça et al., 2016), making the RANS and LES computational costs comparable. However, for higher Reynolds numbers, hybrid models might be preferable. With increased Reynolds number, the flow anisotropy is generally smaller (Jovanovic and Nishi, 2017) and the wake instabilities are expected to be stronger; An anistropic, and possibly even an isotropic hybrid model, could be able to predict the flow asymmetry (given that the asymmetry persists for higher Reynolds numbers). At higher Reynolds numbers the log-layer law is relatively accurate and would reduce the size of a hybrid computation substantially relative to LES. In essence, models from these two types of models should be further assessed in a future V&V study to identify specific models at different Reynolds numbers.

Methodological Improvements for a Future V&V Study

The above assessment of appropriate turbulence modelling for this flow configuration was not strictly based on a formal V&V study as presented in the scope of this thesis. It was rather the result of considering qualitative features of the flow and the turbulence models. This was required as either all relevant scales of the respective models were not resolved and/or that the solution was unstable and had to be stabilized with artificial diffusivity. However, the qualitative considerations in this thesis can be utilized to choose appropriate models for a future, more rigorous V&V study that would aim to identify suitable anisotropic hybrid and LES models. Towards that end, methodological improvements to this study are discussed below.

Pre-processing

The hybrid and LES simulations have faced issues with unboundedness, and this has been deteriorating for the assessment of these models. Investigations of the unstable results showed that errors propagated from the transition regions between different refinement levels. Thus, grids with grading rather than refinement levels might be desirable. Another aspect is the boundary conditions, where alterations reduce the ill-conditioning of the linear system. Additionally, improving essential grid quality parameters such as skewness and orthogonality, may reduce the issue (Jackson, 2018).

Another improvement in the pre-processing of grids for LES is the development and use of utilities calculating x^+ and z^+. These quantities need to be monitored to ensure a proper near wall resolution, as this is required to resolve the near wall flow anisotropy correctly (cf. section 2.2).

In a V&V study, numerous grid refinements are needed and there is no available grid refinement utility in SnappyHexMesh. Hence, performing grid refinements are cumbersome, and more importantly, liable to change qualitative features of the mesh. I.e., with large and unpredictable changes following a refinement, the requirement of all scales being resolved may be hard to ensure. A possible replacement for SnappyHexMesh is the mesher in ReFresco, which has been utilized in numerous V&V papers (e.g., (Eça et al., 2017), (Vaz et al., 2017)).

V&V Procedures

As remarked in section 2.5, the procedure proposed in Eça and Hoekstra (2014) is more general and accurate than the approach utilized in this study. Following the use of meshing software more suitable for grid refinements, the requirement of performing simulations on 4 or more grids could

be satisfied. This would improve the estimate of the discretization error and not depend on the assumption of having grid spacing in the asymptotic range. Additionally, to have control of the influence of the iterative error, the procedure in Eça and Hoekstra (2009) could be pursued. The default tolerances applied in this study are mainly based on experience and do not necessarily yield negligible iterative errors.

Another important feature of this V&V study is the use of DNS for validation. Following the assumptions in section 2.5 and Oliver et al. (2014), the uncertainty of the DNS predictions is only attributable to discretization and sampling errors. In this study, the example case in Oliver et al. (2014) was utilized to produce a rough estimate of the uncertainty. This was required as the DNS study was yet to finish. In a future study, the procedure in Oliver et al. (2014) could be adopted to estimate the uncertainty. However, the procedures for use of DNS in validation are quite immature, as they are yet to be covered in ASME (2009). Nevertheless, as DNS data becomes available for more and more test cases, the development of uncertainty estimate procedures will become more pressing. Thus, in a future V&V study, these procedures may have been formalized and more easily adopted.

With more appropriate modelling, better pre-processing and uncertainty estimates, a more informative V&V study could be performed. I.e., besides force statistics, average velocities, wake frequencies and more could be investigated to improve the quality of the study. In doing so, the procedure of establishing the multivariate metric r/r_{ref} would have included more 'challenging' verification points. I.e., it is more challenging to predict local quantities as an average velocity compared to an integrated variable as a force coefficient. Thus, the difficulty or the 'level' of the V&V study must be taken into account when assessing model suitability with the r/r_{ref} criterion. In this study, the level of the V&V study is at the lowest level with only force coefficients, as the models have not been suitable and/or the simulations have not been of sufficient quality for higher level verification points.

Post-processing

All the post-processing in this study was performed with instantaneous flow fields. I.e., instead of time averaging quantities of interest, one snap shot was investigated. This leaves the question whether the snapshots were statistically representative. In this study, which has mainly been qualitative in nature, this feature is assumed to have marginal influence in the assessment of the results. For the most unsteady results with the Smagorinsky model, the results were investigated at other time instances and no major qualitative differences were observed. Thus, given the highly qualitative nature of this work, this is assumed to be of minuscule importance. However, in a more accurate V&V study this is of relevance, as sampling errors may be considerable. E.g., the vorticity field at the initiation of the primary vortex pair could be time-averaged to obtain representative results. As importantly, the DNS results should be statistically representative to ensure accurate validation.

Another feature of the post-processing that needs to be highlighted is the elliptic character of the system of equations (cf. section 2.1). I.e., an arbitrary cell is dependent on all the other cells in the flow domain. Thus, if the wake is asymmetric, this has an effect on the creation of the primary vortex pair. E.g., comparing the drag forces of the symmetric hybrid and DNS simulations is conceptually questionable. Nevertheless, important features of the different model predictions may be identified by assessing flow features independently.

In a more thorough V&V study, also the level and accuracy of the post-processing effort could increase. E.g., instead of analyzing ω_x at the near body, ω_η is a quantity of more relevance. Further, in assessing the suitability of isotropic hybrid models, the actual levels of anisotropy in the flow should be calculated with the DNS data. In addition to investigate the assumption of isotropy, this would shed light on the extra anistropic production in the $k-\omega$ SST SAS model. I.e., k distributions for the model and DNS could be compared. Concerning hybrid models in general, calculation of the turbulence length scales is of relevance for an accurate assessment of these models. Finally, numerous other flow quantities than those inspected in this study might be of interest when performing more accurate validation. This is naturally very related to the available validation data, but an example is the helicity density analyzed in Jiang et al. (2015).

Chapter 5

Conclusions and Recommendations for Further Work

In this study, a formal Verification and Validation (V&V) study was pursued for a set of RANS, hybrid and LES models. This was performed for the 6:1 spheroid at 45° incidence at $Re = 16000$ based on the minor axis. The validation material was preliminary results from a DNS study that predicts a separating and highly asymmetric wake. In the case of RANS models, the procedures in ASME (2009) and Hills (2005) were successfully adopted, and resulted in deeming the $k-\omega$ SST and $k-\omega$ SST models as unsuitable models for the studied flow configuration. These models predicted a steady, symmetric flow. The study was only partly successful for hybrid and LES models, as the simulations yielded unstable results with low-diffusion numerical schemes. Before instability, the hybrid models predicted an oscillating wake. However, the hybrid model was stabilized with a diffusive numerical scheme and this resulted in damping of all wake oscillations. These results were then used in the aforementioned V&V framework, which invalidated the two hybrid models $k-\omega$ SST SAS and $k-\omega$ SST DES. Further, the LES models were slightly stabilized, and the Smagorinsky model was able to predict an asymmetric wake for a prolonged period of time. The asymmetry was weaker than that observed in the DNS study, and this result was only obtained at one of the three grids. As WALE was unstable at one grid and predicted an oscillating wake on the two others, none of the LES models in this study were able to yield qualitative similar results on all grids, so no formal V&V study could be conducted.

The results gave strong indications of important physical features of the flow. A wake instability is assumed to trigger the development of the flow asymmetry; only scale-resolving models as LES or hybrid models are able to capture this property. Additionally, from a combination of theory and the comparison of hybrid and LES results, it is assumed that near-body turbulence anisotropy is of importance. Anisotropic near body modelling with the Smagorinsky model yields stronger wake oscillations than those seen for the hybrid models with isotropic RANS modes (prior to stabilization). Based on these findings, it is assumed that there are two types of turbulence models that can be able to predict the flow asymmetry. I.e., hybrid models with anisotropic RANS modes and LES models. Thus, RANS and hybrid models with isotropic RANS modes are assumed to be unsuitable. To identify specific models among the selected group of models, a new V&V study could be pursued. In that case, numerous LES models are easily available in commercial and, and based on this study, Smagorinsky and WALE are two promising models. Anisotropic hybrid models are, however, not well validated on simpler flow cases and are still under development.

As the hybrid and LES models were not formally validated in this study and numerous more models could be investigated with this test case, recommendations for methodological improvements to this study have been discussed. Regarding pre-processing, grids and boundary conditions preventing the instability due to unboundedness for the hybrid and LES models are needed. This is a necessity in order to establish the suitability of these type of models. In this endeavor, a mesher with good grid refinement capabilities is desirable. This is to reduce the amount of pre-processing work, but also to produce better quality grids. This is of big importance, as an accurate and general estimation of the numerical uncertainty requires simulations on at least 4 grids (Eça and Hoekstra, 2014). Additionally, this study has estimated the uncertainty of the DNS verification points. This

effort revealed that procedures on this topic is yet to be standardized and is not easily adopted in a V&V study. Lastly, with improved methodology and more suitable turbulence models, the 'level' of the verification points should be increased. I.e., in this study force coefficients have been used to ascertain qualitative features of the wake, whereas a more accurate assessment requires more difficult verification points. E.g. time averaged velocities at different points, measures on wake geometry and more.

In essence, further work related to V&V of turbulence models for this flow and separating bluff body flows in general may be summarized in the following points. The initial point is of comparable nature to this work, whereas the two latter are undertakings of a different character.

Conduct a follow-up V&V study , where stability issues with low-diffusion numerics for hybrid and LES models are resolved. This study could include isotropic and anistropic hybrid models and LES models. The difficulty of the verification points should be increased, such that the study becomes more informative. A large set of other possible improvements are given in section 4.5. If successful, this study could be seen in the larger context of numerous V&V studies and ultimately push development and understanding in turbulence modelling for separating bluff body flows.

Model development of anisotropic hybrid models are suspected to be needed to simulate flows similar to this flow configuration. This is of high practical importance, as LES simulations become quickly very expensive at higher Reynolds numbers relative to hybrid simulations.

Procedures for uncertainty estimates of DNS statistics could be further developed and standardized, which may lead to more published uncertainty estimates from DNS studies and increase the applicability of DNS for validation in V&V studies in general.

Bibliography

Abe, K.-i. (2018), 'Improvement of double-buffer problem in LES–RANS interface region by introducing an anisotropy-resolving subgrid-scale model', *Theoretical and Computational Fluid Dynamics* **32**(3), 263–283.

ASME (2009), *Standard for verification and validation in computational fluid dynamics and heat transfer*, first edn, American Society of Mechanical Engineers, New York, NY.

ASME (2014), *Test uncertainty*, first edn, American Society of Mechanical Engineers, New York, N.Y.

Deardorff, J. W. (1970), 'A numerical study of three-dimensional turbulent channel flow at large Reynolds numbers', *Journal of Fluid Mechanics* **41**(02), 453.

Drazin, P. G. (2002), *Introduction to hydrodynamic stability*, first edn, Cambridge University Press, New York, NY, USA.

Ducros, F., Franck, N. and Poinsot, T. (1998), Wall-adapting local eddy-viscosity models for simulations in complex geometries, *in* 'Numerical methods for fluid dynamics: 6th conference', Oxford, UK.

Eça, L. and Hoekstra, M. (2009), 'Evaluation of numerical error estimation based on grid refinement studies with the method of the manufactured solutions', *Computers and Fluids* **38**(8), 1580–1591.

Eça, L. and Hoekstra, M. (2014), 'A procedure for the estimation of the numerical uncertainty of CFD calculations based on grid refinement studies', *Journal of Computational Physics* **262**, 104–130.

Eça, L., Lopes, R., Vaz, G., Baltazar, J. and Rijpkema, D. (2016), Validation exercises of mathematical models for the prediction of transitional flows, *in* '31st Symposium on Naval Hydrodynamics', Monterey, CA, USA.

Eça, L., Saraiva, G., Vaz, G. and Abreu, H. (2015), The pros and cons of wall functions, *in* 'ASME International Conference on Offshore Mechanics and Arctic Engineering', St. John's, Newfoundland, Canada.

Eça, L., Vaz, G., Koop, A., Pereira, F. and Abreu, H. (2017), Validation exercises for the calculation of the flow around a squared column with rounded corners at high Reynolds numbers with the RANS equations, *in* 'ASME 2017 36th International Conference on Ocean, Offshore and Arctic Engineering', Trondheim, Norway.

Fu, T. C., Shekarriz, A., Katz, J. and Huang, T. T. (1994), 'The flow structure in the lee of an inclined 6:1 prolate spheroid', *Journal of Fluid Mechanics* **269**, 79–106.

Germano, M., Piomelli, U., Moin, P. and Cabot, W. H. (1991), 'A dynamic subgrid-scale eddy viscosity model', *Physics of Fluids A: Fluid Dynamics* **3**(7), 1760–1765.

Gopalan, H. and Jaiman, R. (2015), 'Numerical study of the flow interference between tandem cylinders employing non-linear hybrid URANS–LES methods', *Journal of Wind Engineering and Industrial Aerodynamics* **142**, 111–129.

Han, T. and Patel, V. C. (1979), 'Flow separation on a spheroid at incidence', *Journal of Fluid Mechanics* **92**(4), 643–657.

Hills, R. G. (2005), 'Model validation: Model parameter and measurement uncertainty', *Journal of Heat Transfer* **128**(4), 339–351.

Hoyas, S. and Jiménez, J. (2008), 'Reynolds number effects on the Reynolds-stress budgets in turbulent channels', *Physics of Fluids* **20**(10), 101511.

Jackson, A. (2018), 'A comprehensive tour of snappyhexmesh'. Accessed 28. January.
URL: *https://openfoamwiki.net/images/f/f0/Final-AndrewJacksonSlidesOFW7.pdf*

Jasak, H. (2018), 'Finite volume discretisation in OpenFOAM best practice guidelines'. Accessed February 5th.
URL: *www.tfd.chalmers.se/~hani/kurser/OS_CFD_2015/HrvojeJasak/DiscretisationBestPractice.pdf*

Jeong, J. and Hussain, F. (1995), 'On the identification of a vortex', *Journal of Fluid Mechanics* **285**, 69–94.

Jiang, F., Gallardo, J. P. and Andersson, H. I. (2014), 'The laminar wake behind a 6:1 prolate spheroid at 45 incidence angle', *Physics of Fluids* **26**(11), 113602.

Jiang, F., Gallardo, J. P., Andersson, H. I. and Zhang, Z. (2015), 'The transitional wake behind an inclined prolate spheroid', *Physics of Fluids* **27**(9), 093602.

Jones, W. P. and Launder, B. E. (1972), 'The prediction of laminarization with a two-equation model of turbulence', *International Journal of Heat and Mass Transfer* **15**(2), 301–314.

Jovanovic, J. and Nishi, M. (2017), 'The origin of turbulence in wall-bounded flows', *Thermal Science* **21**, 565–572.

Kolmogorov, A. N. (1941), 'The local structure of turbulence in incompressible viscous fluid for very large Reynolds numbers', *Proceedings of the USSR Academy of Sciences* **30**, 299–303.

Kreyszig, E., Kreyszig, H. and Norminton, E. J. (2015), *Advanced engineering mathematics : international student version*, tenth edn, Wiley, New Delhi, India.

Kundu, P. K., Cohen, I. M. and Dowling, D. R. (2012), *Fluid mechanics with Multimedia DVD*, fifth edn, Academic Press, Amsterdam; London.

Langtry, R. B. and Menter, F. R. (2009), 'Correlation-based transition modeling for unstructured parallelized computational fluid dynamics codes', *AIAA JOURNAL* **47**(12), 2894–2906.

Larssen, H. S. (2017), Numerical simulation of viscous flow and use of turbulence models - project thesis in TMR4520, Technical report, NTNU Trondheim.

Larsson, L., Stern, F. and Visonneau, M. (2014), *Numerical Ship Hydrodynamics An assessment of the Gothenburg 2010 Workshop*, first edn, Springer, Dordrecht, The Netherlands.

Lax, P. D. and Richtmyer, R. D. (1956), 'Survey of the stability of linear finite difference equations', *Communications on Pure and Applied Mathematics* **9**(2), 267–293.

Li, Z., Abrahamsen Prsic, M., Ong, M. C. and Khoo, B. C. (2018), 'Large eddy simulations of flow around two circular cylinders in tandem in the vicinity of a plane wall at small gap ratios', *Journal of Fluids and Structures* **76**, 251–271.

Liu, F. (2018), 'A thorough description of how wall functions are implemented in OpenFOAM'. Accessed 17. March.
URL: *http://www.tfd.chalmers.se/~hani/kurser/OS_CFD_2016/FangqingLiu/openfoamFinal.pdf*

Menter, F. (1993), Zonal two equation k-w turbulence models for aerodynamic flows, *in* '23rd Fluid Dynamics, Plasmadynamics, and Lasers Conference', Orlando, FL, U.S.A.

Menter, F. R. and Egorov, Y. (2010), 'The scale-adaptive simulation method for unsteady turbulent flow predictions. part 1: Theory and model description', *Flow Turbulence Combust Flow, Turbulence and Combustion : An International Journal published in association with ERCOFTAC* **85**(1), 113–138.

Menter, F. R., Kuntz, M. and Langtry, R. (2003), 'Ten years of industrial experience with the SST turbulence model', *Turbulence, heat and mass transfer* **4**(1), 625–632.

Müller, B. (2017), *Lecture notes for the course TEP4165 Computational Heat and Fluid Flow, NTNU Trondheim*, 1st Aug, 2017 edn.

Moussaed, C., Vittoria Salvetti, M., Wornom, S., Koobus, B. and Dervieux, A. (2014), 'Simulation of the flow past a circular cylinder in the supercritical regime by blending RANS and variational-multiscale LES models', *Journal of Fluids and Structures* **47**, 114–123.

NTNU-HPC-GROUP (2018*a*), 'About Vilje'. Accessed 23. March.
URL: *https://www.hpc.ntnu.no/display/hpc/About+Vilje*

NTNU-HPC-GROUP (2018*b*), 'OpenFOAM - Performance on Vilje'. Accessed 14. February.
URL: *https://www.hpc.ntnu.no/display/hpc/OpenFOAM+-+Performance+on+Vilje*

Oliver, T. A., Malaya, N., Ulerich, R. and Moser, R. D. (2014), 'Estimating uncertainties in statistics computed from direct numerical simulation', *Physics of Fluids* **26**(3), 035101.

OpenCFD (2018*a*), 'OpenFOAM extended code guide - k-omega shear stress transport (SST)'. Accessed 17. February.
URL: *https://www.openfoam.com/documentation/cpp-guide/html/guide-turbulence-ras-k-omega-sst.html*

OpenCFD (2018*b*), 'OpenFOAM extended code guide - k-omega-SST delayed eddy simulation (DES)'. Accessed 2. March.
URL: *https://www.openfoam.com/documentation/cpp-guide/html/guide-turbulence-des-k-omega-sst-des.html*

OpenCFD (2018*c*), 'OpenFOAM extended code guide - residuals'. Accessed 10. March.
URL: *https://www.openfoam.com/documentation/cpp-guide/html/guide-solvers-residuals.html*

OpenCFD (2018*d*), 'OpenFOAM guide/finite volume method'. Accessed 10. February.
URL: *http://openfoamwiki.net/index.php/Finite_volume_method_(OpenFOAM)*

OpenCFD (2018*e*), 'OpenFOAM v5 user guide: 4.4 numerical schemes'. Accessed 13. February.
URL: *https://cfd.direct/openfoam/user-guide/fvschemes/*

Patankar, S. V. and Spalding, D. B. (1972), 'A calculation procedure for heat, mass and momentum transfer in three-dimensional parabolic flows', *International Journal of Heat and Mass Transfer* **15**(10), 1787–1806.

Pereira, F. S., Eça, L. and Vaz, G. (2017), 'Verification and validation exercises for the flow around the KVLCC2 tanker at model and full-scale Reynolds numbers', *Ocean Engineering* **129**(Supplement C), 133–148.

Pope, S. B. (2000), *Turbulent flows*, first edn, Cambridge University Press, Cambridge.

Prandtl, L. (1904), 'Über flussigkeitbewegung bei sehr kleiner reibung [english translation in NACA technical memo. 452]', *Proc. Third Int. Math. Congr. Heidelbwerg* .

Roache, P. J. (1998), *Verification and validation in computational science and engineering*, first edn, Hermosa Publishers, Albuquerque, N.M.

Robertson, E., Choudhury, V., Bhushan, S. and Walters, D. K. (2015), 'Validation of OpenFOAM numerical methods and turbulence models for incompressible bluff body flows', *Computers and Fluids* **123**, 122–145.

Rosenhead, L. (1963), *Laminar boundary layers*, first edn, Clarendon Press, Oxford.

Rotta, J. C. (1972), *Turbulente Strömungen. Eine Einführung in die Theorie und ihre Anwendung : Leitfäden der angewandten Mathematik und Mechanik 15*, first edn, Teubner, Stuttgart.

Rumsey, C. (2018), 'The Langtry-Menter 4-equation transitional SST model (NASA)'. Accessed 14. February.
URL: *https://turbmodels.larc.nasa.gov/langtrymenter_4eqn.html*

Sagaut, P. (2006), *Large eddy simulation for incompressible flows : An introduction*, third edn, Springer-Verlag, Berlin; New York.

Schlichting, H., Gersten, K., Krause, E. and Oertel, H. (2017), *Boundary-layer theory*, ninth edn, Springer, Berlin.

Schlüter, J. U., Pitsch, H. and Moin, P. (2004), 'Large-eddy simulation inflow conditions for coupling with Reynolds-Averaged flow solvers', *AIAA Journal* **42**(3), 478–484.

Serre, E., Minguez, M., Pasquetti, R., Guilmineau, E., Deng, G. B., Kornhaas, M., Schäfer, M., Fröhlich, J., Hinterberger, C. and Rodi, W. (2013), 'On simulating the turbulent flow around the Ahmed body: A French-German collaborative evaluation of LES and DES', *Computers and Fluids* **78**, 10–23.

Shur, M. L., Spalart, P. R., Strelets, M. K. and Travin, A. K. (2008), 'A hybrid RANS-LES approach with delayed-DES and wall-modelled LES capabilities', *International Journal of Heat and Fluid Flow* **29**(6), 1638–1649.

Simpson, R. L. (1996), 'Aspects of turbulent boundary-layer separation', *Progress in Aerospace Sciences* **32**(5), 457–521.

Smagorinsky, J. (1963), 'General circulation experiments with the primitive equations', *Monthly Weather Review* **91**(3), 99–164.

Spalart, P., Jou, W. H., Strelets, M. and Allmaras, S. (1997), Comments on the feasibility of LES for wings, and on a hybrid RANS/LES approach, *in* 'Advances in DNS/LES: Direct numerical simulation and large eddy simulation; 1st conference', Ruston; LA.

Sumer, B. M. and Fredsøe, J. (1997), *Hydrodynamics around cylindrical structures*, first edn, World Scientific Publishing, London.

Tennekes, H. and Lumley, J. L. (1985), *A first course in turbulence*, first edn, MIT Press, Cambridge, Mass., USA.

Thomée, V. (2001), 'From finite differences to finite elements: A short history of numerical analysis of partial differential equations', *Journal of Computational and Applied Mathematics* **128**(1), 1–54.

Tikhomirov, V. M. (1991), Local structure of turbulence in an incompressible viscous fluid at very large Reynolds numbers, *in* V. M. Tikhomirov, ed., 'Selected Works of A. N. Kolmogorov: Volume I: Mathematics and Mechanics', Springer Netherlands, Dordrecht, pp. 312–318.

van Raemdonck, G. M. R., van Leeuwen, P. and van Tooren, M. J. L. (2016), Comparison of experimental and numerically obtained flow properties of a bluff body, *in* 'The Aerodynamics of Heavy Vehicles III', Vol. 79, Springer, Cham, Cham, Switzerland, pp. 393–411.

Vaz, G., Koop, A., Pereira, F., Abreu, H. and Eça, L. (2016), Validation: What, why and how, *in* 'ASME 2016 35th International Conference on Ocean, Offshore and Arctic Engineering', Busan, South Korea.

Vaz, G., Pereira, F. and Eça, L. (2017), On the prediction of shear-layer flows with RANS and SRS models, *in* 'VII International Conference on Computational Methods in Marine Engineering MARINE', Nantes, France.

Versteeg, H. K. and Malalasekera, W. (2007), *An introduction to computational fluid dynamics : the finite volume method*, second edn, Pearson Education, Harlow.

Watanabe, Y., Misaka, T., Obayashi, S., Arima, T. and Yamagichi, Y. (2009), Application of cross-flow transition criteria to local correlation-based transition model, *in* '52nd AIAA/SAE/ASEE Joint Propulsion Conference', Salt Lake City, UT, USA.

White, F. M. (2007), *Viscous fluid flow*, third edn, McGraw-Hill, Singapore.

Wilcox, D. C. (1998), *Turbulence modeling for CFD*, first edn, DCW Industries, La Cañada, Calif.

Wilcox, D. C. (2006), *Turbulence modeling for CFD*, third edn, DCW Industries, La Canada, Calif.

Wu, C. H., Ma, S., Kang, C. W., Lim, T. B. A., Jaiman, R. K., Weymouth, G. and Tutty, O. (2016), Vortex-induced motion of a square cylinder at moderate Reynolds numbers, *in* 'Proceedings of the International Conference on Offshore Mechanics and Arctic Engineering - OMAE', Busan, South Korea.

Appendix

A. Force Coefficient Time Histories

In this section the force coefficient time histories are presented. The characteristic behavior for RANS and hybrid models are given in Figures 5.1 and 5.2, respectively. All LES force coefficient time histories are given in Figures 5.3-5.5.

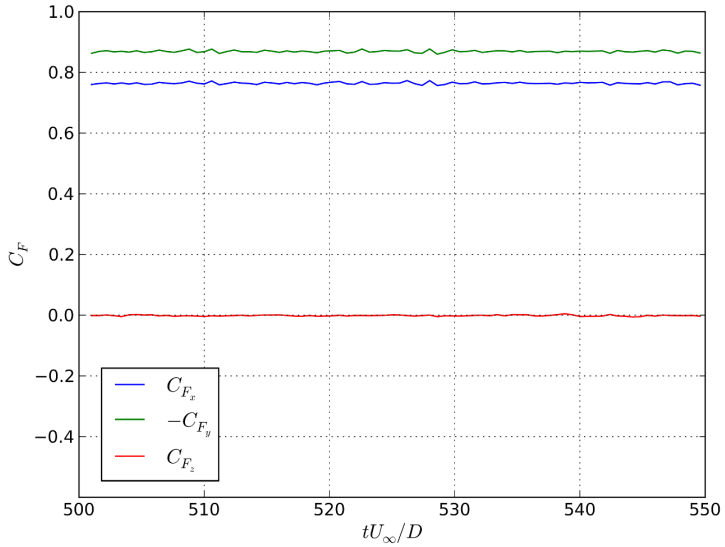

(a) $k-\omega$ SST (M2).

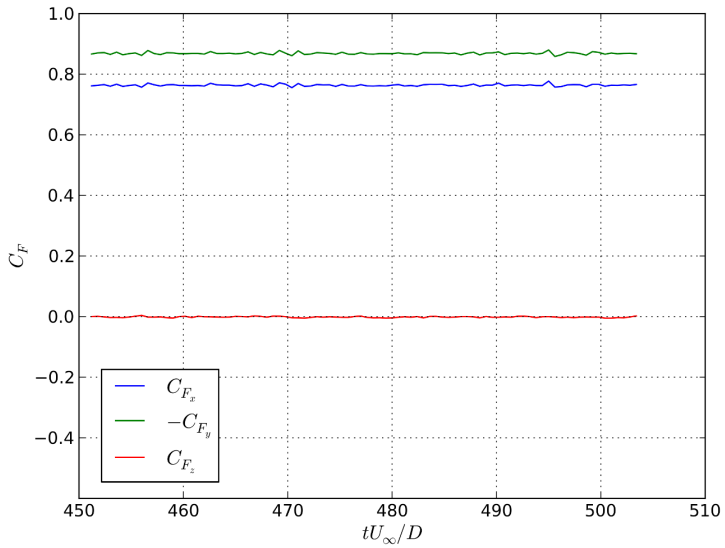

(b) $k-\omega$ $SSTLM$ (M2).

Figure 5.1: RANS characteristic force coefficient time series.

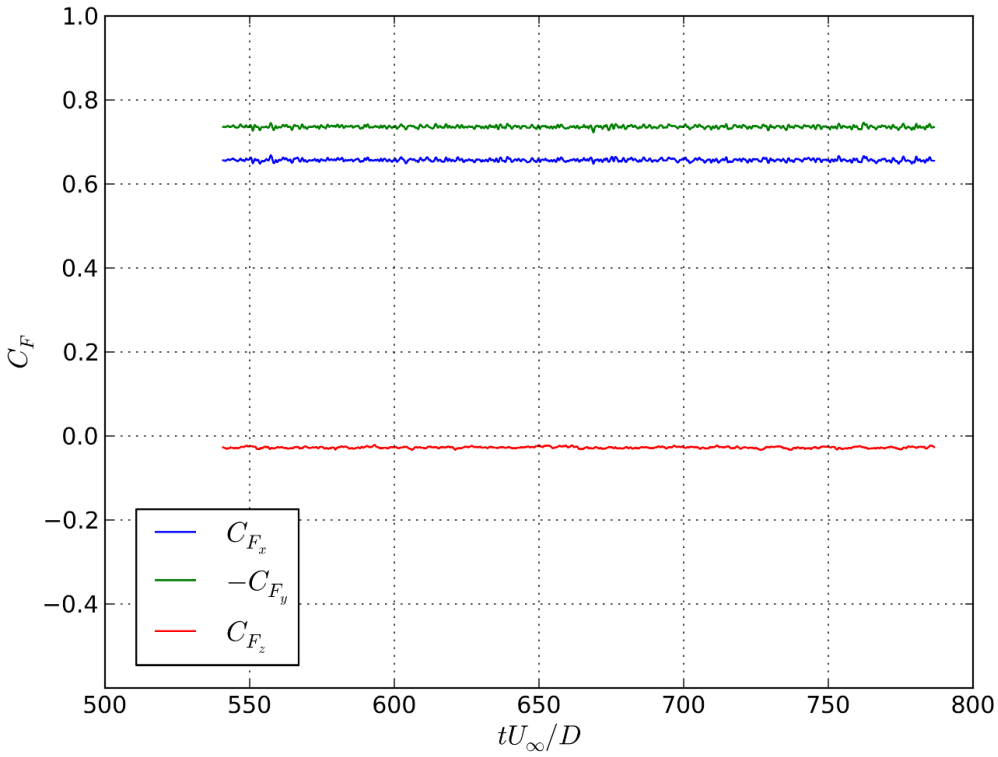

(a) $k-\omega$ *SST SAS* (M3).

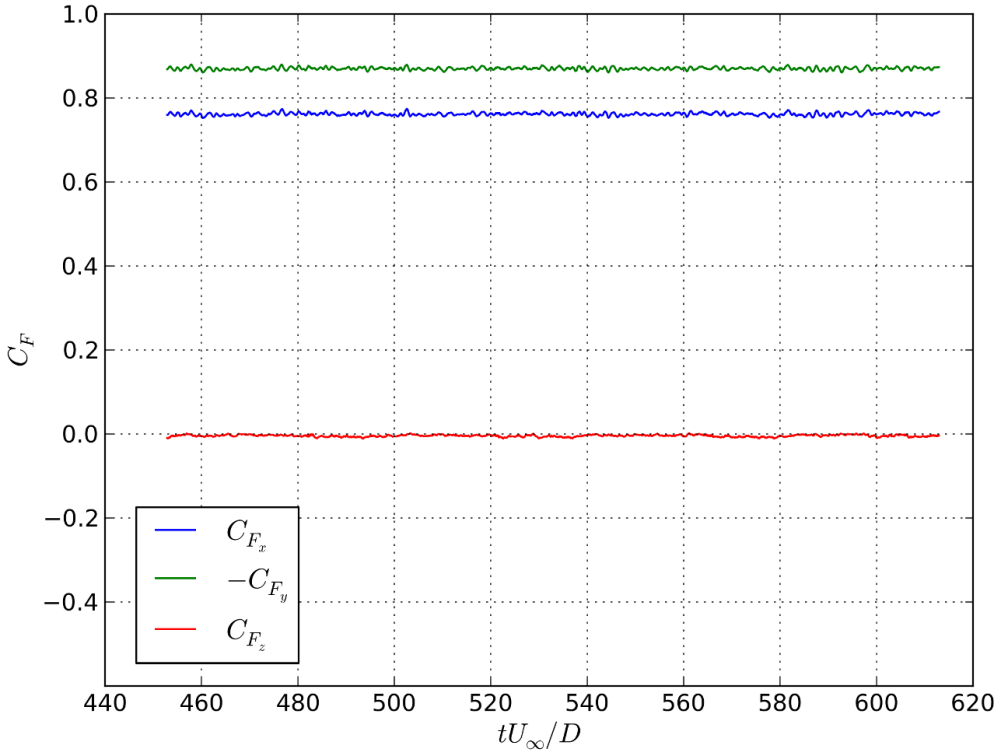

(b) $k-\omega$ *SST DES* (M3).

Figure 5.2: Hybrid characteristic force coefficient time series.

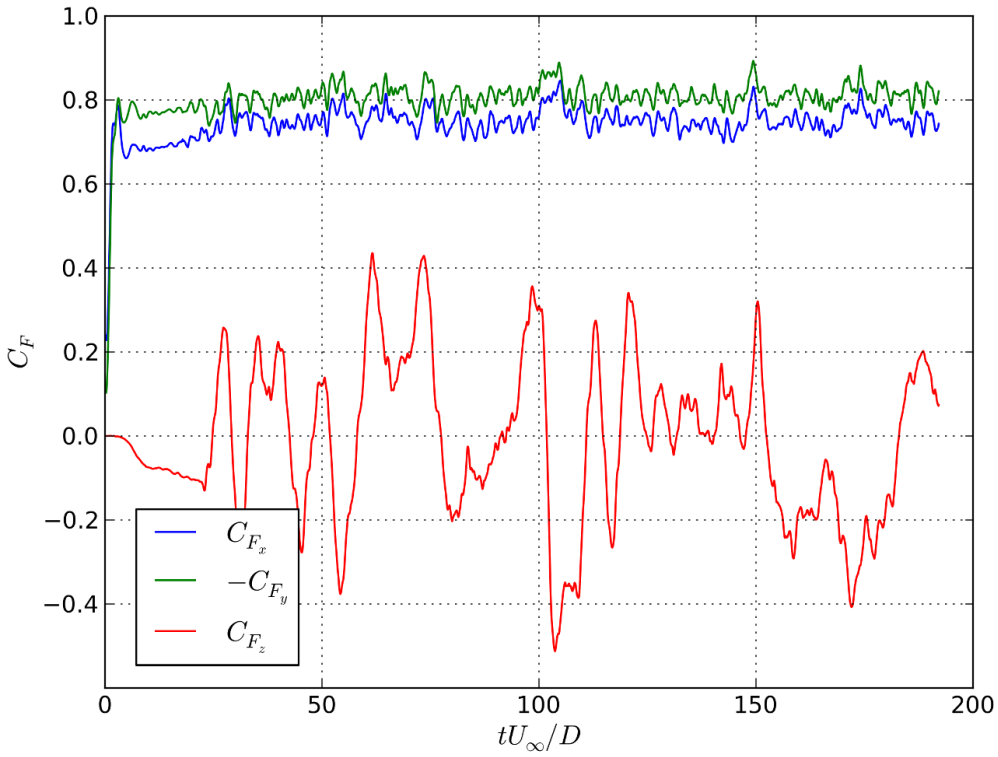

(a) Smagorinsky.

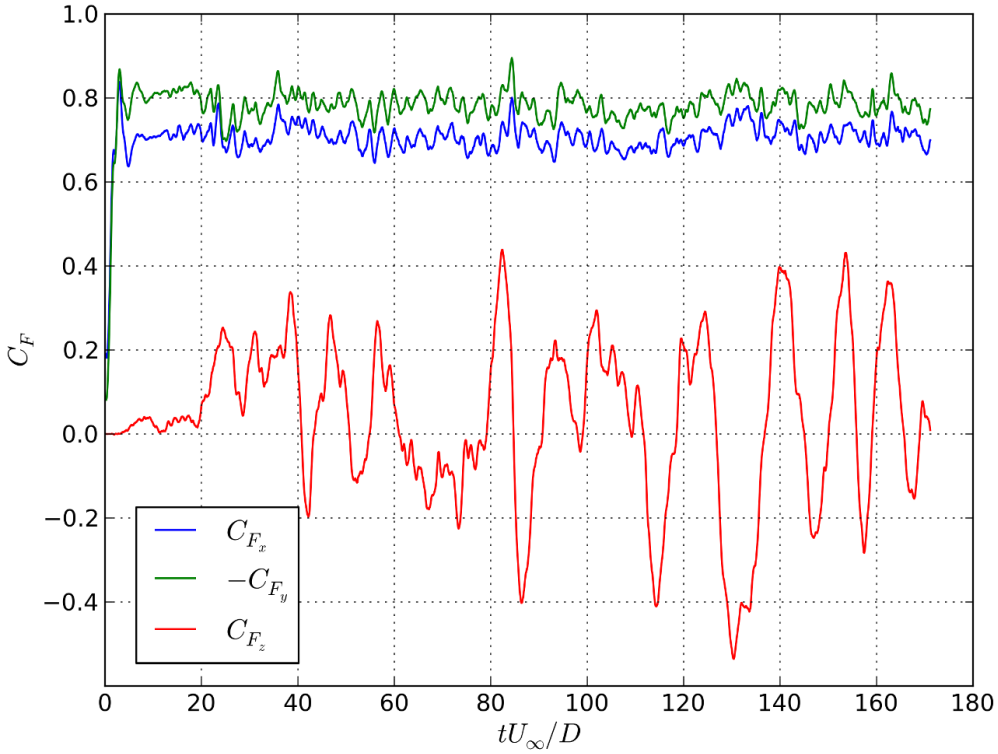

(b) WALE.

Figure 5.3: LES force coefficient time series (M2).

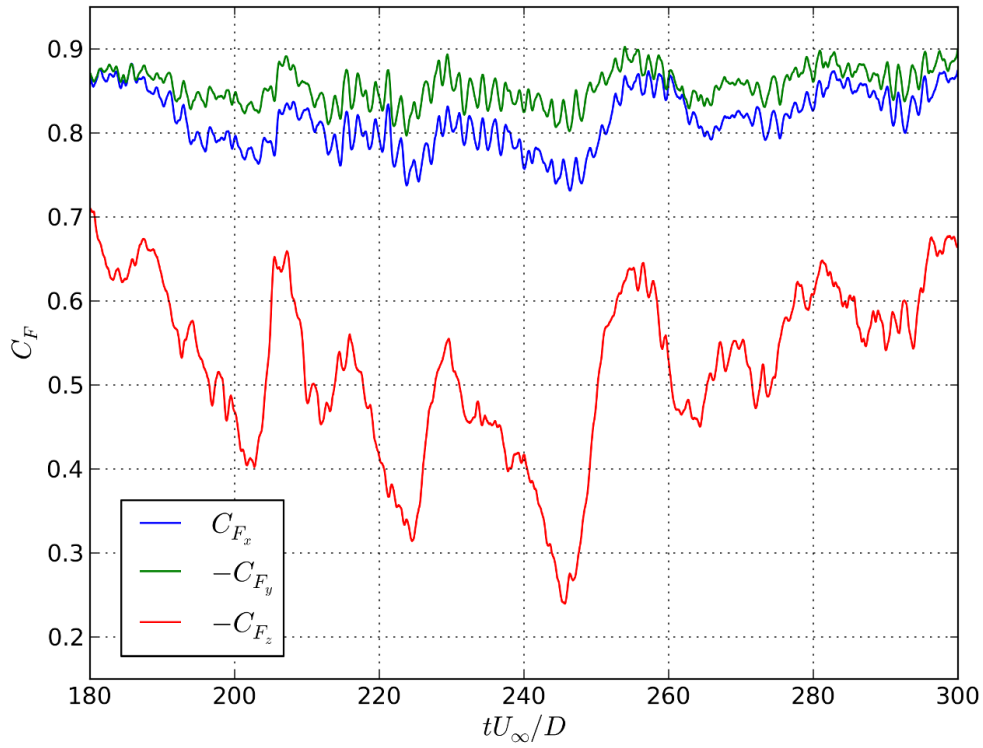

(a) Smagorinsky.

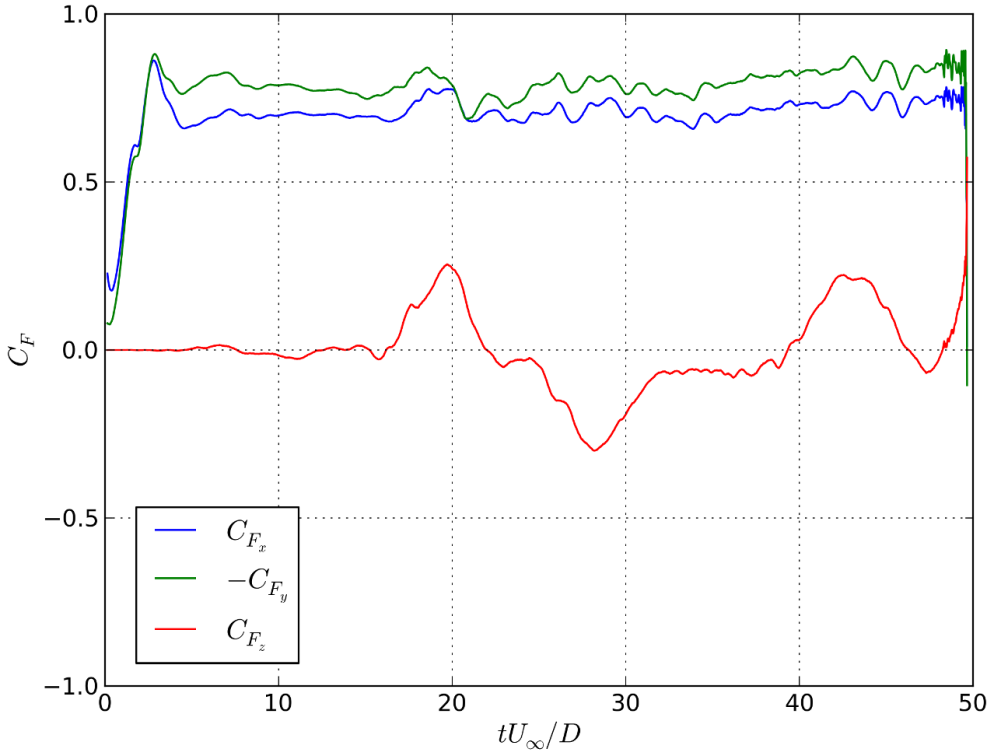

(b) WALE.

Figure 5.4: LES force coefficient time series (M3).

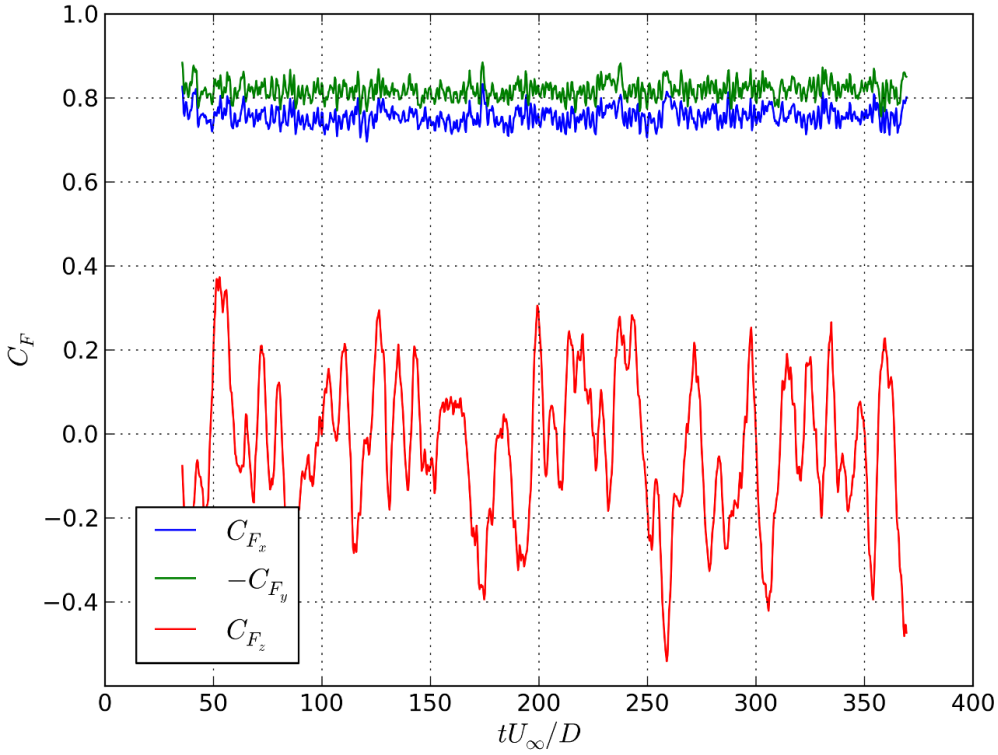

(a) Smagorinsky.

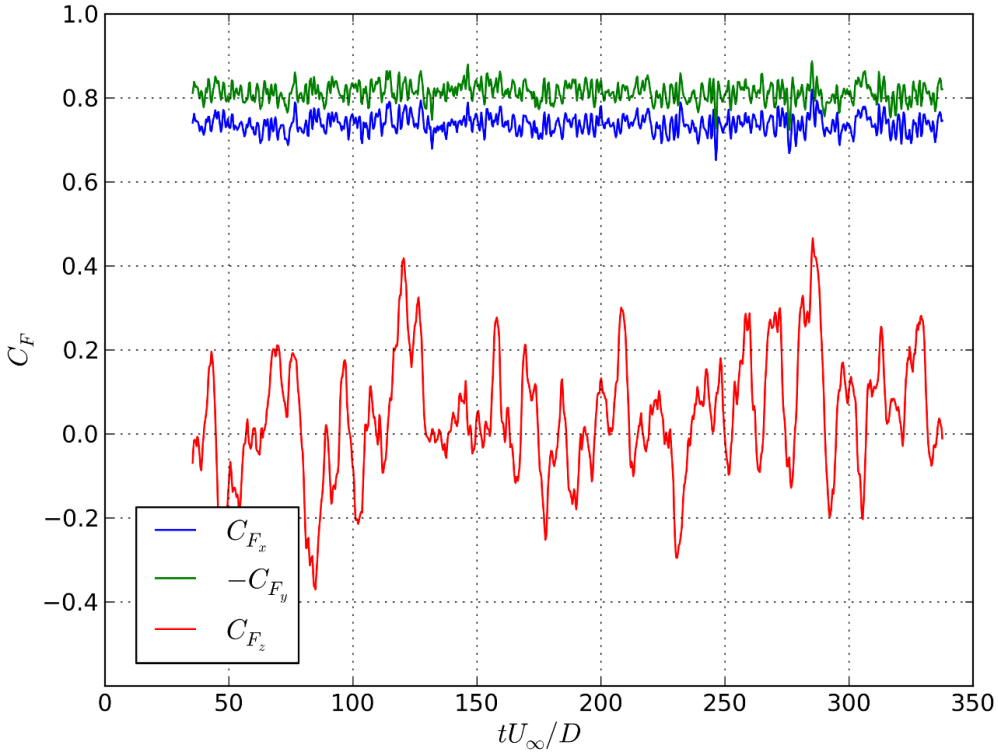

(b) WALE.

Figure 5.5: LES force coefficient time series (M4).

B. Results of the V&V study

Below, the results from the V&V study is given. Note, u_{num} and GCI_{error} are given in percentages. Blank entries represent irregular results and are not reported. These are caused by calcultions of p, where the simulated data is very close to zero or do not change with grid spacing. In this case, the result at the finest mesh is used to calculate the validation comparison error. Note, in the case of $k-\omega$ SST and $k-\omega$ $SSTLM$, fine, medium and coarse correspond to M3, M2 and M1. For hybrid and LES models, these terms correspond to M4, M3 and M2. The LES force coefficient statistics are also presented below. When calculating the validation comparison errors, the results from mesh M3 was used for Smagorinsky, and mesh M4 for WALE.

k − ω SST .

	CFxA	CFxR	CFyA	CFyR	CFzA	CFzR
Coarse	0.754	0.754	-0.861	0.861	0.001	0.002
Medium	0.764	0.764	-0.869	0.869	0.001	0.002
Fine	0.761	0.761	-0.871	0.871	0.005	0.006
Extrapolate	0.760	0.760	-0.872	0.872	0.005	0.006
E	-0.030	-0.040	-0.042	0.032	-0.655	-0.664
u_{num}%	0.185	0.185	0.075	0.075	-	-
GCI_{error}%	8.032	8.032	0.000	0.000	-	-

k − ω SST LM .

	CFxA	CFxR	CFyA	CFyR	CFzA	CFzR
Coarse	0.755	0.755	-0.861	0.861	0.002	0.003
Medium	0.764	0.764	-0.869	0.869	0.001	0.002
Fine	0.760	0.760	-0.870	0.870	0.006	0.006
Extrapolate	0.757	0.757	-0.870	0.870	-0.000	0.001
E	-0.033	-0.043	-0.040	0.030	-0.660	-0.669
u_{num}%	0.476	0.476	0.016	0.016	-	-
GCI_{error}%	9.213	9.213	0.000	0.000	6.996	7.683

k − ω SST SAS .

	CFxA	CFxR	CFyA	CFyR	CFzA	CFzR
Coarse	0.656	0.656	-0.730	0.730	0.013	0.013
Medium	0.657	0.657	-0.736	0.736	0.027	0.028
Fine	0.734	0.734	-0.829	0.829	0.007	0.008
Extrapolate	0.734	0.734	-0.829	0.829	0.074	0.0089
E	-0.066	-0.066	0.001	-0.011	-0.586	-0.581
u_{num}%	13.285	13.285	14.985	14.985	-	-
GCI_{error}%	-	-	-	-	-	-

k − ω SST DES .

	CFxA	CFxR	CFyA	CFyR	CFzA	CFzR
Coarse	0.765	0.765	-0.870	0.870	0.002	0.003
Medium	0.762	0.762	-0.870	0.870	0.004	0.005
Fine	0.767	0.767	-0.878	0.878	0.019	0.019
Extrapolate	0.754	0.754	-0.878	0.878	0.002	0.003
E	-0.036	-0.046	-0.048	0.038	-0.658	-0.667
u_{num}%	2.054	2.054	-	-	-	-
GCI_{error}%	2.749	2.749	-	-	-	-

Smagorinsky.

	CFxA	CFxR	CFyA	CFyR	CFzA	CFzR
Coarse	0.745	0.746	-0.804	0.806	0.011	0.189
Medium	0.816	0.816	-0.856	0.856	0.522	0.532
Fine	0.757	0.757	-0.819	0.820	0.035	0.178
E	0.026	0.016	-0.026	0.016	0.138	-0.138

WALE.

	CFxA	CFxR	CFyA	CFyR	CFzA	CFzR
Coarse	0.705	0.706	-0.782	0.784	0.038	0.196
Medium	0.718	0.719	-0.783	0.785	0.066	0.145
Fine	0.738	0.738	-0.814	0.814	0.039	0.149
E	-0.052	-0.062	0.016	-0.026	-0.621	-0.521

C. Extract of Literature Survey in Larssen (2017)

Turbulence Modelling of Bluff Bodies

In this main part of the review, I will present research efforts focusing on validation of turbulence modelling of bluff bodies at high Reynolds numbers. The papers are presented in increasing degree of model complexity/computational cost. Most of the studies include multiple models, so this chronology is only schematic. The included models range from two equation RANS models to LES, but the emphasis is on anisotropic RANS and hybrid RANS/LES models. I.e., I consider these models to reasonably compromise between accuracy and computational cost relative to engineering purposes. This consideration is confirmed by the review. The studies included in this review range from 2014-2017, where a majority were published in 2016-2017.

Eça et al. (2017) validated the RANS models $k-\omega$ SST and Spalart & Allmaras for flow around a squared column with rounded corners with $Re = 10^5, 10^6, 10^7$. The results were validated against experimental data, and the simulations were performed with ReFRESCO. It is noted that for even the simple assumption of two-dimensional flow, the level of grid refinement and iterative convergence criteria required to obtain acceptable numerical uncertainties are more demanding than usually observed in the literature; with half a million cells, numerical uncertainties of selected flow quantities (C_{D_s}, St etc.) are not below 5 %. Further, only the $k-\omega$ SST model at $Re = 10^5$ is able to predict zero lift statistically. A possible explanation of their behavior is that theses models were developed for statistically steady problems, making them unsuited for the complex separating flows around the squared column. As the applied models struggle to predict the simplified 2D flow, the authors suggest that the models are not sophisticated enough to reproduce the actual 3D flow.

In van Raemdonck et al. (2016), RANS simulations of a generic truck model is validated against experimental data. The two models in use were SST $k-\omega$ and realizable $k-\epsilon$ (a modified $k-\epsilon$ model), and the commercial software package FLUENT was used. The authors note good correspondence in the attached boundary layer flow seen in the front, at the sides and at the top of the truck. Boundary layer parameters as boundary layer thickness and momentum thickness are in good correspondence with experimental data. However, the wake structure deviate significantly from the experimental values. In Figure 5.6, the rear pressure distributions of the experimental and numerical results are presented. The authors suggest the discrepancy is because RANS forces steadiness on the flow, while it is highly unsteady in the wake. I.e., $T \not\ll T2$ (cf. section 2.1). Hence, two equation models do not seem to adequately model highly separating flows, but do predict attached boundary layers quite well. The authors suggest the models may be used in the preliminary design phase to get an estimate of mean force coefficients, but not to optimize rear truck design.

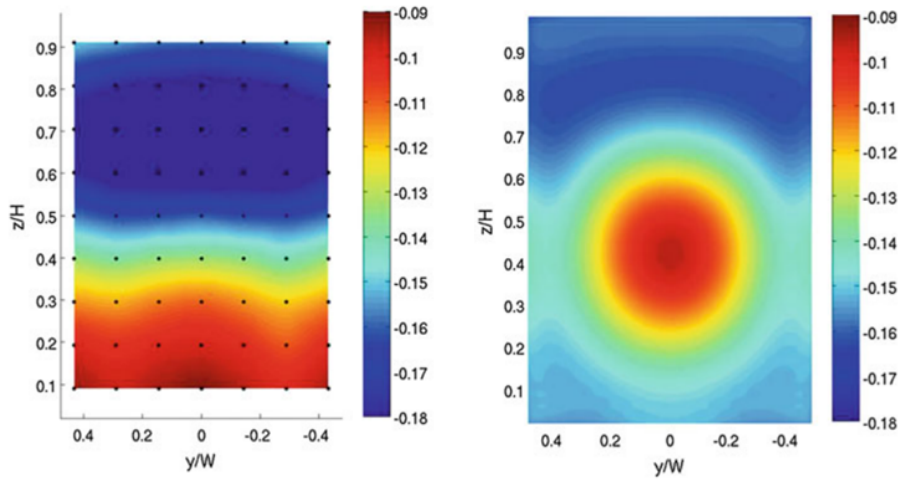

(a) PIV.

(b) RANS.

Figure 5.6: Truck rear pressure distributions in van Raemdonck et al. (2016)

A comprehensive validation study of different RANS models was performed in Pereira et al. (2017). 11 eddy viscosity based models and 3 EARSM models were validated by performing resistance and local flow field simulations of a KVLCC2 tanker (one of the test cases in the workshop on numerical ship hydrodynamics). The free-surface was neglected and none of the models used wall-functions, but rather a special low Re near wall treatment. The convergence properties of the different models were assessed with the ASME V&V 20 procedure. The results were qualitatively in line with the 2010 Gothenburg workshop on numerical hydrodynamics. The eddy-viscosity based models accurately predict the total resistance and show good convergence properties. EARSM produce worse predictions of the total resistance, but provides better estimates of the local flow at the ship stern (cf. Figures 11 and 12 in Pereira et al. (2017)).

Contrary to standard two-equation models, DES and SAS formulations are still under development. In Moussaed et al. (2014) a new DES formulation is tested on a circular cylinder at $Re = 1.4 * 10^5$. This formulation includes an automatic switch between RANS and LES by use of a blending function. This switch is meant to alleviate the earlier a priori specification of RANS and LES regions, making the DES pre-processing less laborious and error-prone. The predicted main flow parameters are generally in good correspondence to reference values, but the authors reckon that further development efforts on the RANS-LES switch are needed.

In Wu et al. (2016), the vortex-induced motion of a square cylinder is studied. The simulations were performed with OpenFOAM's pimpleDy solver, which allows mesh movement in one direction. The flow was simulated at $1500 \leqslant Re \leqslant 14000$ with the three models DDES(Delayed DES), DES-SST $k-\omega$ and SAS-SST $k-\omega$. The movement of the square cylinder was validated against experiments and showed decent agreement with the DES-SST $k-\omega$ and DDES models and very good agreement for SAS-SST $k-\omega$(cf. Table 3 in Wu et al. (2016)). Thus, only the SAS-SST $k-\omega$ was used in the subsequent simulations. As the cylinder length was varied, the simulations produced good quantitative results and the correct wake modes were observed.

Menter and Egorov (2010) conducted a validation study of the SAS and DES SST $k-\omega$, where the emphasis was particularly on the former model. The validation test cases was a circular cylinder and a NACA0021 airfoil at angle of attack 60° at $Re = 1.4 * 10^5$. Both of the test cases are characterized by massive flow separation. Force coefficients are well predicted by both models, but SAS was the more accurate(cf. Table 2 (Menter and Egorov, 2010)). For SAS, mean flow properties are accurately predicted, while second order turbulent statistics only show reasonable correspondance. Allover, both models perform well, but SAS do in general achieve better accuracy than the DES SST $k-\omega$ model for these validation cases.

A comprehensive study of DES and LES was conducted by Serre et al. (2013) on the Ahmed body for $Re = 768\ 000$. Three different LES models and the DES SST $k-\omega$ model were studied. The level of detail in these simulations are illustrated in Figure 5.7. All models were shown to produce results with good overall agreement with experiments, but significant deviations were observed for all models. E.g., a LES model with a near wall treatment did not predict the onset of separation correctly. Another high-order LES model, predicted incorrectly a confined recirculation zone at the front of the body, resulting in a dramatic overestimation of the drag coefficient (44%). The authors reckon LES simulations to be costly, but assess LES and DES to be the right level of turbulence modelling to accurately predict highly separating flows at high Reynolds number. They argue that further improvements of LES and DES algorithms are needed to improve accuracy and to reduce the computational cost. The results show that DES is a viable option to LES, but further algorithmic developments are needed.

In Vaz et al. (2017), a comprehensive validation study of different turbulence models are conducted for the flow cases: circular cylinder at $Re = 3\ 900$, $140\ 000$ and a rounded square prism at $Re = 100\ 000$ at incidence angles 0° and 45°. The models under investigation were: SST $k-\omega$, EARSM, DDES, XLES (similar to DDES) and PANS (hybrid between RANS and DNS). The simulations show that the isotropic SST $k-\omega$ is unable to calculate these flows accurately. In comparison to the SST $k-\omega$ model, the EARSM model results in considerable improvements, as can be seen in Table 2 (Vaz et al., 2017). The hybrid methods show a further leap in accuracy, and the results are in very good agreement with experiments for the circular cylinder. In Figure 5.8, the improvement in accuracy for more sophisticated models is illustrated. The improvement in

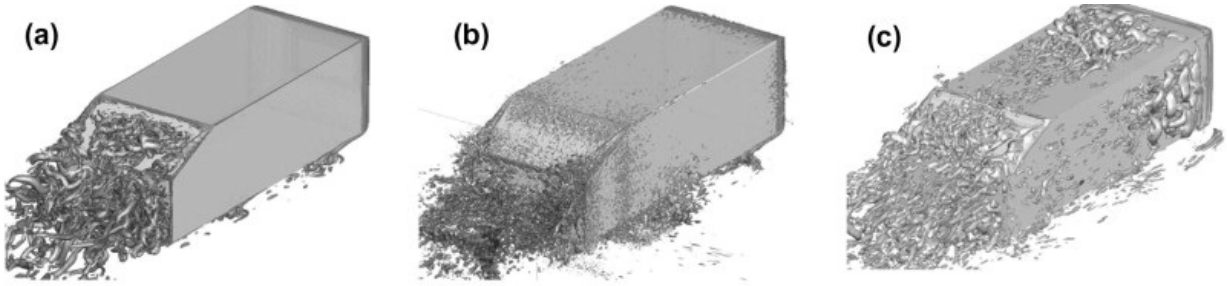

Figure 5.7: Q=60 - contours. (a) DES-SST, (b) LES-NWR, (c) LES-SVV (Serre et al., 2013).

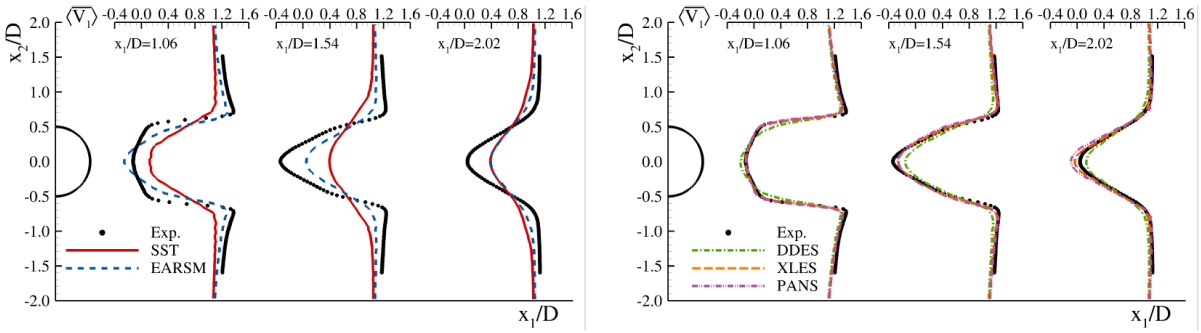

(a) $\langle \overline{V_1} \rangle$ - RANS models.

(b) $\langle \overline{V_1} \rangle$ - SRS models.

Figure 5.8: Time-averaged stream-wise velocity downstream as function of turbulence model. $Re = 3\ 900$. cf. Vaz et al. (2017).

accuracy brings a significant increase in computing time, and this is summarized in Table 6 (Vaz et al., 2017). For the square prism, there are also some discrepancies for the hybrid methods. The authors identify a need for further investigation of the square rounded prism, in order to identify model deficiencies. That effort is a part of a bigger set of verification studies, which is led by the development team behind the aforementioned ReFRESCO software package. This is a dedicated marine CFD tool, which is currently under development at mainly MARIN in the Netherlands.

Robertson et al. (2015) did a comparative study of turbulence models in OpenFOAM of the RANS and hybrid RANS/LES types. Three different test cases were used: flow over backward facing step, a sphere in the supercritical regime and a delta wing with a sharp leading edge. Among the RANS models, SST $k-\omega$ is found to be the most accurate. For hybrid methods, Spalart Allmaras - based DES model performed somewhat better than the $k-\omega$ based SAS model. As a sidenote, this study also identified which numerical schemes that are the most accurate and costly for the given type of turbulence model (RANS or hybrid). This is not relevant for this literature review, but highly relevant for performing efficient analyses in OpenFOAM of highly separated turbulent flows.

Discussion and Recommendations

In Larsson et al. (2014), it is noted that isotropic turbulence models seem to be inadequate to model 3D separating flows. This is verified in Eça et al. (2017) and van Raemdonck et al. (2016), where the isotropic models SST $k-\omega$ and realizable $k-\epsilon$ performs poorly. This is further confirmed in Pereira et al. (2017), where 11 isotropic models are tested. However, these studies also show that when determining the total drag off a body with a large length/breadth-ratio (e.g. ships and trucks), an isotropic model is quite accurate. Boundary layers with limited curvature is accurately predicted, as these models have been tested and developed extensively for these types of flows. In this case, the assumption of an isotropic eddy viscosity seems to be accurate. The studies indicate that the SST $k-\omega$ model is the most accurate among the isotropic models.

Larsson et al. (2014) and Pereira et al. (2017) show that the anisotropic RANS model EARSM is a good alternative to isotropic RANS models for curved, separating flows. A significant increase in accuracy is achieved by a relatively small increase in computing cost. I.e., algebraic expressions for the anisotropy tensor needs to be computed and the iterative convergence is somewhat slowed down. The model performs worse than the isotropic models for the aforementioned total resistance predictions. Hence, among RANS models, EARSM should be used for separating flows, while isotropic models are better suited to predict boundary layers with limited curvature.

In terms of accuracy, the next level of modelling is the DES and SAS models. With RANS behaviour in attached boundary layers and LES behaviour elsewhere, these models optimally achieve LES accuracy without having to resolve a boundary layer with LES-resolution. This implies a significant reduction in computing cost compared to LES. Wu et al. (2016), Serre et al. (2013) and Vaz et al. (2017) show that these models can achieve accurate results for 3D highly separating flows. However, these models show inconsistencies and needs to be further evaluated. E.g., the RANS-LES switch needs to be improved (Spalart et al., 1997). Thus, these models show promise but need further development and validation.

Comprehensive LES and DES simulations were performed in Serre et al. (2013). A further increase in accuracy is observed with LES, but at a considerable cost. If this is due to the RANS simulations in DES or because of algorithmic issues with DES, is an open question. Deficiencies with the LES simulations were found and further development needs to be performed for LES applied to 3D high Reynolds number separating flows.

The above may be summarized in the following:

- Isotropic RANS models are unable to predict high Reynolds number separating flows, but is a cheap and quite accurate option for boundary layers with limited curvature.
- The anisotropic RANS model EARSM yields a big improvement in the calculation of 3D separating flows compared to isotropic RANS models.
- DES and the SAS models provide accurate predictions for complex 3D separating flows, but are not well validated and show some inconsistencies. Further development and validation is needed.
- LES simulations provide accurate results, but are presently too computationally expensive for engineering purposes. LES has the inherent problem of a very fine boundary layer resolution, but its cost may be reduced by algorithmic/modelling improvements.

Thus, for engineering purposes, I recommend EARSM, DES and SAS models for turbulence modelling of flows around bluff bodies at high Reynolds number. The former do only increase the computational cost slightly from isotropic RANS models. The two latter are more costly, but have produced highly accurate results for complex flows. All of the three models need further development and validation, but the preliminary results looks promising.

D. OpenFOAM Scripts

D1. fvSchemes for LES Models

```
/*--------------------------------*- C++ -*----------------------------------*\
| =========                 |                                                 |
| \\      /  F ield         | OpenFOAM: The Open Source CFD Toolbox           |
|  \\    /   O peration     | Version:  4.1                                   |
|   \\  /    A nd           | Web:      www.OpenFOAM.org                      |
|    \\/     M anipulation  |                                                 |
\*---------------------------------------------------------------------------*/
FoamFile
{
    version     2.0;
    format      ascii;
    class       dictionary;
    location    "system";
    object      fvSchemes;
}
// * * * * * * * * * * * * * * * * * * * * * * * * * * * * * * * * * * * * * * * * * * * * * * * * * * * * * * * * //

ddtSchemes
{
    default         CrankNicolson 0.9;
}

gradSchemes
{
    default         Gauss linear;
    grad(p)         Gauss linear;
}

divSchemes
{

    default                         none;
    div(phi,U)                      Gauss filteredLinear2 0.025 0.0;
    div(phi,k)                      bounded Gauss limitedLinear 1;
    div(phi,omega)                  bounded Gauss limitedLinear 1;
    div(phi,gammaInt)               bounded Gauss limitedLinear 1;
    div(phi,ReThetat)               bounded Gauss limitedLinear 1;
    div((nuEff*dev2(T(grad(U)))))   Gauss linear;
    div(nonlinearStress)            Gauss linear;
}

laplacianSchemes
{
    default         Gauss linear corrected;
}

interpolationSchemes
{
    default         linear;
}

snGradSchemes
{
    default         corrected;
}


wallDist
{
    method meshWave;
}


// ************************************************************************* //
```

D2. fvSchemes for Hybrid & RANS Models

```
/*--------------------------------*- C++ -*----------------------------------*\
| =========                 |                                                 |
| \\      /  F ield         | OpenFOAM: The Open Source CFD Toolbox           |
|  \\    /   O peration     | Version:  4.1                                   |
|   \\  /    A nd           | Web:      www.OpenFOAM.org                      |
|    \\/     M anipulation  |                                                 |
\*---------------------------------------------------------------------------*/
FoamFile
{
    version     2.0;
    format      ascii;
    class       dictionary;
    location    "system";
    object      fvSchemes;
}
// * * * * * * * * * * * * * * * * * * * * * * * * * * * * * * * * * * * * * //

ddtSchemes
{
    default         CrankNicolson 0.9;
}

gradSchemes
{
    default         Gauss linear;
    grad(p)         Gauss linear;
}

divSchemes
{

    default                         none;
    div(phi,U)                      Gauss filteredLinear2 0.025 0.0;
    div(phi,k)                      bounded Gauss limitedLinear 1;
    div(phi,omega)                  bounded Gauss limitedLinear 1;
    div(phi,gammaInt)               bounded Gauss limitedLinear 1;
    div(phi,ReThetat)               bounded Gauss limitedLinear 1;
    div((nuEff*dev2(T(grad(U)))))   Gauss linear;
    div(nonlinearStress)            Gauss linear;
}

laplacianSchemes
{
    default         Gauss linear corrected;
}

interpolationSchemes
{
    default         linear;
}

snGradSchemes
{
    default         corrected;
}


wallDist
{
    method meshWave;
}


// ************************************************************************* //
```

D3. fvSolution for All Models

```
/*--------------------------------*- C++ -*----------------------------------*\
| =========                 |                                                 |
| \\      /  F ield         | OpenFOAM: The Open Source CFD Toolbox           |
|  \\    /   O peration     | Version:  4.1                                   |
|   \\  /    A nd           | Web:      www.OpenFOAM.org                      |
|    \\/     M anipulation  |                                                 |
\*---------------------------------------------------------------------------*/
FoamFile
{
    version     2.0;
    format      ascii;
    class       dictionary;
    location    "system";
    object      fvSchemes;
}
// * * * * * * * * * * * * * * * * * * * * * * * * * * * * * * * * * * * * * * * * * * //

ddtSchemes
{
    default         CrankNicolson 0.9;
}

gradSchemes
{
    default         Gauss linear;
    grad(p)         Gauss linear;
}

divSchemes
{

    default                         none;
    div(phi,U)                      Gauss filteredLinear2 0.025 0.0;
    div(phi,k)                      bounded Gauss limitedLinear 1;
    div(phi,omega)                  bounded Gauss limitedLinear 1;
    div(phi,gammaInt)               bounded Gauss limitedLinear 1;
    div(phi,ReThetat)               bounded Gauss limitedLinear 1;
    div((nuEff*dev2(T(grad(U)))))   Gauss linear;
    div(nonlinearStress)            Gauss linear;
}

laplacianSchemes
{
    default         Gauss linear corrected;
}

interpolationSchemes
{
    default         linear;
}

snGradSchemes
{
    default         corrected;
}


wallDist
{
    method meshWave;
}


// ************************************************************************* //
```

List of Figures

List of Tables